AXIAL SOLID-DENSITY DISTRIBUTION IN
GAS SOLID FLUIDIZED BEDS


by


CHAU JEN LEE

B. S., National Taiwan University, 1957


————————————


A MASTER'S THESIS


submitted in partial fulfillment of the

requirements for the degree

MASTER OF SCIENCE

Department of Chemical Engineering

KANSAS STATE UNIVERSITY
Manhattan, Kansas

1961

TABLE OF CONTENTS

# INTRODUCTION

The fluidization technique has been employed widely in many fields of the
process industry. The term _fluidization_ generally implies that solid particles
are suspended in a fluid flowing through a vessel. The mixture of particles
and fluid, therefore, forms the over-all bed.

The advantages and disadvantages of the fluidization technique in com-
parison with the conventional packed bed reactors can be found elsewhere.
(11, 28, 25). May (15) in his recent paper pointed out, "Chemical reactions
with fluidized beds have shown efficiencies varying all the way from 'better
than fixed beds' to as low as 5% of fixed beds. The low figure shows that the
bypassing must be important."

Wilhelm and Kwauk (26) first observed and described the distinction
between _particulate fluidized bed_ and _aggregative fluidized bed_. In the
particulate fluidization, particles are discretely separated from each other
and a mean free path for the particles seems to exist; whereas, the particles
in the aggregative fluidization are present in the bed not as individual units,
but as local aggregates. The particulate fluidized bed resembles closely an
ideal expansion of a fixed bed, whereas an aggregative fluidized bed is a
heterogeneous body composed of two separate coexisting phases --- dense
phase and bubble phase (dilute phase). A close analogy can be found between
the characteristics of a fixed bed and a particulate fluidized bed, but it is
not so between a fixed bed and an aggregative fluidized bed. The differences
are chiefly due to the fact that:

a) Particle distribution in the aggregative bed is extremely heterogeneous.

b) There is no definite way to measure the height of bed expansion.

## Literature Survey[*]

During the past years, the characteristics of aggregative fluidized beds have been studied by several different experimental methods. The experimental methods used by previous workers are summarized as follows:

1. High speed photographic studies were used by Matheson et.al.(14), Furukawa and Omae (7), and by Leopoldo Massimilla and J. W. Westwater (13). They took high speed photographs of bubbles through transparent walls of fluidized columns for gas-solid systems.

2. Shuster and Kisliak (24) studied the uniformity of aggregative fluidized beds by using diaphram plates to measure pressure gradients.

3. By measuring the variation of the electric capacitance between condenser probes, Morse and Ballou (18), and J. M. Dotson (5) examined the uniformity of aggregative fluidization. Later Bakker and Heertjes (1, 2) applied a similar technique to measure the point porosity of fluidized beds at various locations.

4. Yasui and C. N. Johanson (27) devised a small light probe to study the frequency, thickness and the rising speed of bubbles in aggregative fluidized beds.

5. The X-ray absorption technique made it possible for Grohse (9) to measure the over-all density of the aggregative fluidized bed without disturbing the bed. Baumgarten and Pigford (3) employed a $\gamma$-ray absorption technique in the study of bubble size and bubble frequency in aggregative fluidized beds.

---

[*] A rather complete literature survey concerning fluidization can be found in the Ph.D. thesis by P. T. Shannon (22).

Some of these investigators have proposed certain mathematical or empirical models to fit their experimental data. None of these models has as yet been verified as acceptable and applicable to aggregative fluidized beds in general.

## Purpose

The major purpose of the present work was to investigate the axial distribution of the fluidized bulk density in an aggregative fluidized bed by $\gamma$-ray technique. This is to determine qualitatively and quantitatively the axial density profile as the function of several operational variables.

## EXPERIMENTAL

### Application of $\gamma$-ray Absorption Technique to a Fluidized Bed

The radiation attenuation method of measuring density of a two-phase fluid has become prevalent during the past years (19, 3). This method of measuring density is based on the absorption of high energy radiation from a radioactive source which can be detected by a scintillation counter probe. Two of the characteristics of $\gamma$-rays are their high energy and their short wave length. When it is applied to the measurement of density, it is essentially a process of counting the number and indicating the kind of atoms by which the radiation is being absorbed. The attenuation of $\gamma$-rays is virtually independent of the chemical or physical state of the atoms.

If the absorption of the primary radiation by air (or by other fluidizing gas) is negligible, the attenuation of $\gamma$-rays shown on the scintillation probe is due to the absorption of $\gamma$-rays by the thickness of the walls of the fluidizing column, the constant absorbing media, such as the protective enclosure of the scintillation crystals (Fig. 1), and the particles packed or fluidizing in the path between the radioactive source and the scintillation counter probe. The $\gamma$-rays describe an essentially parallel path in passing from the source to the scintillation counter probe. The $\gamma$-rays absorption by a homogeneous material of density, $\rho$, and thickness, D, can be described by the Lamberts-Beer's Law:

$$I = I_0 \, e^{-\mu_m \rho D}$$

or

$$\ln(I/I_0) = -\mu_m \rho D \tag{1}$$

The absorption coefficient "$\mu_m$" varies in accordance with the following relationship:

$$\mu_m = (N_a/M) \, \sigma$$

where,

  $N_a$  is avagadro's number

  M   is the atomic weight, and

  $\sigma$  is the microscopic absorption cross section.

Therefore, the line average of solid density in the fluidized bed can be measured for each axial position by recording the radiation attenuation at each position and by converting it to density by equation (1), provided the following assumption is made:

The fluidizing particles and the fluidizing gas together form a substance of density, $\rho$, and with a thickness, $D_c$ (the inside diameter of the fluidizing column), where the absorption of $\gamma$-rays by the air (or fluidizing gas) is negligible.

## Apparatus and Equipment

A photograph of the equipment is shown in Fig. 1 while a schematic diagram is presented in Fig. 2. The equipment may be divided into two categories; (1), the column and its accessories, and (2), the gamma-ray source and nuclear instrumentation for detection, measurement, and recording of the transmitted gamma-ray beam.

The Column and Accessories. A 24-inch-high, 3.97-inch-diameter, lucite column was used. The column was covered at the top with a fine screen to permit the exhaust of the fluidizing air, but to retain any particles that might have been fluidized as high as the top of the column. The lower flange of the column was equipped with a pressure tap for measuring the pressure drop over the bed. Other taps were located every four inches up the flange of the column. The column was bolted directly to the distributor assembly.

Accessories to the column included the distributor assembly for distributing the air, manometers for measuring the pressure drops over the column and across the distributor, an air supply to provide dry air at a known velocity, and a jack for raising and lowering the column so that different heights in the bed could be investigated. These accessories will be discussed in this order.

Distributor Assembly. The air was distributed by the distributor assembly shown in Fig. 3. The air first passed through an 8-inch calming section of quarter-inch ceramic spheres. Above the bed of ceramic spheres, the air was distributed by a canvas filter cloth positioned between the lower flange of the column and a second lucite flange similar to the lower flange of the column.

Manometers. A 20-inch manometer using a manometer oil with specific gravity of 0.818 was used for measuring the pressure drop over the column.

Air Supply. A compressed-air line from the Kansas State University Physical Plant provided air for fluidizing. The air was dried by passing it through a silica-gel air dryer. The flow rate of air was measured by a rotameter.

Jack Assembly. The column-distributor assembly was mounted on an iron frame which was rasied and lowered by means of a hand jack making it possible to investigate various heights in the column.

Gamma-ray Source and Nuclear Instrumentation. Two gamma-ray sources were used to provide a greater intensity, thereby increasing the count rate and improving the statistics. These two sources were a five millicurie $Ra^{226}$ source and a twenty-five millicurie $Cs^{137}$ source. The two sources were placed in a 5/8-inch hole drilled lengthwise in a 2 x 4 x 8-inch lead brick. The 5/8-inch hole served as a collimator for the $\gamma$-radiation from the two sources. For added shielding, other lead bricks were placed around the brick containing the source. The beam was directed through the center of the column. On the opposite side of the column a 7/16-inch diameter collimator transmitted the beam to the scintillation probe which was positioned directly behind the collimator. This collimator consisted of two bricks. This was done
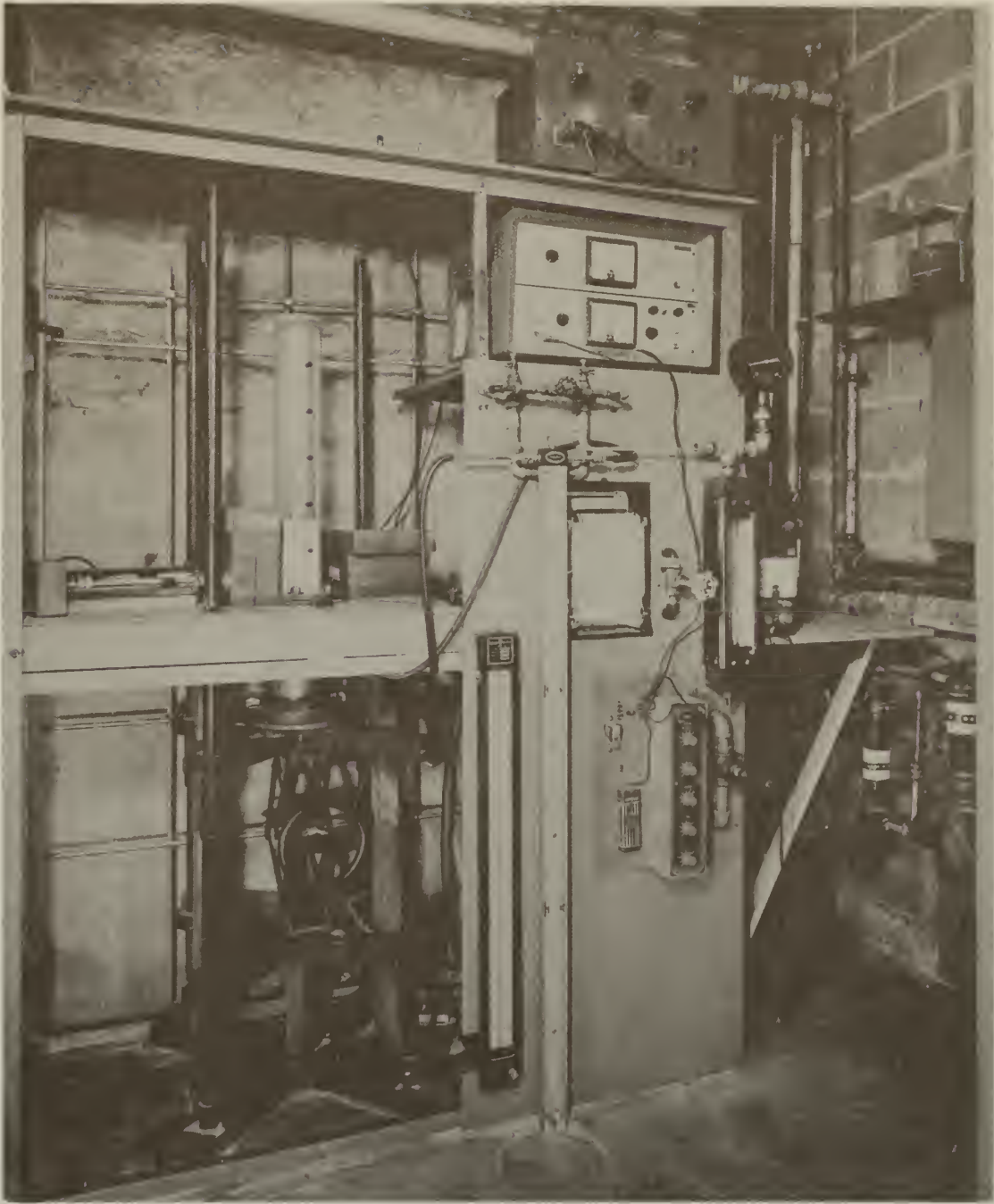
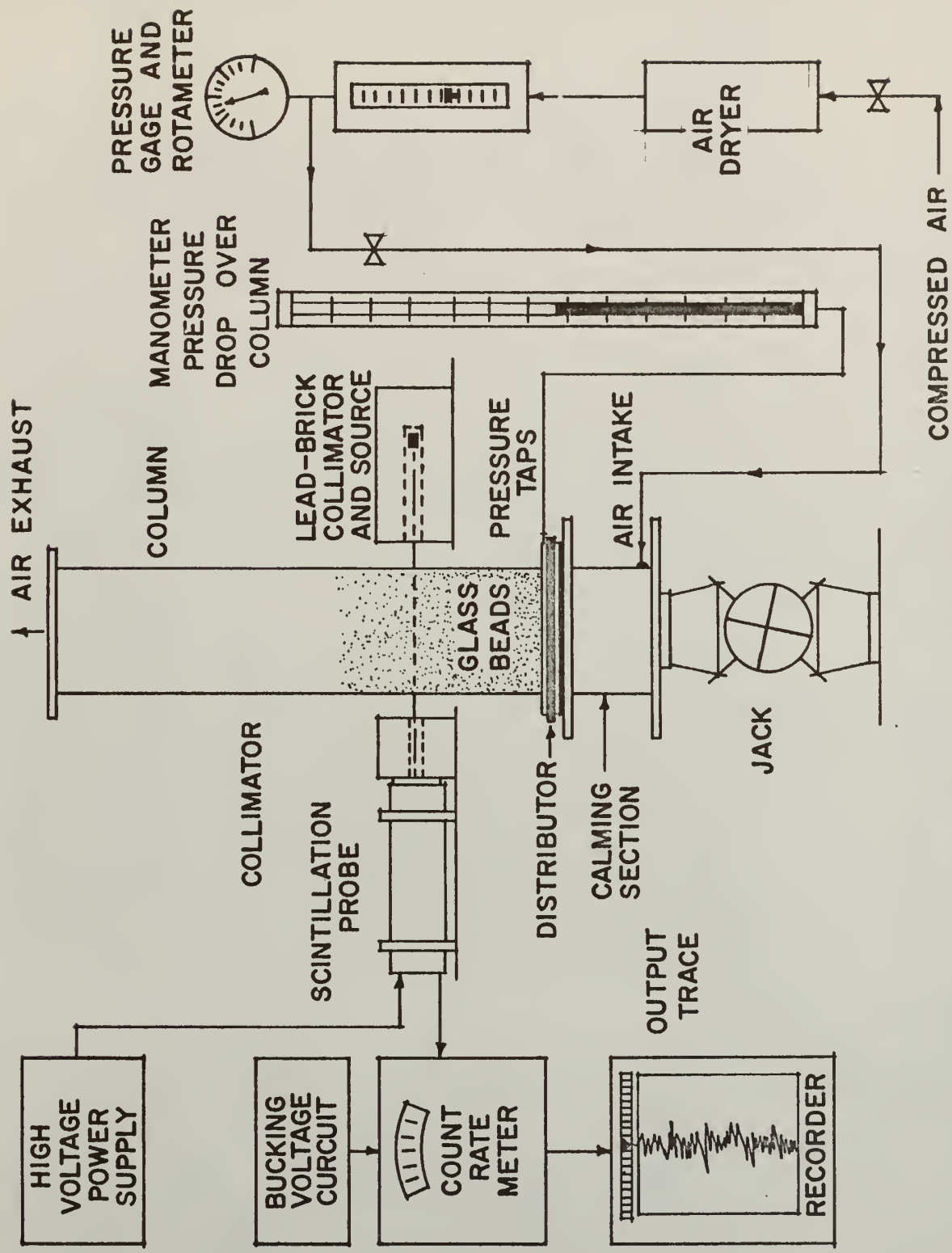Figure 1. Photograph of column and associated equipment.

Fig. 2. Schematic diagram of column, accessories, and instrumentation.

so that the 8-inch side of the bricks could be used to shield the probe from stray radiation. A close-up view of the source, collimators, column, and probe is shown in Fig. 4.

Instrumentation for the measurement, detection, and the recording of the transmitted gamma-radiation included a scintillation probe, power supply, modified count rate meter, bucking voltage supply, and recorder. These instruments will be discussed in this order.

Scintillation Probe. The probe, a Model Dp3, B-J Electronics, Borg-Warner Corporation, was used without modification. This instrument consisted of a Type 704, thallium-activated sodium iodide scintillation crystal, a Type 6292, DuMont photomultiplier tube, and a one-tube (6AK5) preamplifier. The probe was operated at 1200 volts.

Power Supply. A John Fluke Mfg. Co. Model 400BDA high-voltage power supply was used for operation of the scintillation probe.

Modified Count Rate Meter (CRM). The scintillation probe output was fed into a B-J Electronics Model DM1-D count rate meter that had been slightly modified. The meter included five time constants, 0.3, 1, 3, 10, and 30 seconds. Only the 30-second time constant was used for measurement of the average line density. The rate meter was equipped with five scale multiplication constants; 10, 30, 100, 300, and 1000. 300 scale was chosen since it gave the highest sensitivity. In choosing the 300 scale multiplier it became necessary to modify the rate meter. With the high activity used, it was necessary to apply a bucking voltage in order that the CRM would read on-scale, and so that the full range of density fluctuations could be covered. The bucking voltage was added to the input of the vacuum-tube voltmeter circuit of the CRM. This bucking voltage acted as a negative bias on the input grid of the voltmeter circuit.
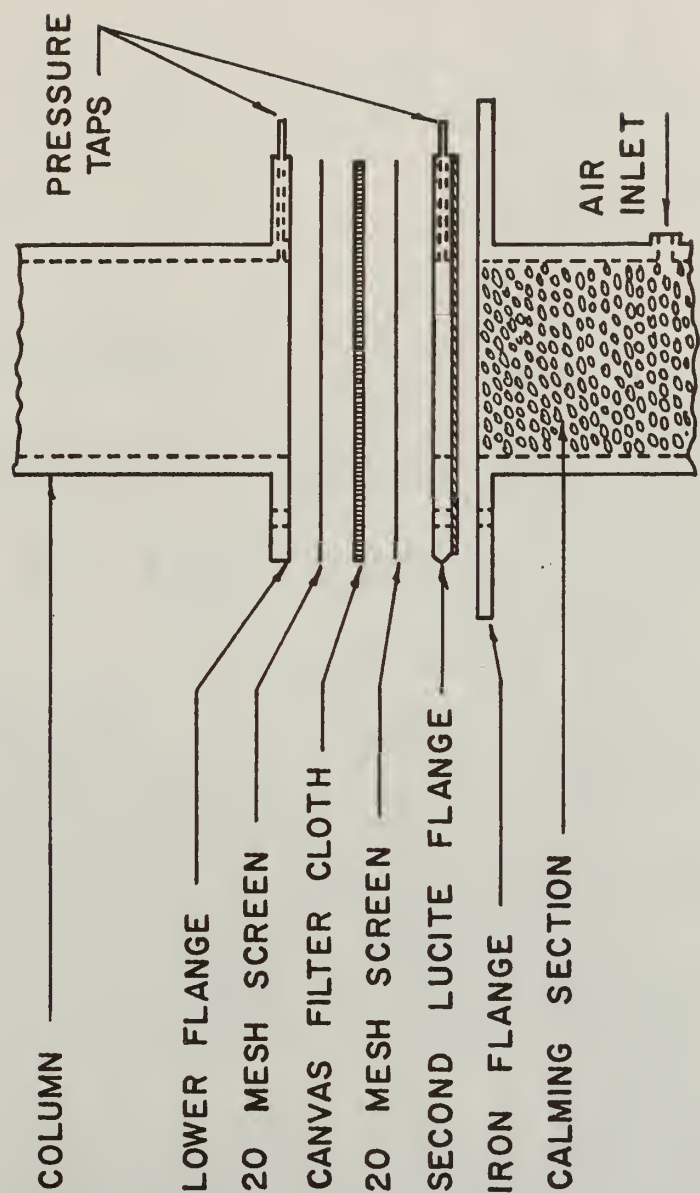
Fig. 3  Distributor  assembly.

Recorder. This instrument, an Esterline-Angus Model AW graphic ammeter was used without modification. The recorder was connected in series with the CRM.

## Preparation of Fluidizing Particles

The particles used in this experiment were glass beads manufactured by Minnesota Mining and Manufacturing Co. In order to minimize the error due to the size distribution effect when doing the investigation for narrow-cut particles, the purchased glass beads were reclassified by a sieving machine.

The glass beads actually used in the experiment were of two sizes:

(1) 40-45 U. S. mesh: particle diameter ranges from 0.0138 inches to 0.0164 inches, the average diameter of this size is 0.0153 inches.

(2) 80-100 U. S. mesh: particle diameter ranges from 0.0049 to 0.0070 inches, the average diameter of this size is 0.00642 inches.

The particles of 40-45 mesh were obtained by shaking about 100 grams of 3M catalog No. 70 glass beads on the sieving machine for three minutes, those particles passing through 40 mesh screen and retained on the 45 mesh screen were collected.

The 80-100 mesh particles were obtained from the catalog No. 110 glass beads by using the same technique as for 40-45 mesh particles. Those passing through 80 mesh and retained on 100 mesh particles were collected.

Some additional data were obtained with 60-70 mesh particles in order to confirm some of the observations and correlations resulting from the use of the other two particle sizes.

## Preliminary Calibrations

Count Rate Meter vs. Solid Density in the Fluidized Bed. For the prelimi-
nary calibration, spacers made from very thin aluminum sheets were used, which
had inside air-gap widths of 0.25, 0.50, 0.75, 1.00, 1.25, 1.50 & 2.00 inches,
respectively.

The calibration was done by inserting perpendicularly one spacer at a
time into the densely packed bed of glass beads of density equal to 1.502
grams/cu-cm, and then recording the radiation attenuation. This process was
also repeated by packing the glass beads inside the spacers, and leaving the
area surrounding the spacers empty. Then the density corresponding to a
particular spacer could be calculated with the following two relations:

(a) (Density of packed bed) x $(D_c - D_s)/D_c$, when the glass beads
were outside the spacers.

(b) (Density of packed bed) x $(D_s/D_c)$, when the glass beads were
inside the spacers.

These two linear relationships can be proved by the combined Lambert's equation:

$$\ln(I/I_o) = (\mathcal{U}_m)_c \int_c d_c + (\mathcal{U}_m)_{Al} \int_{Al} d_{Al} + (\mathcal{U}_m)_p \int_{pa} D'_p \qquad (2)$$

Where the subscript "c" denotes the radiation attenuation due to $\gamma$-rays
absorption by the walls of column; subscript "Al", by the aluminum sheets and
subscript "p", by the packed particles inside spacers or in the annular space
between column walls and the spacer sheets. Care was taken that the attenua-
tion due to column wall, aluminum sheets and all other possible absorbing
media stayed constant through the calibration (Fig. 4 and 5). Therefore,
Equation (2) can be simplified as:

$$\ln (I/I_o) = \text{constant} + (\mu_m)_p \rho_{pa} D_p'$$ (3)

where $(\mu_m)_p \rho_{pa}$ is also constant throughout the calibration, since the same glass beads were used, and the density of solid glass remained constant. Then the change in $\ln(I/I_o)$ is a linear function of $D_p'$ .

In dealing with the density of a fluidizing state, the radiation attenuation reading corresponding to one of the spacer calibrated values should have a density corresponding to the mass of $\rho_{pa} D_p' A_r$ particles distributed homogeneously in the volume, $D_c A_r$, where,

$A_r$ = projected area of $\gamma$-beam path.

Therefore, the density of the fluidized bed at a certain attenuation reading is:

$$\rho_f \approx \frac{\rho_{pa} D_p' A_r}{D_c A_r} = \frac{\rho_{pa} D_p'}{D_c}$$ (4)

where, $D_p' = D_c - D_s$ , when the beads were outside the spacer.

$D_p' = D_s$ , when the beads were inside the spacer.

As described in the section of <u>Apparatus and Equipment</u>, the radiation attenuations were measured and recorded on the graphic ammeter. In using the 300 scale multiplier of the count rate meter, it was necessary to calibrate the density vs. recorder reading in the manner mentioned above for several different bucking voltages. This was done so that the full range of densities, i.e., from empty column to packed bed, could be covered.

A complete correlation chart of recorder reading vs. density of bed is given in Table I. In the table:

300 I scale is for B. V. of 8170--8300 v

300 Ia scale is for B. V. of 9870--10010 v
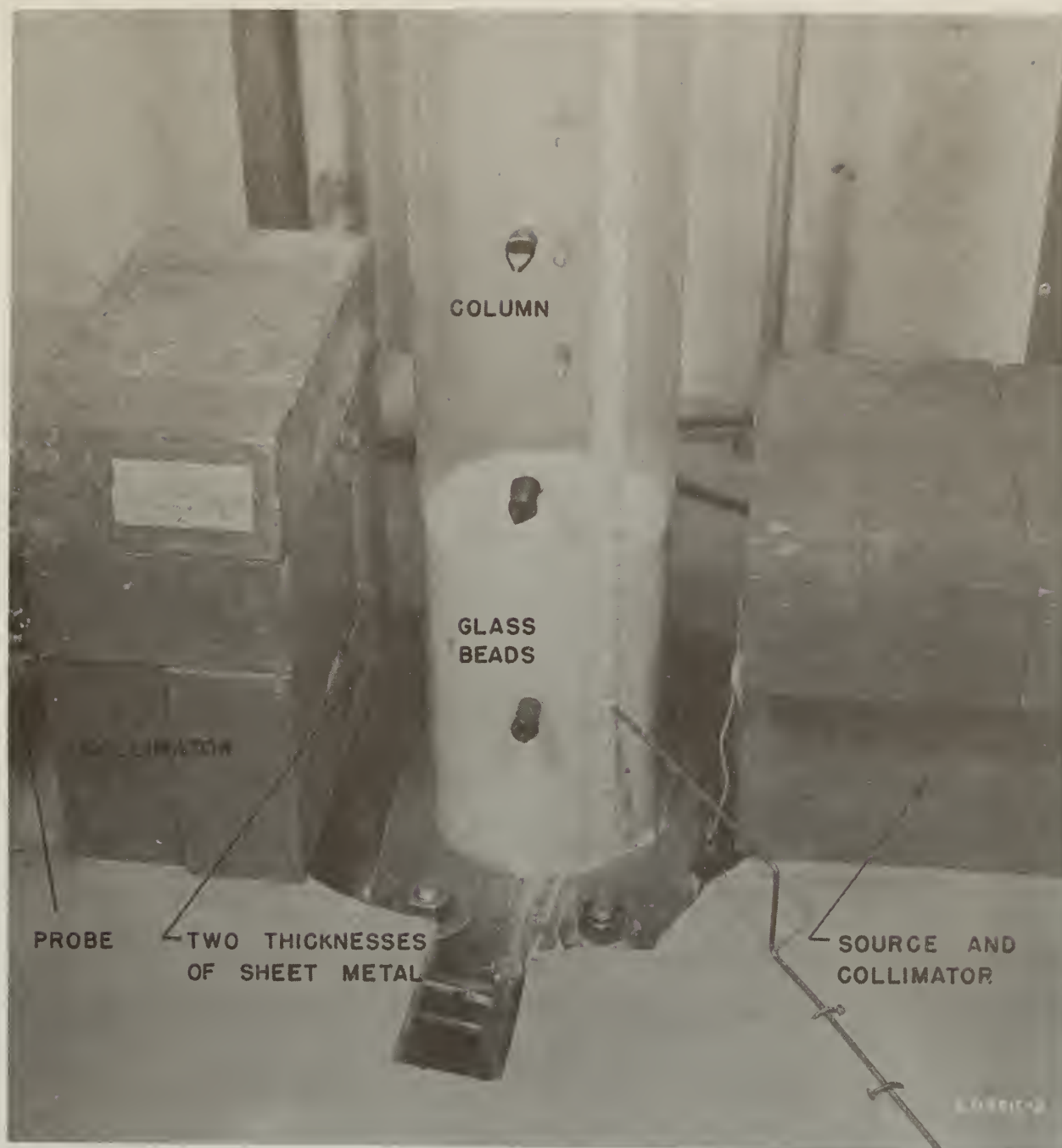
300 II scale is for B. V. of 11300--11450 v

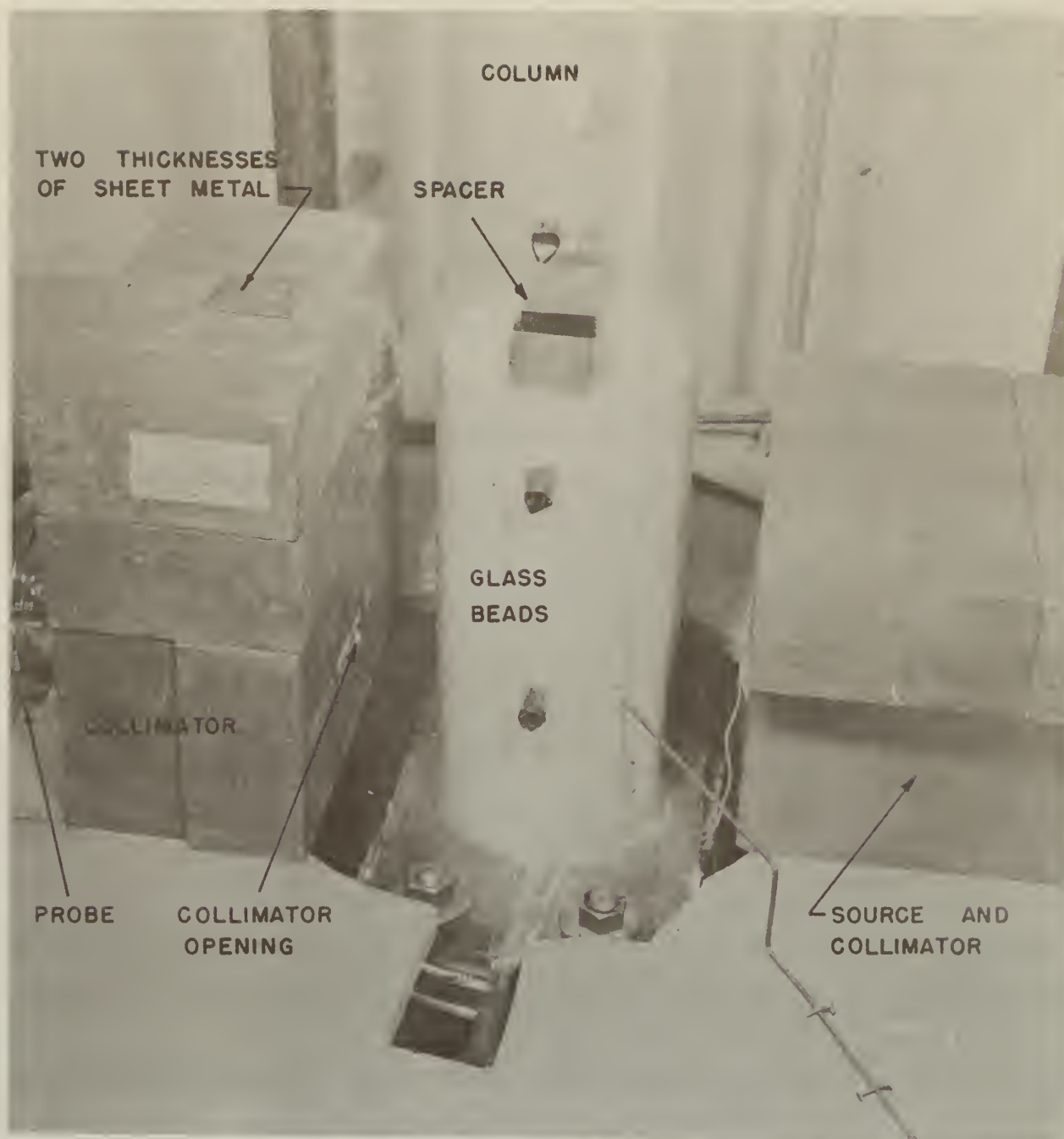Figure 4. Bed arrangement with spacer out.

Figure 5. Calibration technique with spacer inserted.
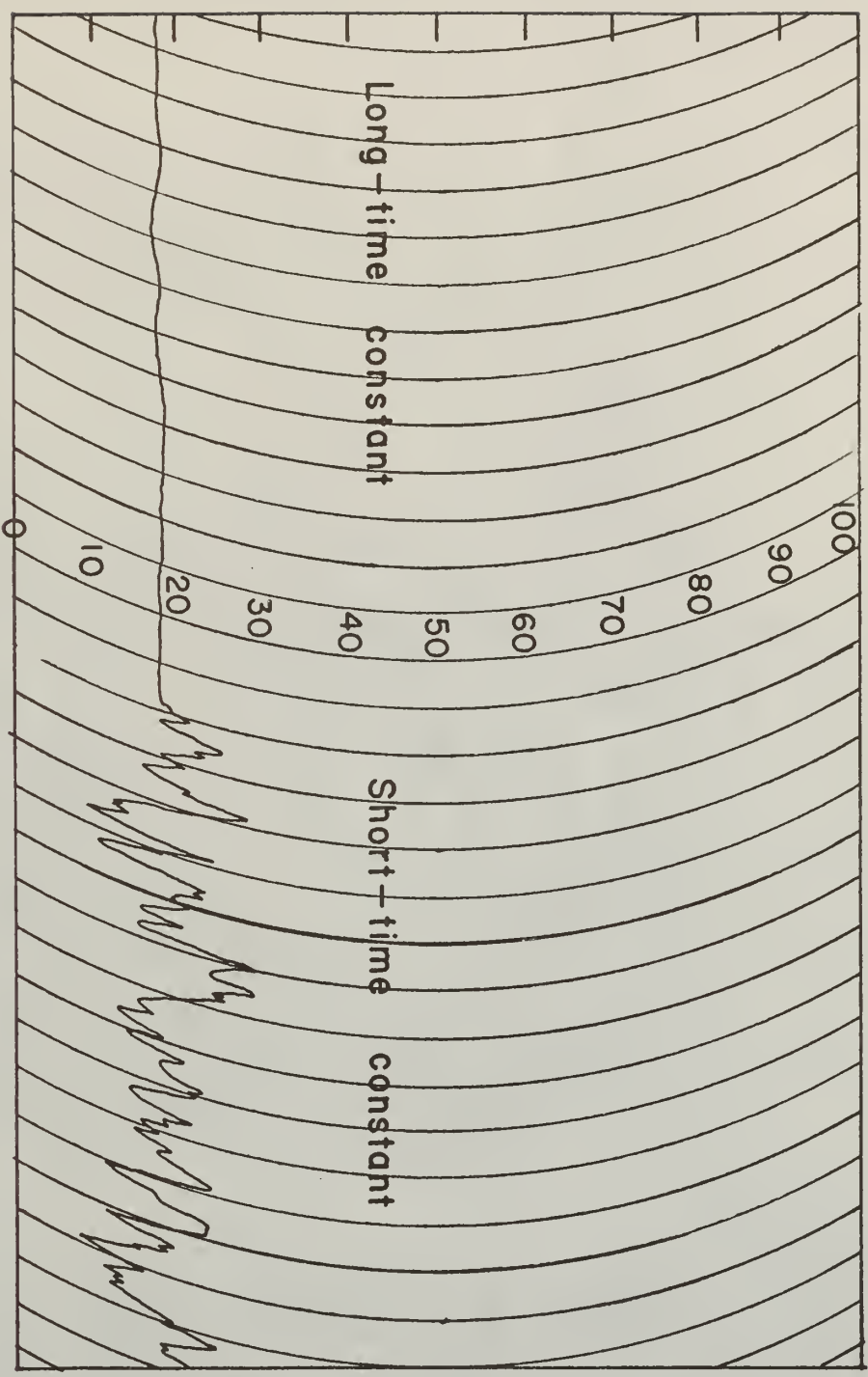
Fig. 6.  Typical recorder trace for packed bed on 300
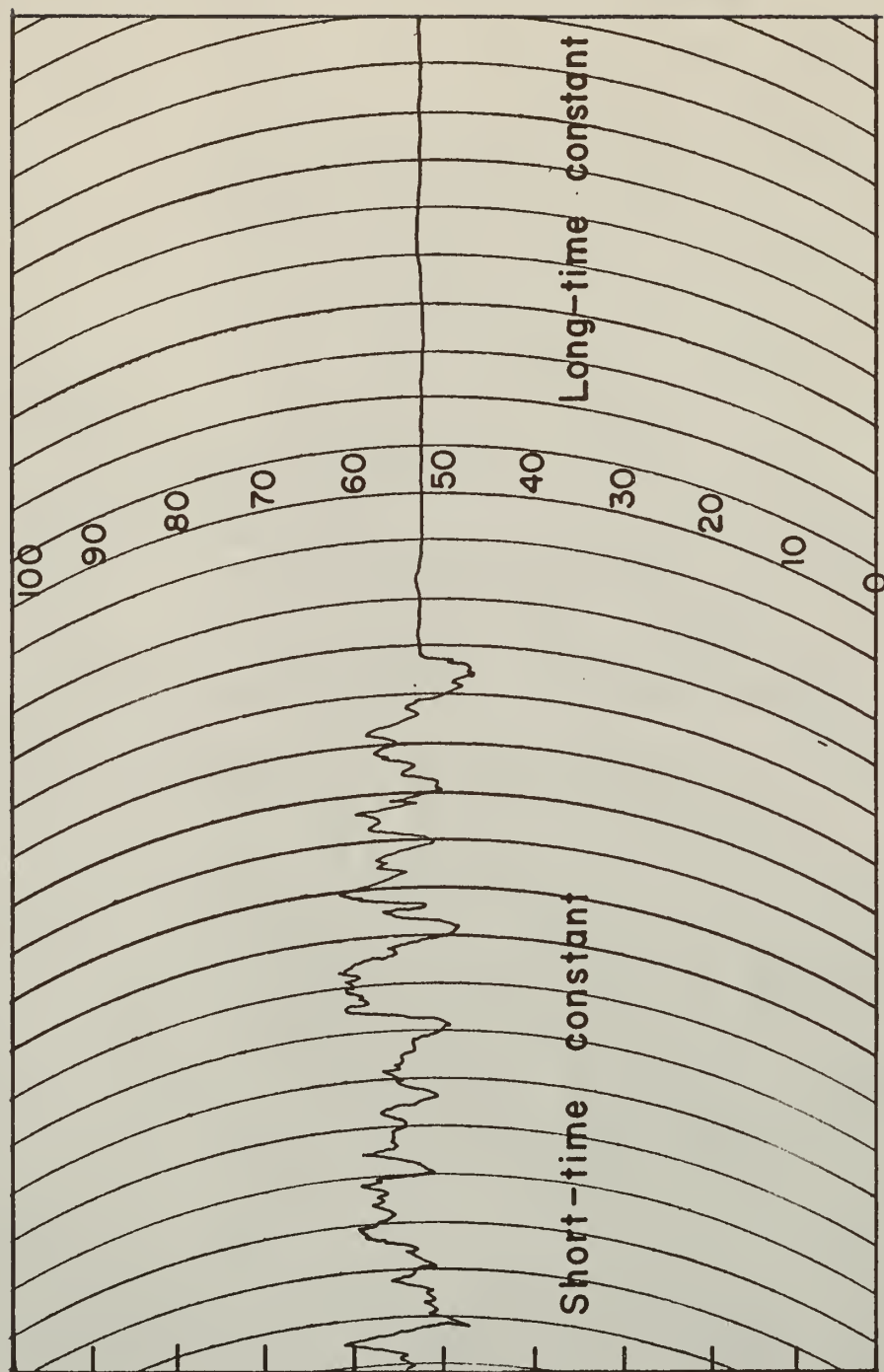I scale.

Fig. 7. Typical recorder trace for empty column on 300 III scale.

Table I. Count Rate Meter (CRM) Calibration.

300 I Scale

| CRM Reading | Density gm/cu-cm | CRM Reading | Density gm/cu-cm | CRM Reading | Density gm/cu-cm | CRM Reading | Density gm/cu-cm |
|---|---|---|---|---|---|---|---|
| 001 | 1.6300 | 026 | 1.4550 | 051 | 1.2600 | 076 | 1.0260 |
| 002 | 1.6200 | 027 | 1.4460 | 052 | 1.2500 | 077 | 1.0150 |
| 003 |  | 028 | 1.4400 | 053 | 1.2420 | 078 | 1.0050 |
| 004 | 1.6100 | 029 | 1.4330 | 054 | 1.2330 | 079 | 0.9940 |
| 005 |  | 030 | 1.4250 | 055 | 1.2250 | 080 | 0.9830 |
| 006 | 1.5950 | 031 | 1.4170 | 056 | 1.2160 | 081 | 0.9720 |
| 007 |  | 032 | 1.4100 | 057 | 1.2080 | 082 | 0.9610 |
| 008 | 1.5800 | 033 | 1.4020 | 058 | 1.2000 | 083 | 0.9490 |
| 009 |  | 034 | 1.3950 | 059 | 1.1900 | 084 | 0.9370 |
| 010 | 1.5700 | 035 | 1.3880 | 060 | 1.1810 | 085 | 0.9260 |
| 011 |  | 036 | 1.3800 | 061 | 1.1720 | 086 | 0.9150 |
| 012 | 1.5500 | 037 | 1.3720 | 062 | 1.1630 | 087 | 0.9040 |
| 013 |  | 038 | 1.3650 | 063 | 1.1550 | 088 | 0.8910 |
| 014 | 1.5350 | 039 | 1.3580 | 064 | 1.1450 | 089 | 0.8780 |
| 015 |  | 040 | 1.3500 | 065 | 1.1350 | 090 | 0.8660 |
| 016 | 1.5250 | 041 | 1.3420 | 066 | 1.1260 | 091 | 0.8540 |
| 017 |  | 042 | 1.3340 | 067 | 1.1160 | 092 | 0.8410 |
| 018 | 1.5100 | 043 | 1.3260 | 068 | 1.1070 | 093 | 0.8260 |
| 019 |  | 044 | 1.3180 | 069 | 1.0980 | 094 | 0.8110 |
| 020 | 1.5000 | 045 | 1.3100 | 070 | 1.0880 | 095 | 0.7970 |
| 021 |  | 046 | 1.3020 | 071 | 1.0780 | 096 | 0.7820 |
| 022 | 1.4850 | 047 | 1.2940 | 072 | 1.0680 | 097 | 0.7660 |
| 023 |  | 048 | 1.2850 | 073 | 1.0580 | 098 | 0.7510 |
| 024 | 1.4700 | 049 | 1.2760 | 074 | 1.0480 | 099 | 0.7350 |
| 025 |  | 050 | 1.2680 | 075 | 1.0370 | 100 | 0.7170 |

Table I. Count Rate Meter (CRM) Calibration. (Cont.)

300 Ia Scale

| CRM Reading | Density gm/cu-cm | CRM Reading | Density gm/cu-cm | CRM Reading | Density gm/cu-cm | CRM Reading | Density gm/cu-cm |
|---|---|---|---|---|---|---|---|
| 001 | 1.1270 | 026 | 0.9500 | 051 | 0.7510 | 076 | 0.5030 |
| 002 | 1.1200 | 027 | 0.9430 | 052 | 0.7430 | 077 | 0.4920 |
| 003 | 1.1140 | 028 | 0.9360 | 053 | 0.7340 | 078 | 0.4810 |
| 004 | 1.1080 | 029 | 0.9280 | 054 | 0.7250 | 079 | 0.4710 |
| 005 | 1.1000 | 030 | 0.9190 | 055 | 0.7150 | 080 | 0.4600 |
| 006 | 1.0940 | 031 | 0.9110 | 056 | 0.7050 | 081 | 0.4500 |
| 007 | 1.0870 | 032 | 0.9040 | 057 | 0.6950 | 082 | 0.4390 |
| 008 | 1.0820 | 033 | 0.8960 | 058 | 0.6850 | 083 | 0.4280 |
| 009 | 1.0740 | 034 | 0.8900 | 059 | 0.6750 | 084 | 0.4170 |
| 010 | 1.0670 | 035 | 0.8840 | 060 | 0.6650 | 085 | 0.4060 |
| 011 | 1.0600 | 036 | 0.8760 | 061 | 0.6550 | 086 | 0.3950 |
| 012 | 1.0510 | 037 | 0.8700 | 062 | 0.6450 | 087 | 0.3840 |
| 013 | 1.0430 | 038 | 0.8620 | 063 | 0.6360 | 088 | 0.3730 |
| 014 | 1.0350 | 039 | 0.8540 | 064 | 0.6260 | 089 | 0.3620 |
| 015 | 1.0280 | 040 | 0.8450 | 065 | 0.6160 | 090 | 0.3500 |
| 016 | 1.0210 | 041 | 0.8370 | 066 | 0.6060 | 091 | 0.3400 |
| 017 | 1.0140 | 042 | 0.8300 | 067 | 0.5960 | 092 | 0.3300 |
| 018 | 1.0070 | 043 | 0.8210 | 068 | 0.5860 | 093 | 0.3190 |
| 019 | 1.000 | 044 | 0.8130 | 069 | 0.5760 | 094 | 0.3070 |
| 020 | 0.9920 | 045 | 0.8050 | 070 | 0.5660 | 095 | 0.2950 |
| 021 | 0.9860 | 046 | 0.7960 | 071 | 0.5560 | 096 | 0.2830 |
| 022 | 0.9800 | 047 | 0.7870 | 072 | 0.5450 | 097 | 0.2700 |
| 023 | 0.9720 | 048 | 0.7780 | 073 | 0.5350 | 098 | 0.2560 |
| 024 | 0.9650 | 049 | 0.7700 | 074 | 0.5240 | 099 | 0.2400 |
| 025 | 0.9570 | 050 | 0.7610 | 075 | 0.5140 | 100 | 0.2250 |

Table I.  Count Rate Meter (CRM) Calibration.  (Cont.)

300 II Scale

| CRM Reading | Density gm/cu-cm | CRM Reading | Density gm/cu-cm | CRM Reading | Density gm/cu-cm | CRM Reading | Density gm/cu-cm |
|---|---|---|---|---|---|---|---|
| 001 | 0.8860 | 026 | 0.6940 | 051 | 0.4810 | 076 | 0.2300 |
| 002 | 0.8800 | 027 | 0.6860 | 052 | 0.4720 | 077 | 0.2190 |
| 003 | 0.8730 | 028 | 0.6780 | 053 | 0.4630 | 078 | 0.2090 |
| 004 | 0.8660 | 029 | 0.6700 | 054 | 0.4540 | 079 | 0.1970 |
| 005 | 0.8590 | 030 | 0.6620 | 055 | 0.4450 | 080 | 0.1850 |
| 006 | 0.8510 | 031 | 0.6540 | 056 | 0.4350 | 081 | 0.1750 |
| 007 | 0.8430 | 032 | 0.6450 | 057 | 0.4250 | 082 | 0.1640 |
| 008 | 0.8360 | 033 | 0.6360 | 058 | 0.4150 | 083 | 0.1530 |
| 009 | 0.8280 | 034 | 0.6260 | 059 | 0.4050 | 084 | 0.1420 |
| 010 | 0.8210 | 035 | 0.6180 | 060 | 0.3950 | 085 | 0.1310 |
| 011 | 0.8140 | 036 | 0.6100 | 061 | 0.3850 | 086 | 0.1200 |
| 012 | 0.8060 | 037 | 0.6020 | 062 | 0.3650 | 087 | 0.1090 |
| 013 | 0.7980 | 038 | 0.5950 | 063 | 0.3550 | 088 | 0.0970 |
| 014 | 0.7900 | 039 | 0.5860 | 064 | 0.3460 | 089 | 0.0850 |
| 015 | 0.7820 | 040 | 0.5770 | 065 | 0.3360 | 090 | 0.0740 |
| 016 | 0.7750 | 041 | 0.5690 | 066 | 0.3260 | 091 | 0.0640 |
| 017 | 0.7660 | 042 | 0.5610 | 067 | 0.3150 | 092 | 0.0530 |
| 018 | 0.7580 | 043 | 0.5530 | 068 | 0.3050 | 093 | 0.0400 |
| 019 | 0.7500 | 044 | 0.5440 | 069 | 0.2950 | 094 | 0.0290 |
| 020 | 0.7420 | 045 | 0.5350 | 070 | 0.2840 | 095 | 0.0160 |
| 021 | 0.7350 | 046 | 0.5250 | 071 | 0.2730 | 096 | 0.0050 |
| 022 | 0.7260 | 047 | 0.5160 | 072 | 0.2620 | 097 | 0.0 |
| 023 | 0.7180 | 048 | 0.5070 | 073 | 0.2510 | 098 | 0.0 |
| 024 | 0.7100 | 049 | 0.5000 | 074 | 0.2400 | 099 | 0.0 |
| 025 | 0.7010 | 050 | 0.4900 | 075 | 0.2300 | 100 | 0.0 |

Table I.  Count Rate Meter (CRM) Calibration.  (Cont.)

300 IIa Scale

| CRM Reading | Density gm/cu-cm | CRM Reading | Density gm/cu-cm | CRM Reading | Density gm/cu-cm | CRM Reading | Density gm/cu-cm |
|---|---|---|---|---|---|---|---|
| 001 | 0.5940 | 026 | 0.4400 | 051 | 0.2640 | 076 | 0.0550 |
| 002 | 0.5880 | 027 | 0.4330 | 052 | 0.2560 | 077 | 0.0450 |
| 003 | 0.5820 | 028 | 0.4260 | 053 | 0.2480 | 078 | 0.0370 |
| 004 | 0.5760 | 029 | 0.4200 | 054 | 0.2400 | 079 | 0.0280 |
| 005 | 0.5700 | 030 | 0.4130 | 055 | 0.2330 | 080 | 0.0200 |
| 006 | 0.5650 | 031 | 0.4060 | 056 | 0.2250 | 081 | 0.0110 |
| 007 | 0.5590 | 032 | 0.3990 | 057 | 0.2170 | 082 | 0.0030 |
| 008 | 0.5540 | 033 | 0.3910 | 058 | 0.2100 | 083 | 0.0000 |
| 009 | 0.5480 | 034 | 0.3850 | 059 | 0.2010 | 084 | 0.0000 |
| 010 | 0.5420 | 035 | 0.3780 | 060 | 0.1920 | 085 | 0.0000 |
| 011 | 0.5350 | 036 | 0.3700 | 061 | 0.1840 | 086 | 0.0000 |
| 012 | 0.5300 | 037 | 0.3640 | 062 | 0.1750 | 087 | 0.0000 |
| 013 | 0.5240 | 038 | 0.3580 | 063 | 0.1660 | 088 | 0.0000 |
| 014 | 0.5170 | 039 | 0.3510 | 064 | 0.1580 | 089 | 0.0000 |
| 015 | 0.5110 | 040 | 0.3440 | 065 | 0.1500 | 090 | 0.0000 |
| 016 | 0.5050 | 041 | 0.3360 | 066 | 0.1420 | 091 | 0.0000 |
| 017 | 0.4990 | 042 | 0.3290 | 067 | 0.1340 | 092 | 0.0000 |
| 018 | 0.4920 | 043 | 0.3220 | 068 | 0.1250 | 093 | 0.0000 |
| 019 | 0.4860 | 044 | 0.3150 | 069 | 0.1150 | 094 | 0.0000 |
| 020 | 0.4800 | 045 | 0.3090 | 070 | 0.1060 | 095 | 0.0000 |
| 021 | 0.4740 | 046 | 0.3010 | 071 | 0.0990 | 096 | 0.0000 |
| 022 | 0.4670 | 047 | 0.2940 | 072 | 0.0900 | 097 | 0.0000 |
| 023 | 0.4600 | 048 | 0.2870 | 073 | 0.0810 | 098 | 0.0000 |
| 024 | 0.4530 | 049 | 0.2800 | 074 | 0.0720 | 099 | 0.0000 |
| 025 | 0.4470 | 050 | 0.2720 | 075 | 0.0640 | 100 | 0.0000 |

Table I.  Count Rate Meter (CRM) Calibration.  (Cont.)

300 III Scale

| CRM Reading | Density gm/cu-cm | CRM Reading | Density gm/cu-cm | CRM Reading | Density gm/cu-cm | CRM Reading | Density gm/cu-cm |
|---|---|---|---|---|---|---|---|
| 001 | 0.3380 | 026 | 0.1870 | 051 | 0.0200 | 076 | --- |
| 002 | 0.3310 | 027 | 0.1800 | 052 | 0.0140 | 077 | --- |
| 003 | 0.3260 | 028 | 0.1730 | 053 | 0.0060 | 078 | --- |
| 004 | 0.3200 | 029 | 0.1670 | 054 | 0.0000 | 079 | --- |
| 005 | 0.3150 | 030 | 0.1610 | 055 | --- | 080 | --- |
| 006 | 0.3090 | 031 | 0.1540 | 056 | --- | 081 | --- |
| 007 | 0.3030 | 032 | 0.1470 | 057 | --- | 082 | --- |
| 008 | 0.2970 | 033 | 0.1400 | 058 | --- | 083 | --- |
| 009 | 0.2910 | 034 | 0.1350 | 059 | --- | 084 | --- |
| 010 | 0.2850 | 035 | 0.1280 | 060 | --- | 085 | --- |
| 011 | 0.2790 | 036 | 0.1210 | 061 | --- | 086 | --- |
| 012 | 0.2730 | 037 | 0.1150 | 062 | --- | 087 | --- |
| 013 | 0.2670 | 038 | 0.1090 | 063 | --- | 088 | --- |
| 014 | 0.2600 | 039 | 0.1020 | 064 | --- | 089 | --- |
| 015 | 0.2540 | 040 | 0.0950 | 065 | --- | 090 | --- |
| 016 | 0.2490 | 041 | 0.0880 | 066 | --- | 091 | --- |
| 017 | 0.2430 | 042 | 0.0820 | 067 | --- | 092 | --- |
| 018 | 0.2370 | 043 | 0.0760 | 068 | --- | 093 | --- |
| 019 | 0.2310 | 044 | 0.0690 | 069 | --- | 094 | --- |
| 020 | 0.2250 | 045 | 0.0620 | 070 | --- | 095 | --- |
| 021 | 0.2180 | 046 | 0.0550 | 071 | --- | 096 | --- |
| 022 | 0.2120 | 047 | 0.0490 | 072 | --- | 097 | --- |
| 023 | 0.2060 | 048 | 0.0410 | 073 | --- | 098 | --- |
| 024 | 0.2000 | 049 | 0.0340 | 074 | --- | 099 | --- |
| 025 | 0.1930 | 050 | 0.0270 | 075 | --- | 100 | --- |

300 IIa scale is for B. V. of 12100--12220 v

300 III scale is for B. V. of 13100--13330 v

Fig. 6 and Fig. 7 are two typical tracings of the CRM recorder on 300 I scale and 300 III scale respectively.

Rotameter Calibration. The linear flow velocity of the air was measured by a rotameter of Brooks Rotameter Co. R-9M-25-2. Two floats and one pressure gauge were used to cover the range of flow rates used in this experiment. The aluminum float was used to measure the low flow rates, and the steel float was used to measure high flow rates. The rotameter was further calibrated by an Anemotherm (No. 1005 Mechanical Engineering, K.S.U.) for the high flow rates. For calibration in the low range, a wet test meter (WMT 4, Dept. of Chemical Engineering) was used. Five pressures of 5, 10, 15, 20, 25 psig were used as parameters. The calibration curve is presented in Fig. 8.

## Procedure

The instruments were turned on at least 4 hours, usually overnight, before a run was made. The calibration was checked to make sure that the instrumentations were stabilized. The column was charged with the desired particles. Pressure drop data were taken, increasing the air velocity from below the minimum fluidizing velocity to about 90 ft/min. The air velocity was then decreased slowly until the air velocity was zero. The static bed height was then read. The air was then set at the desired velocity. The data were taken with 300 multiplier on 30-second time constants and with the bucking voltage appropriate for the particular density range. Data were generally taken at every half inch in the bed, starting 1 inch above the distributor.

Near the top of the fluidized bed, data were taken every quarter inch.  The attenuation readings from the recorder chart were converted to average line density by the calibration table (Table I), plotted on rectangular graphs to obtain the density profile, and then the consistency test performed.

## Consistency Test

To prove that the radioactive technique used for measuring the axial solid density was satisfactory and reproducible, the consistency test for several sets of experimental data was performed.  The test was based on the principle of the conservation of mass, i.e., the actual mass of particles placed in the column should be equal to the integrated area of the solid-density profile.

For most runs the results obtained by this consistency test were within the allowable error.  The procedure and the calculation method of this consistency test are as follows:

The area under the curve shown in Fig. 9 was graphically integrated by means of a planimeter.  The total mass of particles determined in this manner is:

M' = (integrated area) x (cross sectional area of column) x
     (unit conversion constant)

If the actual mass of particles in the column is M, then the deviational error is:

$$\% \text{ error} = \frac{M' - M}{M} \times 100\%$$

Table 2 summarizes the results of this consistency test.  The positive or negative error for each run is listed.
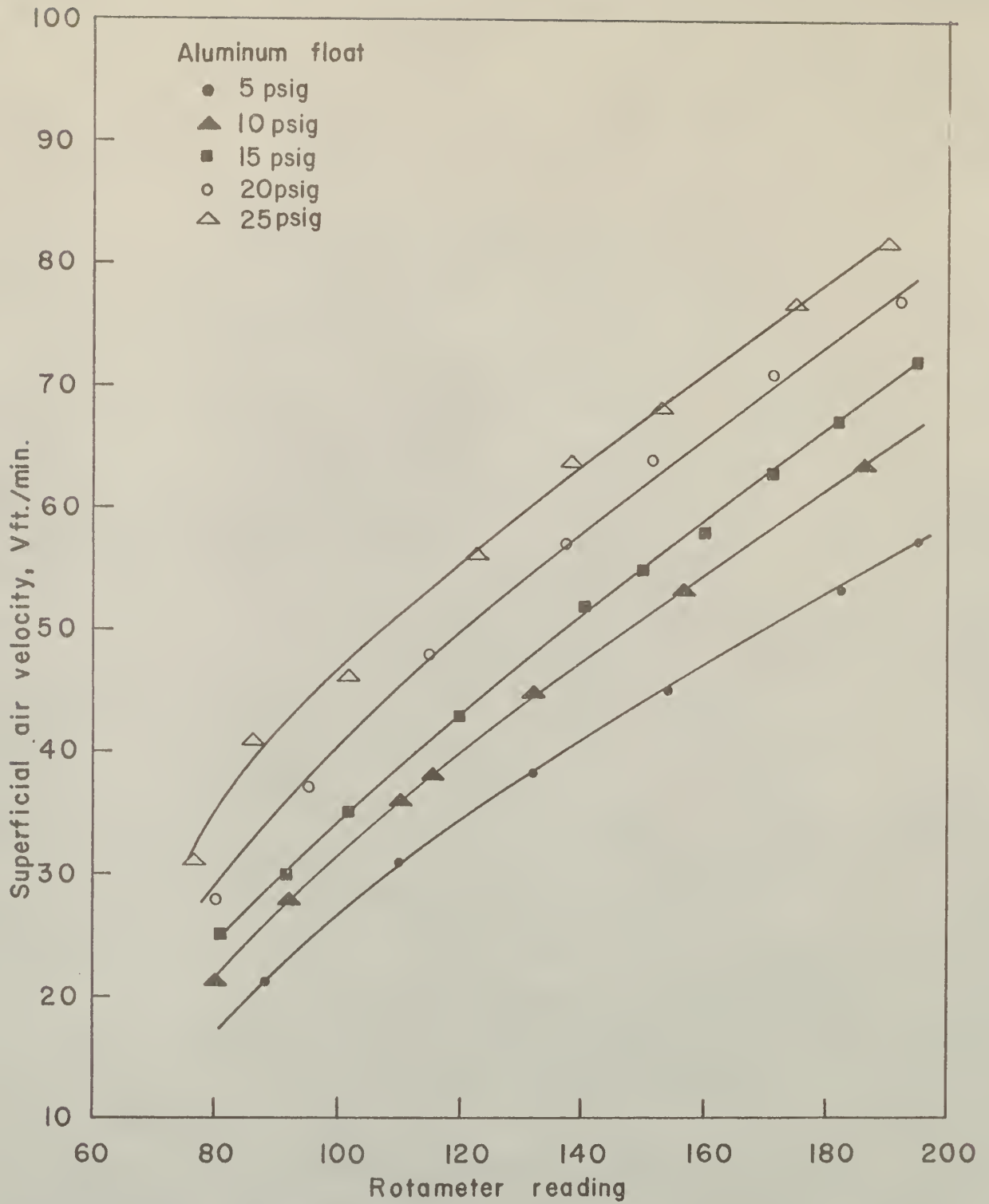
Fig. 8 Rotameter calibration

The factors which caused the error of this consistency test may be attributed to:

(a) The assumption that the average line density of solid is uniform across the cross sectional area at each axial position is not exactly valid since the density near the wall of column could be different from that in the middle of the column.

(b) There was an error due to radioactive decay or noise and other effects on the detecting power of the scintillation probe for $\gamma$-ray attenuation.

(c) When fluidizing, the particles in the bed were actually in a state of dynamic equilibrium. The line density detected is an average within the time constant used for the scintillation counting probe. Because of the complexity of the inter-particle disturbance, the speed of the particles at different locations in a certain layer could not be the same, but the time constant used for the scintillation counting probe was the same throughout. Therefore it could hardly be possible to take an exact average solid density which was consistent at any cross-section of the bed.

(d) The graphical integration must have introduced some error.

Fig. 10 shows the positive or negative percent error of this consistency test as a function of air velocity. The negative error consistently increased as the flow rate of air increased. At low flow rate of air, the error was almost negligible.

The fact that a larger error occurred at higher air velocity is logical since the particles were moving more vigorously and randomly in the bed. It might also be due to elutriation of small particles from the open top of the fluidizing column.
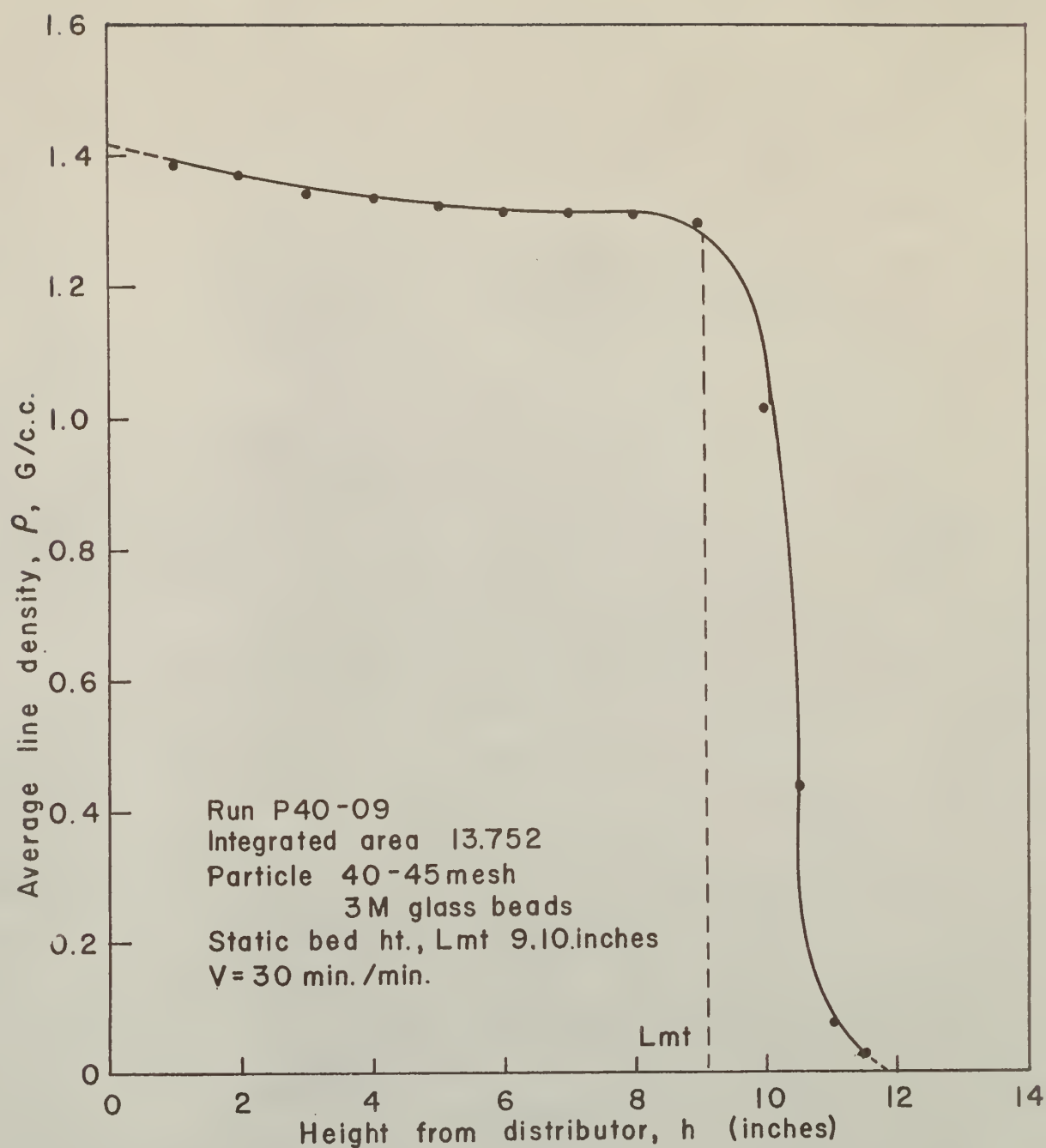
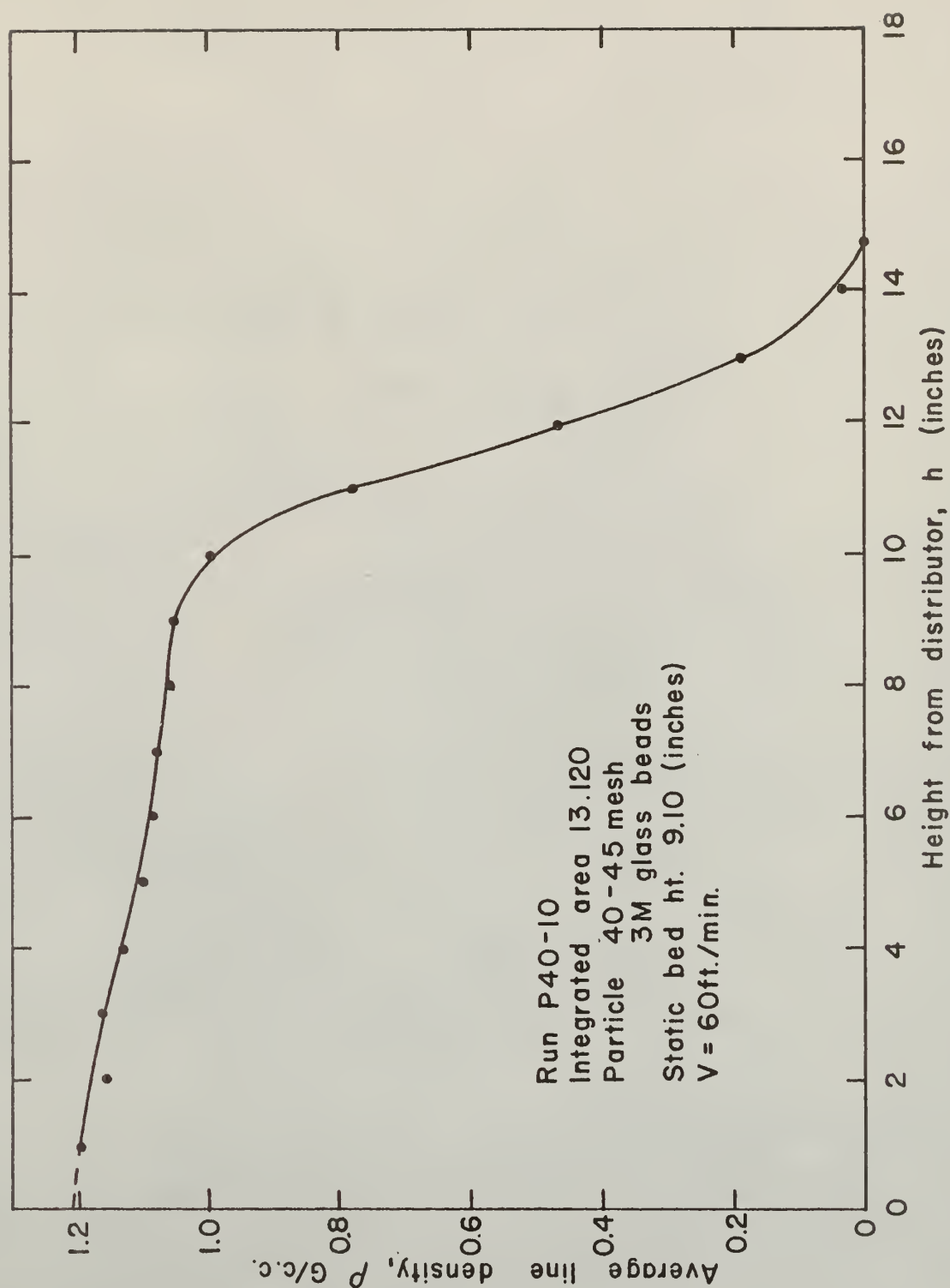Fig. 9-(a) Axial density profile of Run P40-09 for graphical integration.

Fig. 9-(b). Axial density profile of Run P40-10 for graphical integration.
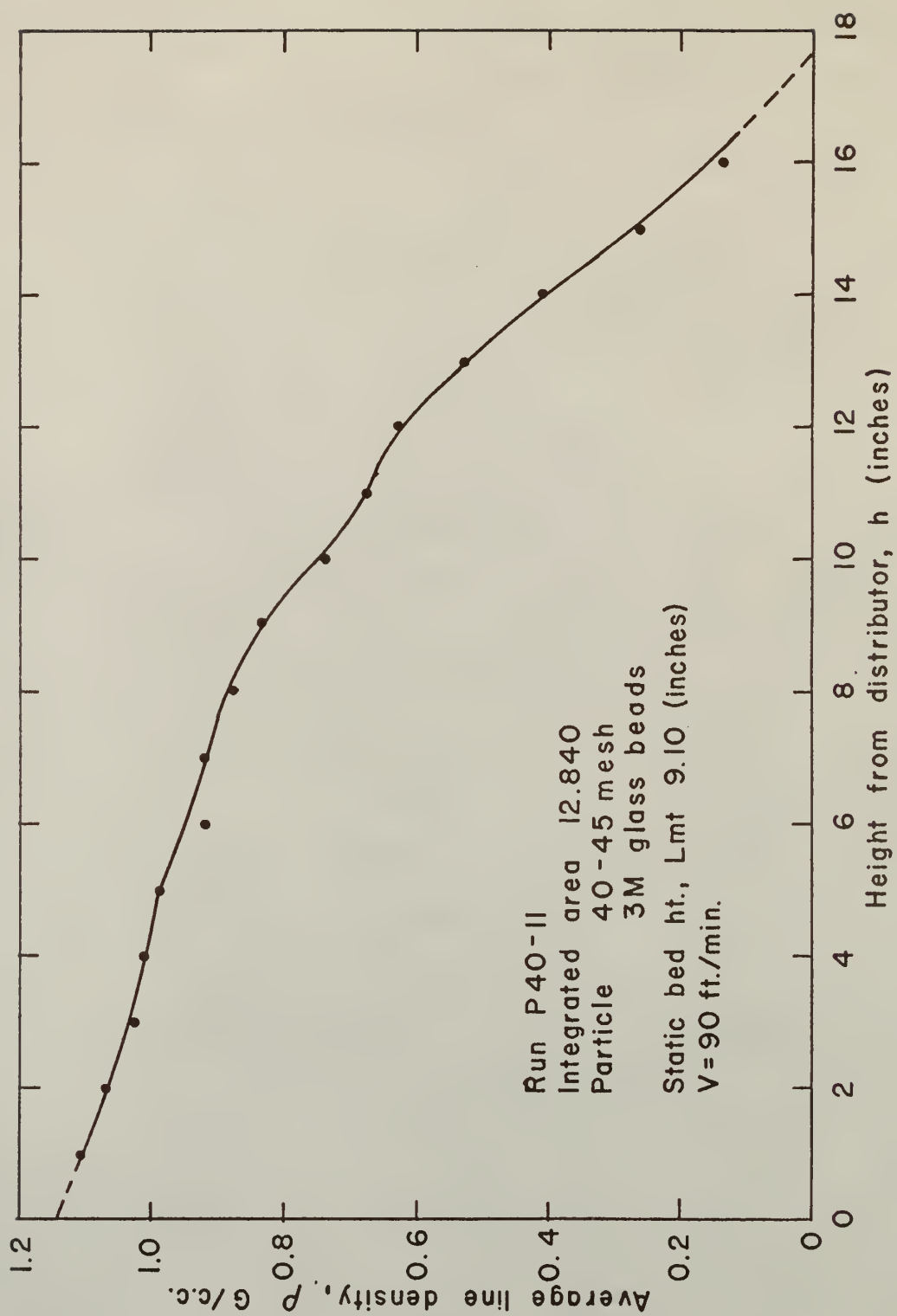
Fig. 9-(c) Axial density profile of Run P40-11 for graphical integration.

Table 2. Consistency Test.

| Run No. | St. Bed Ht. in. | Air Vel. ft./min. | Bed Wt. gram | Integrated Area | | | Bd. Wt. Integ'd | Error, % | |
|---|---|---|---|---|---|---|---|---|---|
| | | | | Below $L_{mf}$ | Above $L_{mf}$ | Total | | + | - |
| P40-05 | 6.20 | 30 | 1893.803 | 8.168 | 1.196 | 9.364 | 1904.295 | 0.55 | |
| P40-06 | 6.20 | 60 | 1893.803 | 7.872 | 1.352 | 9.224 | 1875.824 | | 0.95 |
| P40-07 | 6.20 | 90 | 1893.803 | 6.120 | 1.768 | 8.288 | 1685.476 | | 11.00 |
| | | | | | | | | | |
| P40-01 | 2.75 | 30 | 839.993 | 3.780 | 0.392 | 4.172 | 848.432 | 1.00 | |
| P40-02 | 2.75 | 60 | 839.993 | 3.342 | 0.960 | 4.302 | 874.869 | 4.15 | |
| P40-03 | 2.75 | 90 | 839.993 | 2.890 | 1.184 | 4.074 | 828.503 | | 1.370 |
| P40-04 | 2.75 | 110 | 839.993 | 2.780 | 1.360 | 4.140 | 841.925 | 0.23 | |
| | | | | | | | | | |
| P40-09 | 9.20 | 30 | 2810.158 | 12.100 | 1.612 | 13.752 | 2796.654 | | 0.480 |
| P40-10 | 9.20 | 60 | 2810.158 | 10.044 | 3.076 | 13.120 | 2668.128 | | 4.010 |
| P40-11 | 9.20 | 90 | 2810.158 | 9.008 | 3.832 | 12.840 | 2611.180 | | 6.060 |
| | | | | | | | | | |
| P80-04 | 6.10 | 30 | 1812.273 | 6.944 | 2.012 | 8.954 | 1821.323 | 0.50 | |
| P80-05 | 6.10 | 60 | 1812.273 | 5.988 | 2.388 | 8.376 | 1703.372 | | 5.230 |
| P80-06 | 6.10 | 90 | 1812.273 | 5.328 | 2.656 | 8.024 | 1631.788 | | 8.390 |
| P80-07 | 8.75 | 30 | 2599.573 | 9.720 | 2.664 | 12.384 | 2518.453 | | 3.120 |
| P80-08 | 8.75 | 60 | 2599.573 | 8.560 | 2.952 | 11.512 | 2341.120 | | 9.940 |
| | | | | | | | | | |
| P80-10 | 3.15 | 30 | 935.846 | 3.640 | 1.288 | 4.928 | 991.597 | 5.96 | |
| P80-11 | 3.15 | 60 | 935.846 | 3.190 | 1.446 | 4.636 | 942.793 | 0.74 | |
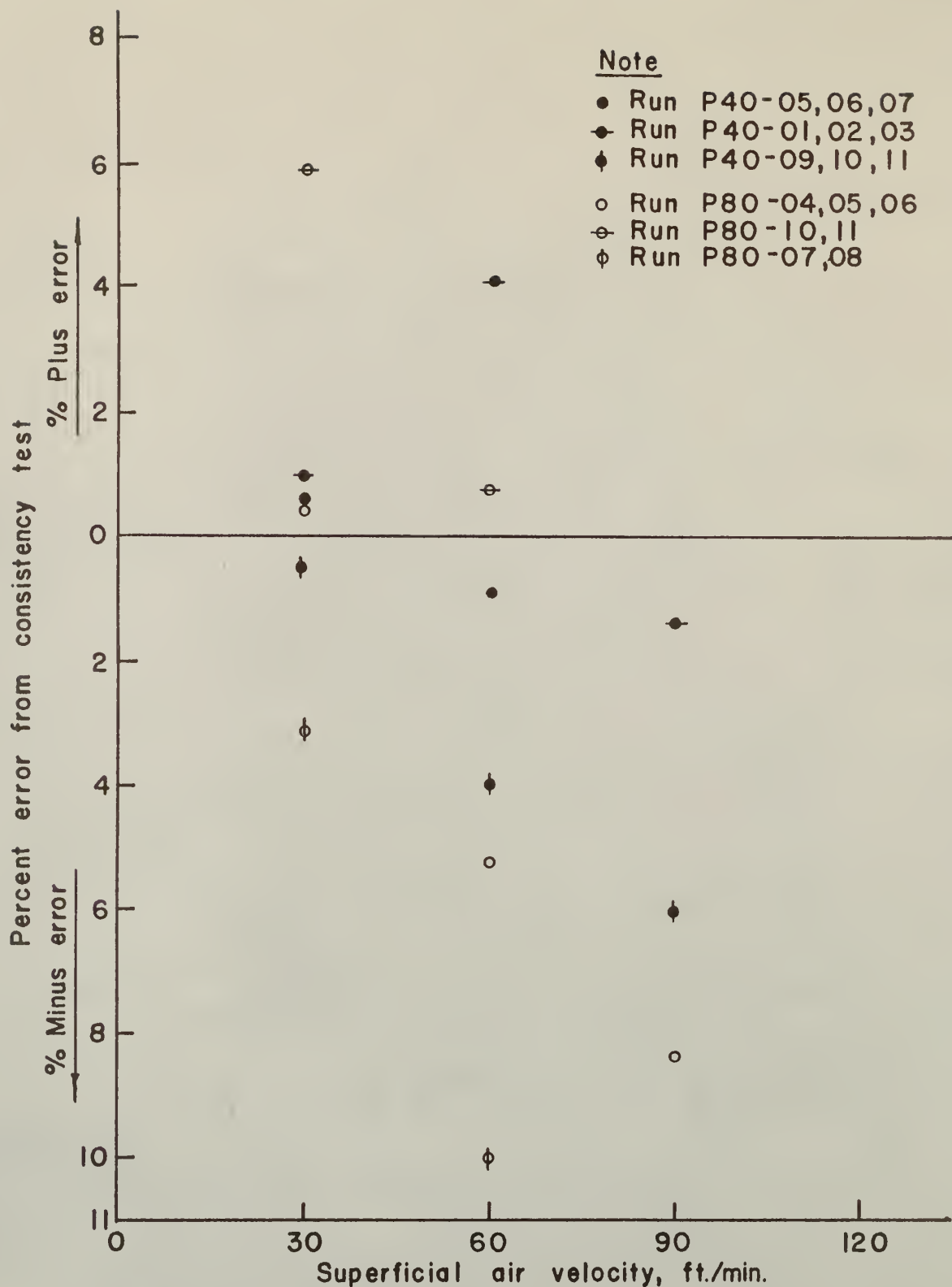
Fig. 10 Error in consistency test as a function of air velocity.

CHARACTERISTIC AXIAL DENSITY DISTRIBUTION
OF GAS-SOLID, AGGREGATIVE FLUIDIZED BEDS


General Observations


Typical characteristic axial solid density profiles of a gas-solid
fluidized bed are shown in Fig. 11 and Fig. 12. Similar profiles were
obtained for all experimental runs for different static bed heights and under
different air velocities. Even the beds mixed particles yielded similar pro-
files. Two distinct zones can be found in this typical distribution curve:
in the range AB of Fig. 11, the solid density stays fairly constant. This
is called the constant density zone. After point B the solid density decreases
sharply as the distance from the bottom of the bed increases. This portion of
the profile is called the falling density zone.

These typical density profiles show qualitatively the properties of gas-
solid fluidized beds under the effect of several operational variables: --

Dotson (5) studied the effects of five primary variables on the uni-
formity of fluidization in a 4-inch diameter column by a statistically
designed experiment. He measured the density fluctuations inside the bed by
a capacitance method and concluded that among the five variables, i.e.,
distributor, bed height, particle size, probe height and gas velocity, gas
velocity had by far the greatest effect on the uniformity, with uniformity
generally decreasing with an increasing gas velocity.

In the present study with the $\gamma$-ray technique, the capacitance probe,
which did effect the flow pattern in a fluidized bed, was not present. Thus
its effect was eliminated. Only one type of gas distributor (canvas filter
cloth) was used in all the experimental runs. Therefore, only three

operational variables were studied. The effect of these three operational
variables on the axial solid density distribution will be discussed.

## Effect of Air Velocity

Fig. 11 shows the effect of air velocity upon the fluidized bulk density
profiles. It is shown that the density in the constant density zone decreased
with increasing air velocity, but the slope of the falling density zone becomes
smaller as the air velocity increases. This was expected since more air was
passing through the bed at higher air velocity and, therefore, the bed was
expanded.

Fig. 11 also indicates that this two-zone profile becomes less apparent
as the air flow rate increases. At flow rate over 90 ft/min., the line average
density falls from the bottom of the bed to the top layer of the fluidizing bed.
In other words, when the air velocity is low the constant density zone clearly
exists and the bed is closer to the ideally expanded fixed bed. If the air
velocity is high, the air which carries the particles becomes more turbulent
and the particles are in more vigorous and randomized movement. Under these
conditions there is no section in the whole bed that has a uniform solid
density.

## Effect of Static Bed Height

Figs. 13 (a-d) are the dimensionless axial density profiles, in which
$\rho/\rho_{pa}$ was plotted against $h/h_{pa}$. It appears from these graphs that the
static bed effect on the density profile is relatively small. The dimension-
less density profiles for different static bed heights fluidizing at the same
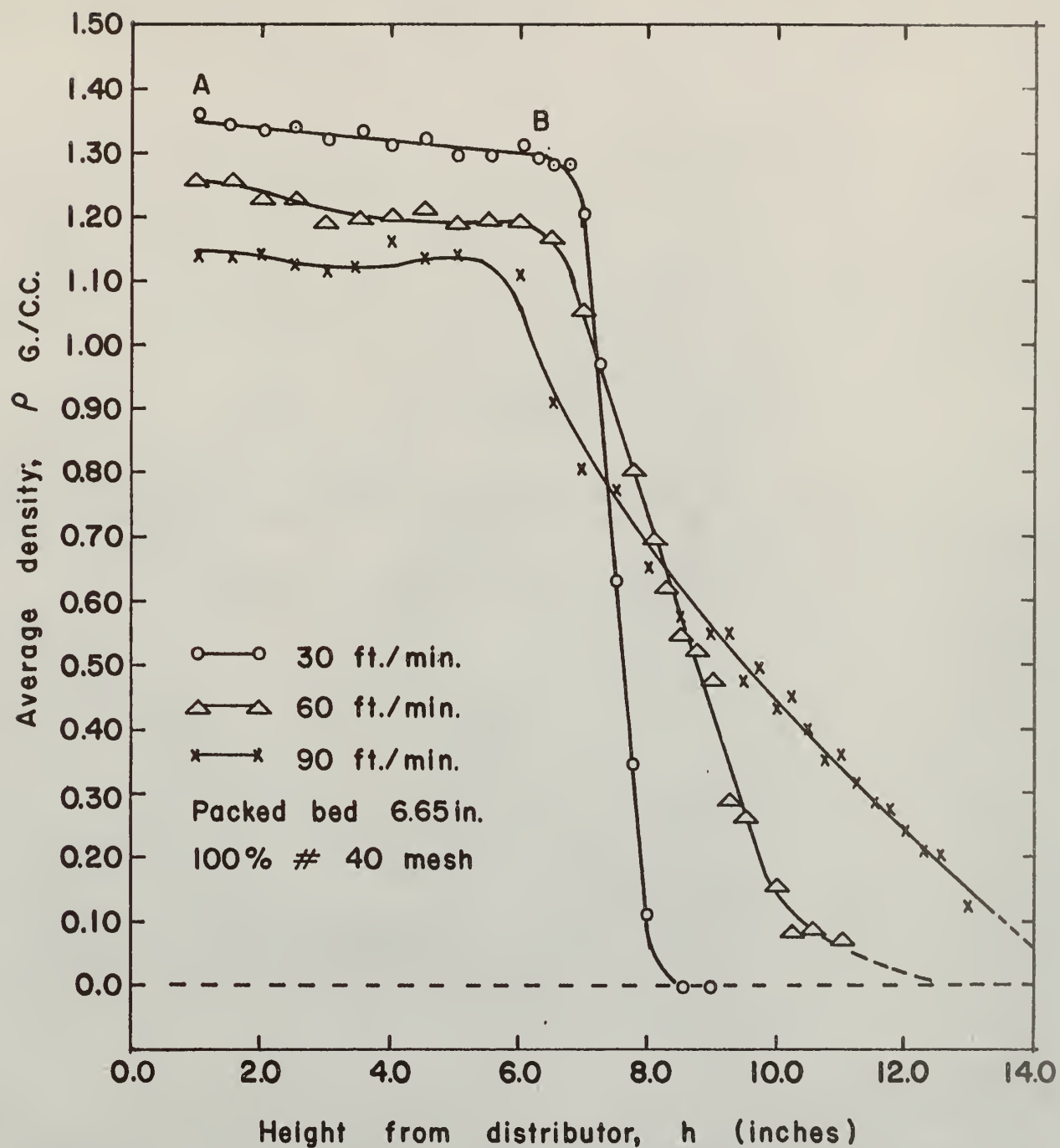
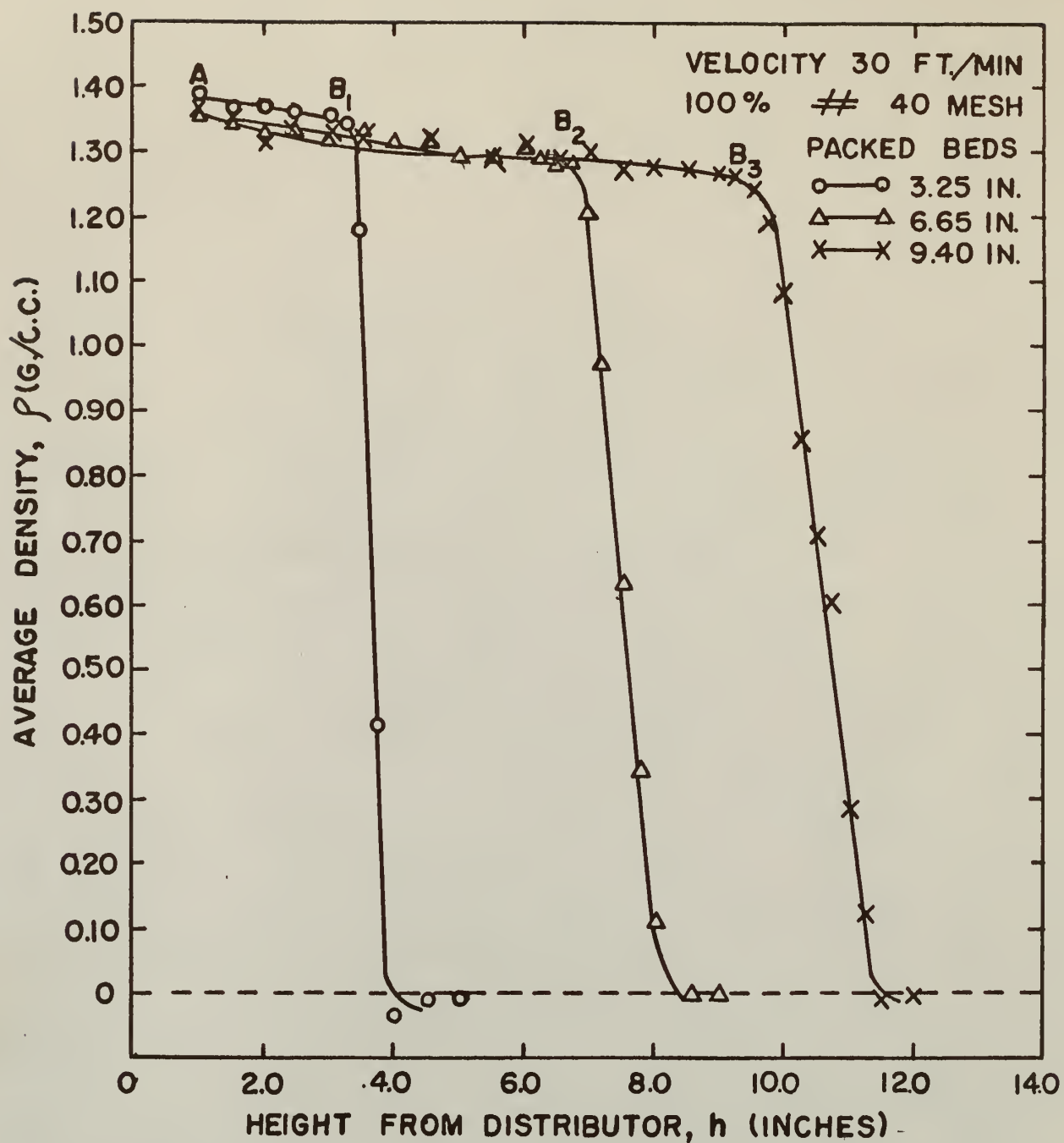Fig. 11.   Effect of air velocity upon the density profiles.

Fig. 12. Effect of static bed height upon density profiles.

air velocity can almost be represented by one curve. This is especially true
at low fluidizing air velocities. The deviations between such curves becomes
greater as the air velocity increases. The deviation from the common dimen-
sionless density profile becomes more significant for the individual profile
corresponding to the smallest bed height. This is shown in Figs. 13 (c) and
13 (d). This result may be explained as follows:

The ratio of the static bed height to the column diameter instead of
the static bed height itself is probably the significant variable affecting
the bed expansion and the density profile. This is the proper combination
of entrance and wall effects. When the bed is shallow and the ratio is small,
the air passing through could hardly have time to form well-shaped bubbles
before it leaves the fluidizing bed. The two phases of fluidization for the
shallow bed are therefore not as pronounced as in the case of deep static bed.

It may be concluded that at higher air velocity, the effect of the static
bed height on the density profile becomes more noticeable when the ratio of
static bed height to the column diameter is less than one (the diameter of
fluidizing column used was 3.9765 inch). If the ratio is greater than one,
the effect of the static bed height on the dimensionless density profile is
negligible. This is consistent with the observation made by Gomezplata
et.al.,(8). They studied the entrance effect on the conversion of the
catalytic cracking of cumene. Their results are shown in Fig. 14 to compare
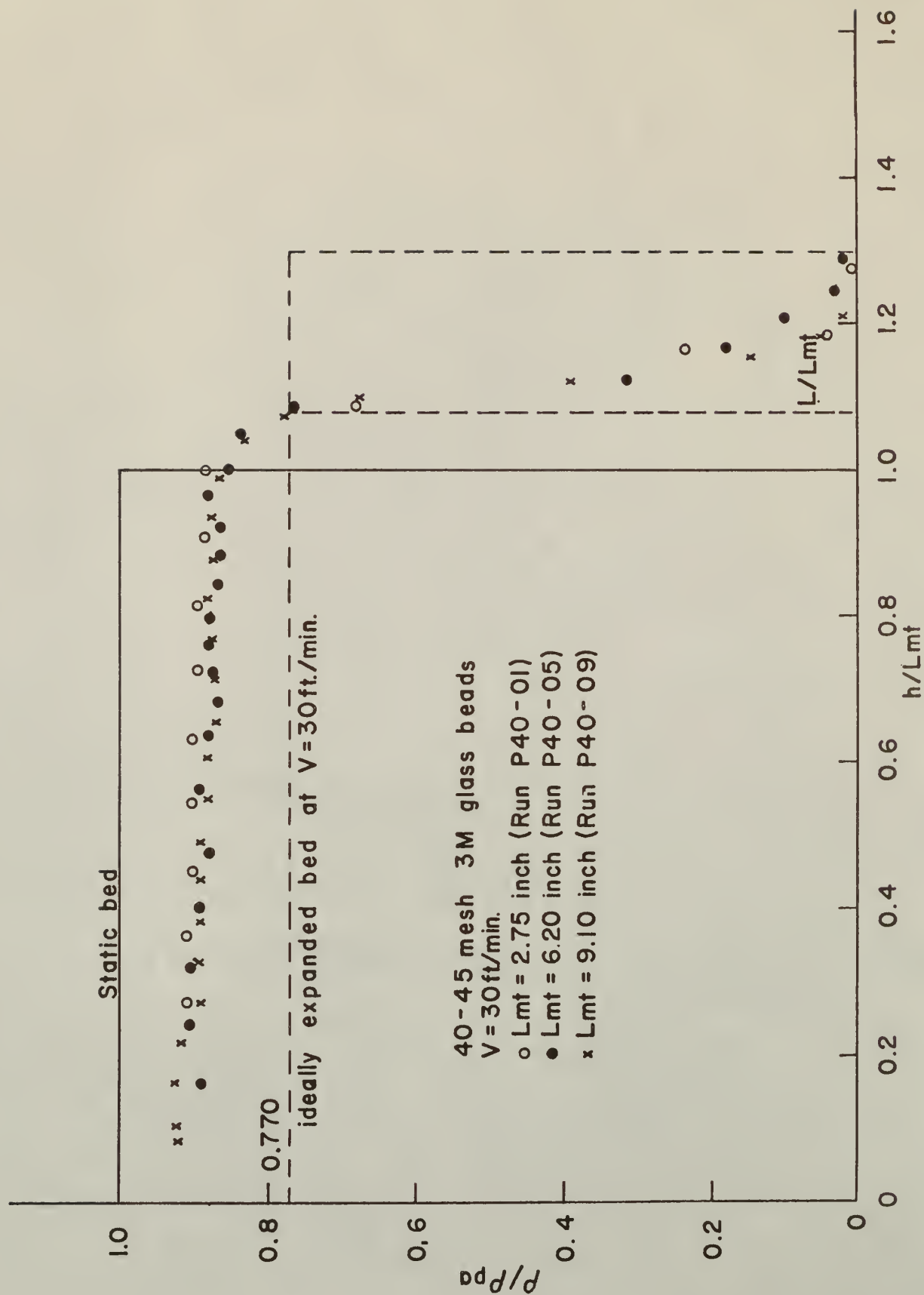with and to substantiate the present observation.

Fig. 13-(a). Dimensionles density profile at V=30ft./min for various static bed heights.

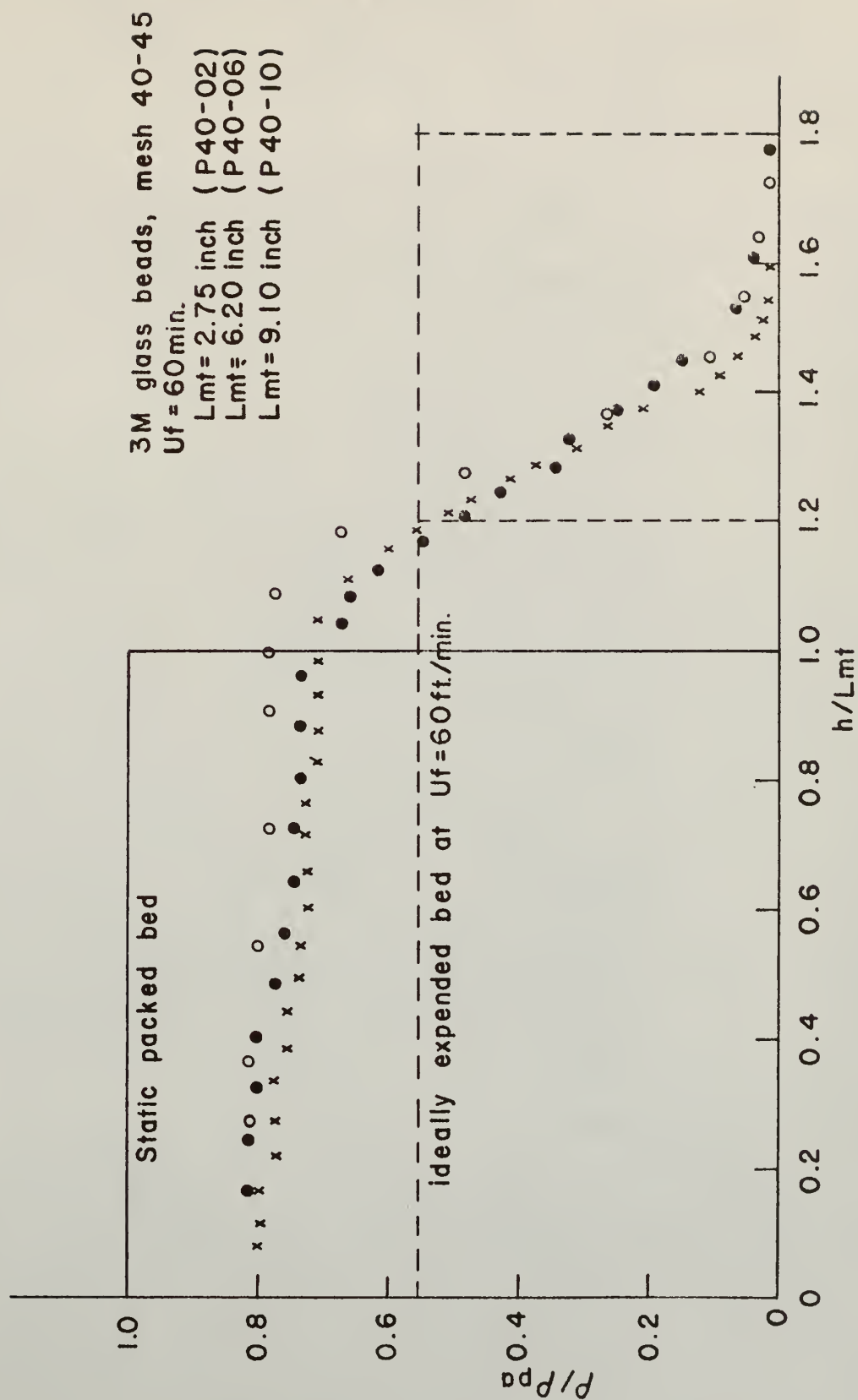40-45 mesh 3M glass beads
V=30ft./min.
o Lmf = 2.75 inch (Run P40-01)
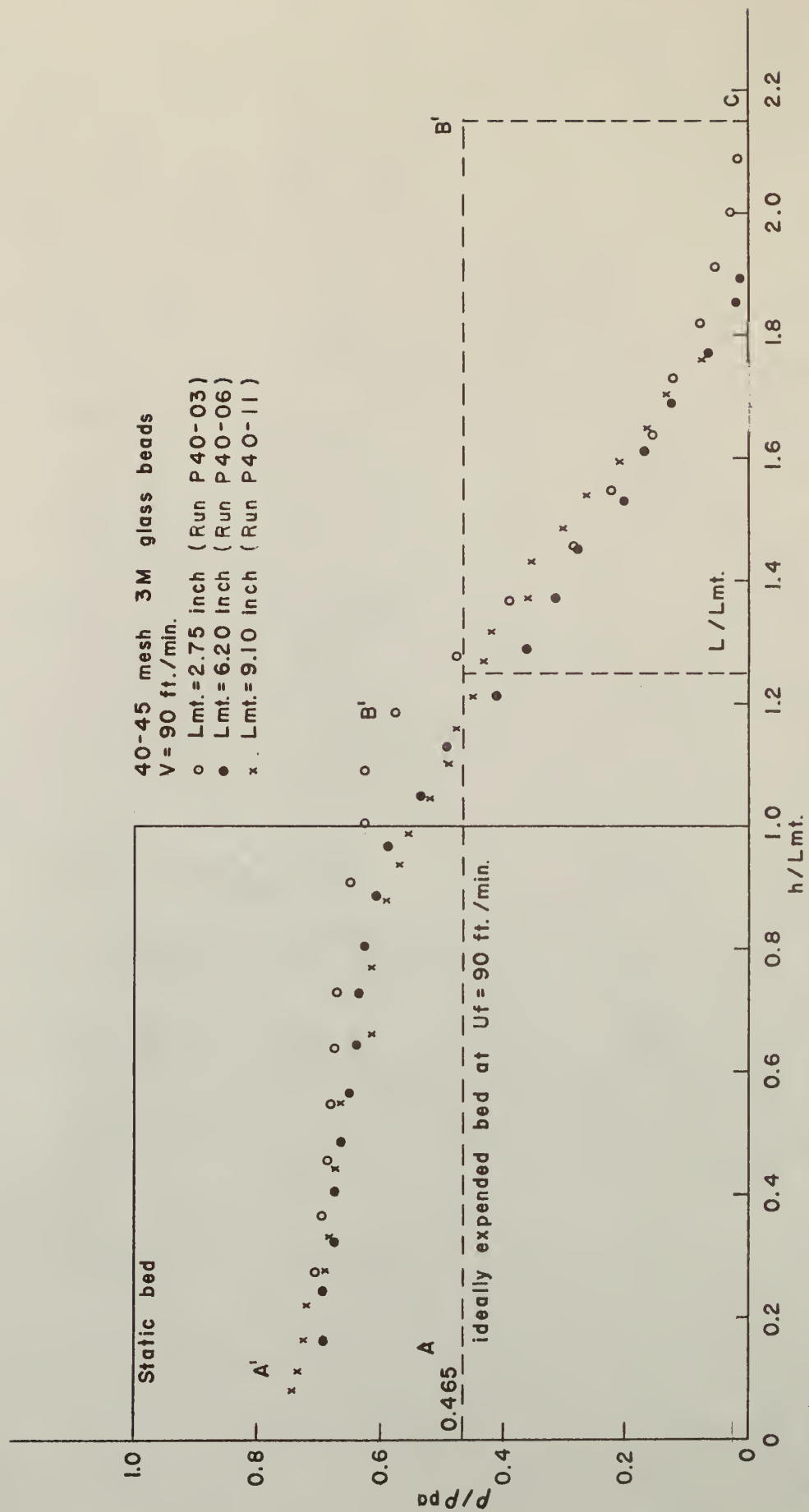● Lmf = 6.20 inch (Run P40-05)
x Lmf = 9.10 inch (Run P40-09)

Fig. 13 - (b). Dimensionless density profile at V = 60 ft./min. for various static bed height.

Fig. 13-(C)  Dimensionless density profile at V = 90 ft./min. for various static bed heights.

40-45 mesh 3M glass beads
V = 110 ft./min.

○ Lmt.= 2.75 inch ( Run P40-04 )
● Lmt.= 6.20 inch ( Run P40-07 )
× Lmt.= 9.10 inch ( Run P40-12 )
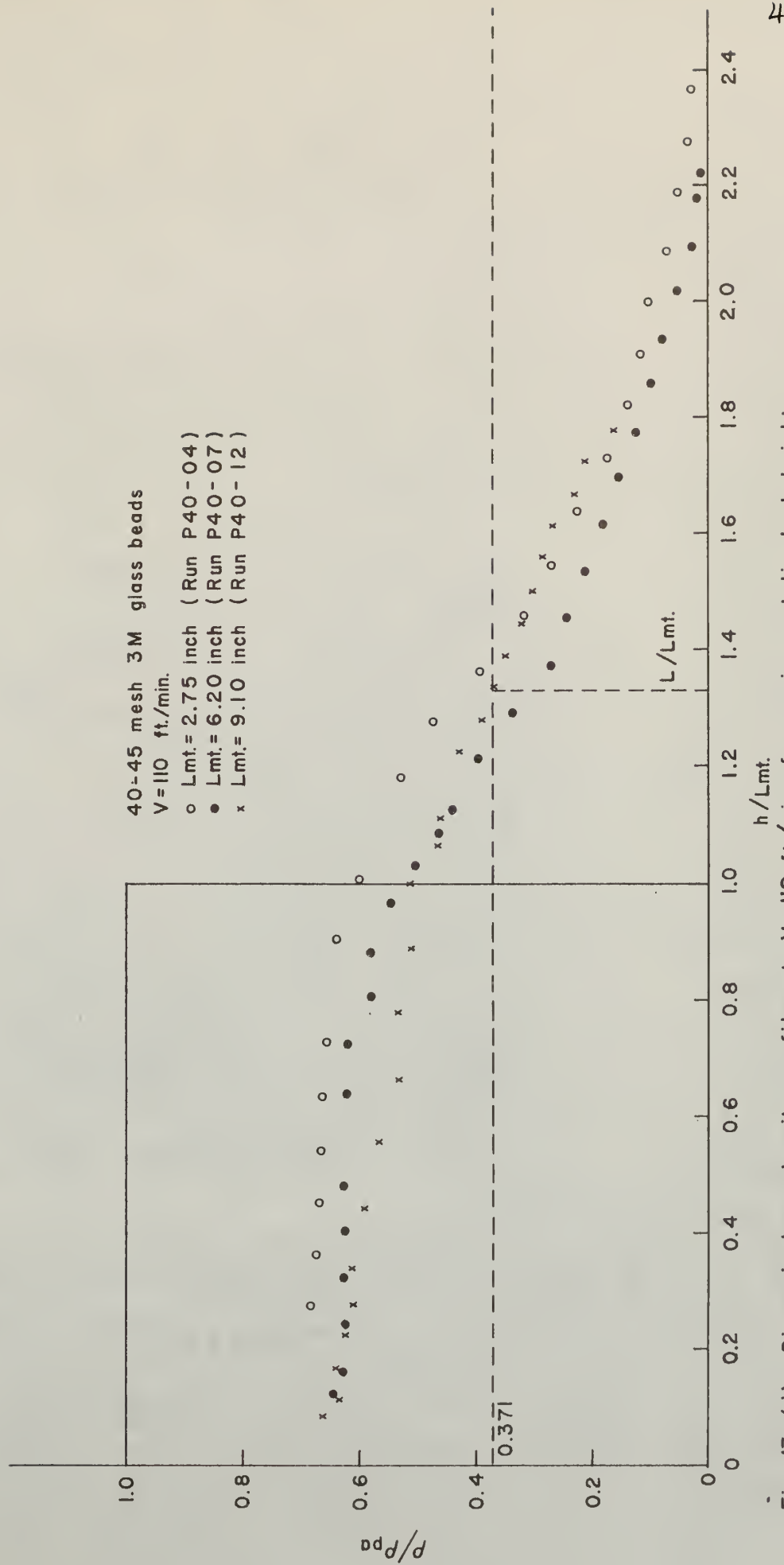
L/Lmt.

h/Lmt.

0.371

$\rho/\rho_{pa}$

Fig. 13-(d)  Dimensionless density profile at  V=110 ft./min. for various static bed heights.

## Effect of Particle Size and Bed Composition

The effect of particle size and bed composition could not be determined either qualitatively or quantitatively without defining some index for aggregative fluidization. Stewart (25) has discussed the particle size effect with a defined ISU index. His results are consistent with the findings of Dotson (5) and Baumgarten (3).

More details and quantitative discussion of the effects of operational variables on aggregative fluidization will be found in later sections.

## ANALYSIS OF DATA AND CORRELATIONS

As mentioned in the previous section, the axial density profiles may be divided into a constant density zone and a falling density zone. The correlation of the density profile as a function of the operational variables will be obtained for the two zones separately. It was usually considered (1) that the constant density zone extended from the bottom of the bed to the position corresponding to the static bed height, and the falling density zone existed above the static bed height.

### Bed Density Correlation in the
### Constant-Density Zone

The density in the constant-density zone is fairly constant, thought a considerable density fluctuation may be observed from the density profile at high air velocities. From the qualitative observation made in the previous
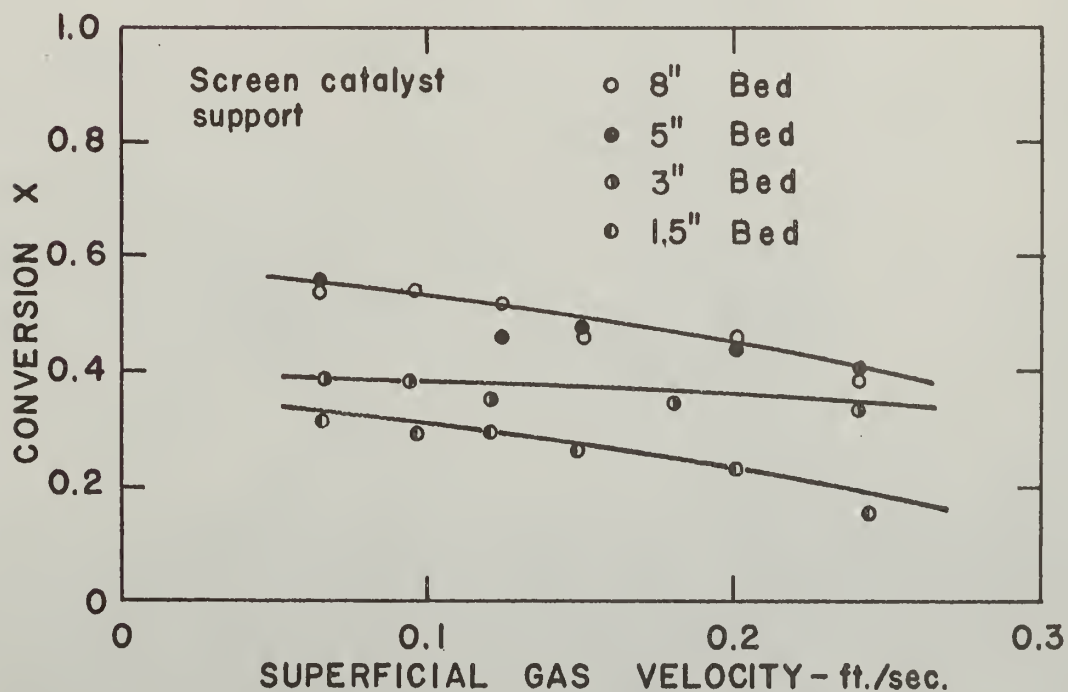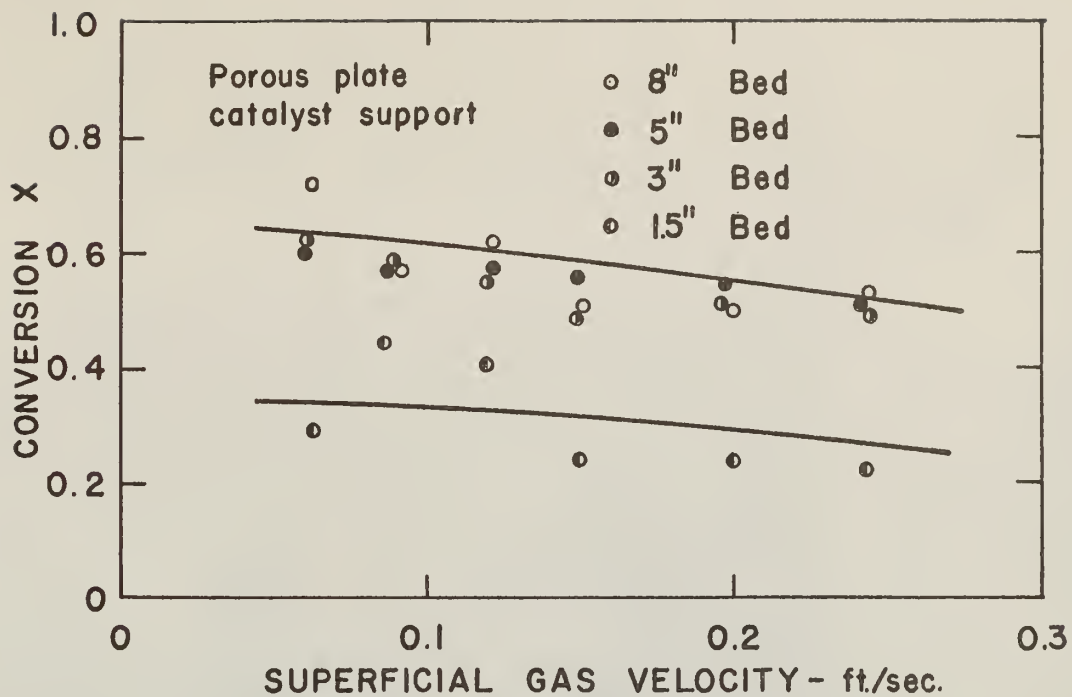
Fig. 14. Entrance effect on the conversion of cumene.
[Gomezplata & Shuster (8)]

section, we know that air velocity is the major factor affecting the shape of the density profile, whereas the static bed height has little effect. Thus the density in the constant-density zone can be correlated as a function of air velocity and particle diameter.

Let $\bar{\rho}_d$ represent the average density in the constant density zone (where the region ranges from the bottom of the column to the position corresponding to the static bed height, $L_{mf}$); $M_{s_2}$, the weight of particles fluidizing below $L_{mf}$; and A, the cross-sectional area of the fluidizing column, then:

$$\bar{\rho}_d = \frac{M_{s_2}}{A\, L_{mf}} \qquad (5)$$

The particles blown off and suspended above $L_{mf}$, are then

$$M = M_{s_1} + M_{s_2} \qquad (6)$$

where M is the total weight of particles charged in the column. It was mentioned by Bakker et.al.(2) that the volume of the particles suspended in the space above $L_{mf}$, i.e. $Vol_{s_1}$, corresponds to the product of the volume of the gas bubbles appearing below $L_{mf}$, and the concentration in the prefluidized state. Thus,

$$Vol_{s_1} = (1 - \overset{*}{\epsilon}_{mf})\, Vol_b \qquad (7)$$

If we consider that A' is the part of area A which is occupied by the dense phase emulsion, then (A - A') is the area crossed by the bubbles. The superficial velocity of bubbles, as indicated by Baumgarten et.al.(3), is a function of bubble size and is different at each layer of the fluidized bed. He observed that the size of a bubble grows as it moves away from the

* $\epsilon_{mf}$, is the void space of bed at minimum fluidizing state.

distributor. But to avoid this complexity, we can assume that there is a mean bubble velocity, $\bar{V}_b$, which is constant throughout the section below $L_{mf}$. With this assumption:

$$G = G_b + G_{mf} \tag{8}$$

where G is the volumetric air velocity, $G_b$ is the volumetric bubble velocity, and $G_{mf}$, the volumetric velocity of minimum fluidization.

Therefore, from equation (8):

$$VA = \bar{V}_b (A - A') + V_{mf} A' \tag{8'}$$

Rearranging equation (8') we get:

$$A' = \frac{A (\bar{V}_b - V)}{\bar{V}_b - V_{mf}} \tag{9}$$

Let $t_b$ be the residence time of bubbles in the bed below $L_{mf}$. Then:

$$t_b = \frac{L_{mf}}{\bar{V}_b} \tag{10}$$

The volume occupied by bubbles below $L_{mf}$ is:

$$Vol_b = G_b\, t_b = \bar{V}_b (A - A') \frac{L_{mf}}{\bar{V}_b} \tag{11}$$

Substituting equation (9) into Equation (11) gives:

$$Vol_b = L_{mf} \left[ A - \frac{A(\bar{V}_b - V)}{(\bar{V}_b - V_{mf})} \right]$$

$$= \frac{AL_{mf} (V - V_{mf})}{\bar{V}_b - V_{mf}} \tag{12}$$

From Equations (7) and (12), the volume of the solid particles above $L_{mf}$ is obtained.

$$Vol_{s_1} = \frac{AL_{mf}(V - V_{mf})}{\bar{V}_b - V_{mf}}(1 - \epsilon_{mf}) \qquad (13)$$

then,

$$M_{s_1} = \rho_s \, Vol_{s_1} = \rho_s (1 - \epsilon_{mf}) \frac{AL_{mf}(V - V_{mf})}{\bar{V}_b - V_{mf}} \qquad (14)$$

and

$$M_{s_2} = M - \frac{\rho_s (1 - \epsilon_{mf}) AL_{mf}(V - V_{mf})}{\bar{V}_b - V_{mf}} \qquad (15)$$

Substitution of Equation (15) to Equation (5) leads to:

$$\bar{\rho}_d = \frac{M_{s_2}}{AL_{mf}} = \frac{M}{AL_{mf}} - \frac{\rho_s (1 - \epsilon_{mf})}{(\bar{V}_b - V_{mf})}(V - V_{mf}) \qquad (16)$$

$$\bar{\rho}_d = \rho_{mf} - \frac{\rho_s (1 - \epsilon_{mf})}{(\bar{V}_b - V_{mf})}(V - V_{mf})$$

since,

$$1 - \epsilon_{mf} \doteqdot \frac{\rho_{mf}}{\rho_s}$$

then,

$$\bar{\rho}_d = \rho_{mf} - \frac{\rho_{mf}}{(\bar{V}_b - V_{mf})}(V - V_{mf})$$

$$= \rho_{mf} - C(V - V_{mf}) \qquad (17)$$

where $C = \dfrac{\rho_{mf}}{(\bar{V}_b - V_{mf})}$

Since the average bubble velocity through the bed below $L_{mf}$ has been assumed constant, C in equation (17) is a constant and the average density in the constant density zone has a linear relationship with the superficial air velocity.

The data plotted on Fig. 15 (a) and Fig. 15 (b) confirm this linear relationship between $\bar{\rho}_d$ and $(V - V_{mf})$ fairly well with the static bed height showing a negligible effect.

Using the least squares method, the intercepts and slopes of the straight lines from the experimental data were obtained. The empirical equations which relate $\bar{\rho}_d$ with $(V - V_{mf})$ for 40-45 mesh and 80-100 mesh 3M glass beads are as follows:

(i)   For 40-45 mesh glass beads:

$$\bar{\rho}_d = 1.371 - 0.00536 \, (V - V_{mf, \; 40 \; mesh})$$

(ii)   For 80-100 mesh glass beads:

$$\bar{\rho}_d = 1.269 - 0.00439 \, (V - V_{mf, \; 80 \; mesh})$$

where $\bar{\rho}_d$ is in gm/cu-cm

V, $V_{mf}$ are in ft/min

$V_{mf, \; 40 \; mesh}$ is the minimum velocity of fluidization of 40-45 mesh glass beads with air, which is 24.3 ft/min

$V_{mf, \; 80 \; mesh}$ is the minimum velocity of fluidization of 80-100 mesh glass beads with air, which is 4.89 ft/min

Bed Density Correlation in the
Falling Density Zone

The fluidized bulk density in this zone decreases as the height from distributor increases. In all cases, as has been shown in Fig. 13, the density distribution in this falling density zone may be represented by a probability function. For the experimental runs at low air velocity, the density distribution in this falling zone can be fitted almost exactly by the one-tailed normal distribution function, if we consider that the
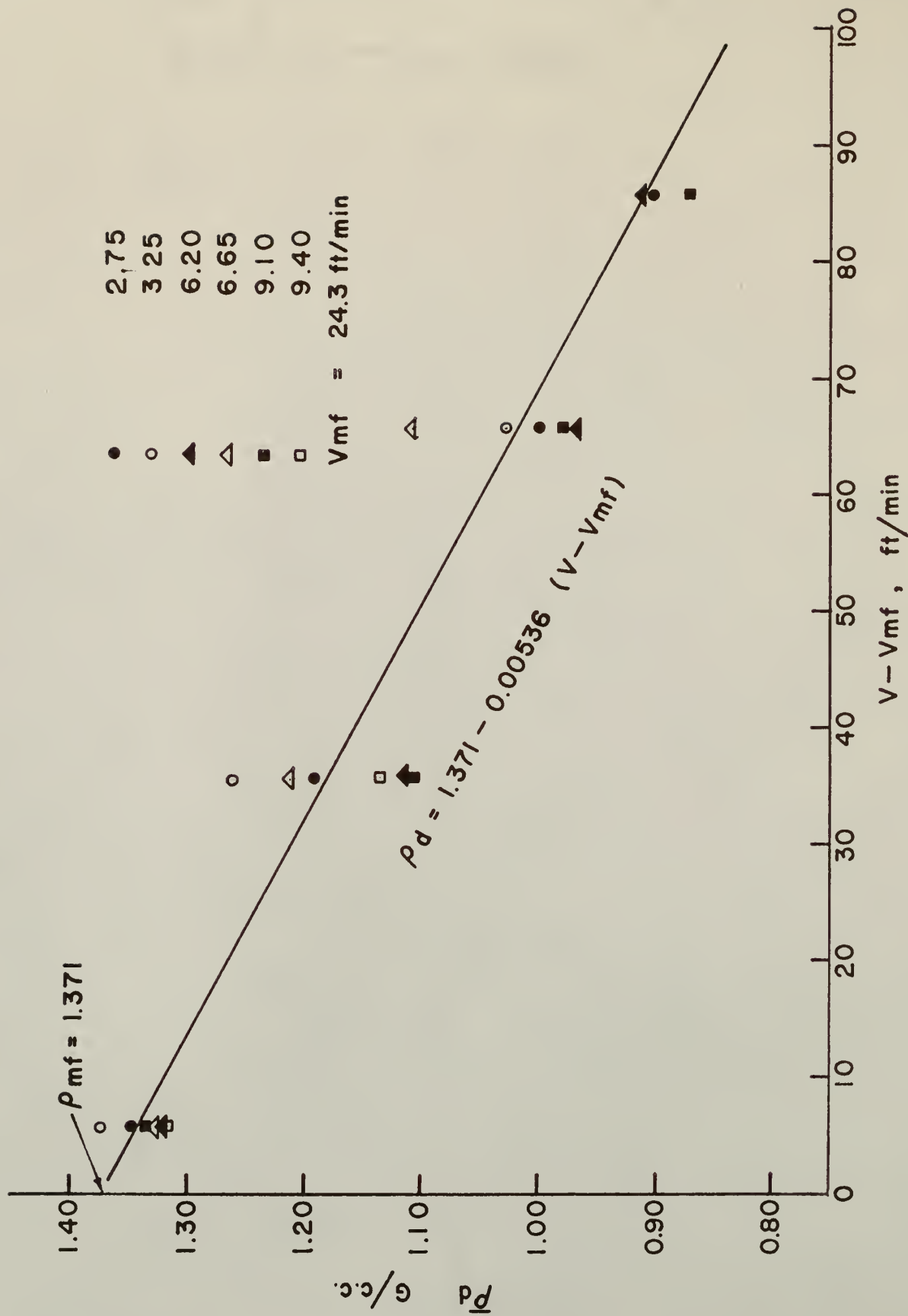
47



Fig. 15-a.   Correlation for 40-45 mesh glass beads
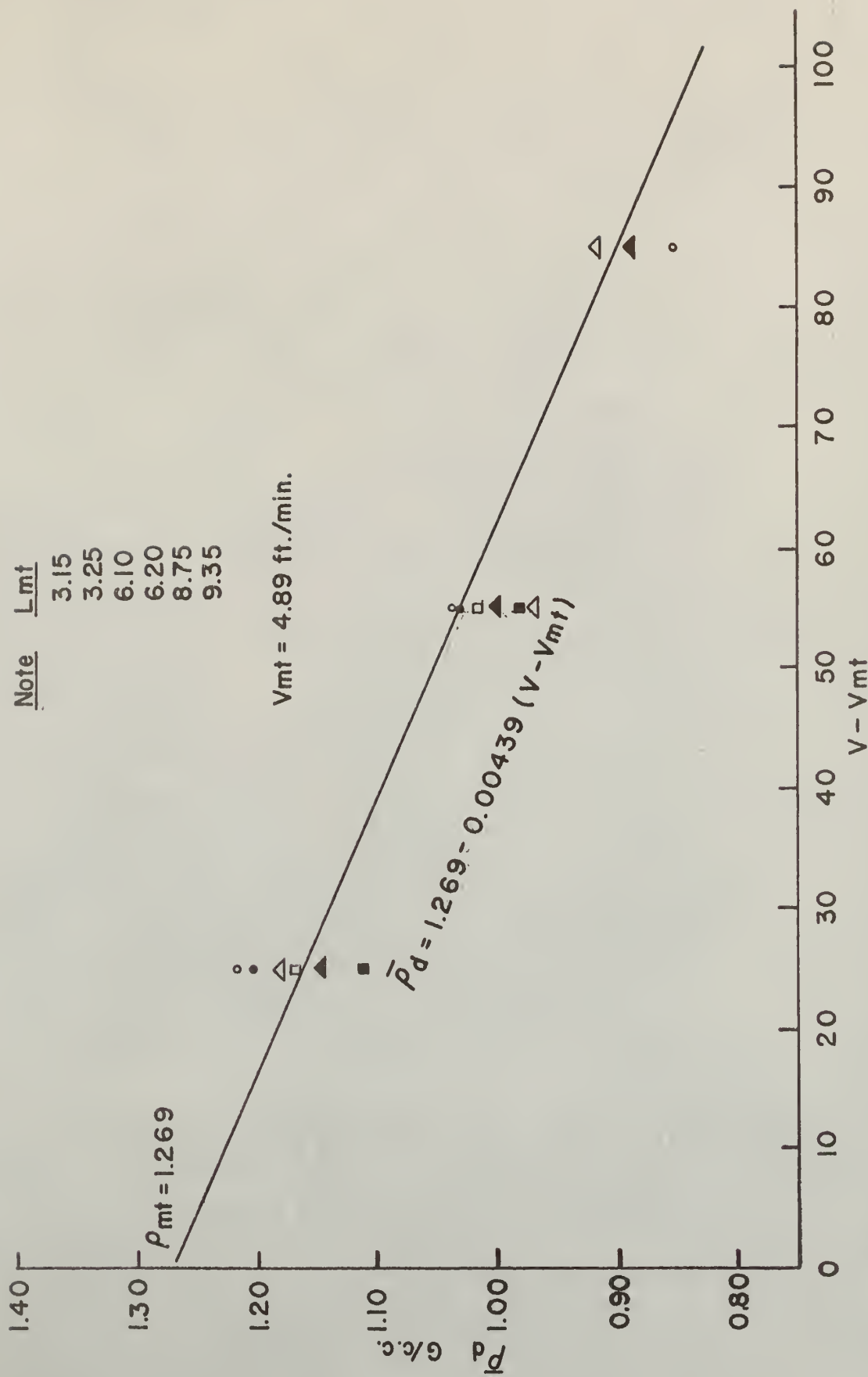
Fig. 15-(b). $\bar{\rho}_d$ Correlation for 80-100 mesh glass beads.

$\rho_{mt} = 1.269$

$\bar{\rho}_d = 1.269 - 0.00439 \, (V - V_{mt})$

$V_{mt} = 4.89$ ft./min.

| Note | $L_{mt}$ |
|------|----------|
|      | 3.15 |
|      | 3.25 |
|      | 6.10 |
|      | 6.20 |
|      | 8.75 |
|      | 9.35 |

falling density zone starts at the location corresponding to the static bed height. But for the falling density distribution obtained from the bed fluidizing at higher air velocity, the profile becomes rather skewed. We can hardly find a simple form of probability equation to fit this profile. Consequently, it is not an easy task to find a unique and general form of probability equation capable of describing the falling density profiles for all ranges of air velocity.

Thus, it becomes necessary to search for an empirical equation which, with some coefficients determined from the experimental data, will describe quantitatively the state of aggregative fluidization. For instance, the varying slope of the falling density profile could be a simple index for this purpose.

It was found that a function in the form:

$$\rho / \rho_{pa} = A_o \exp \left[ B_o \left( h/L_{mf} - 1 \right)^2 \right] \tag{18}$$

would correlate fairly well the falling density profiles. At a height corresponding to $L_{mf}$ (the position at prefluidized state) the fluidized bulk density is $\rho_d$, which can be obtained from the axial density profile. In most cases it was the same as $\overline{\rho}_d$, the average density in the constant density zone. Values of $\overline{\rho}_d$ have been plotted as function of air velocity and particle size in Fig. 15. The value of $A_o$ in equation (18) is then equal to $\rho_d/\rho_{pa}$, which can be calculated for each condition.

The problem now is to solve for $B_o$, which indicates quantitatively the slope of the correlated density profile for the falling density zone. It may be considered as an index to describe the fluidizing states under various operating conditions.

By taking logarithms of both sides of equation (18), we get the following linear equation:

$$\log\left(\rho/\rho_{pa}\right) = \log\left(\rho_d/\rho_{pa}\right) + B\left(h/L_{mf} - 1\right)^2$$

$$= A + B\left(h/L_{mf} - 1\right)^2 \tag{19}$$

It should be noted that equation (19) is only an empirical equation to fit the experimental falling density profiles. It is not fitted equally well by the experimental data obtained under different fluidizing conditions. The general trend is shown in Fig. 16.

For all sizes of glass beads fluidizing at lower air velocities, the falling density profiles were fitted better by the linear relation of equation (19); while for those fluidizing at higher air velocities, the linear relationship was not the best fit to the profile. Fig. 16 is the falling density profiles transformed into the form of equation (19). Even though the linear correlation of the dimensionless density to the dimensionless height was not as good for the runs fluidizing at higher air velocities as that at lower velocities, it is possible to obtain a best straight line by using the method of least squares. Thus the slope, B, and the intercept, $A = \log\left(\rho_d/\rho_{pa}\right)$ can be found for all sets of experimental data fluidizing at various conditions. They are listed in Table 3 (Appendix).

The index B was plotted in Fig. 17 (a), 17 (b) and 17 (c) with the air velocity variable for three different sizes of glass beads. This index converges to a single value as the air velocity increases. It indicates that at high air velocity, the particles carried up by the air bubbles are uniformly dispersed in the falling density zone. No matter what the original static bed height, the value of index B is the same if fluidizing at high air velocity.
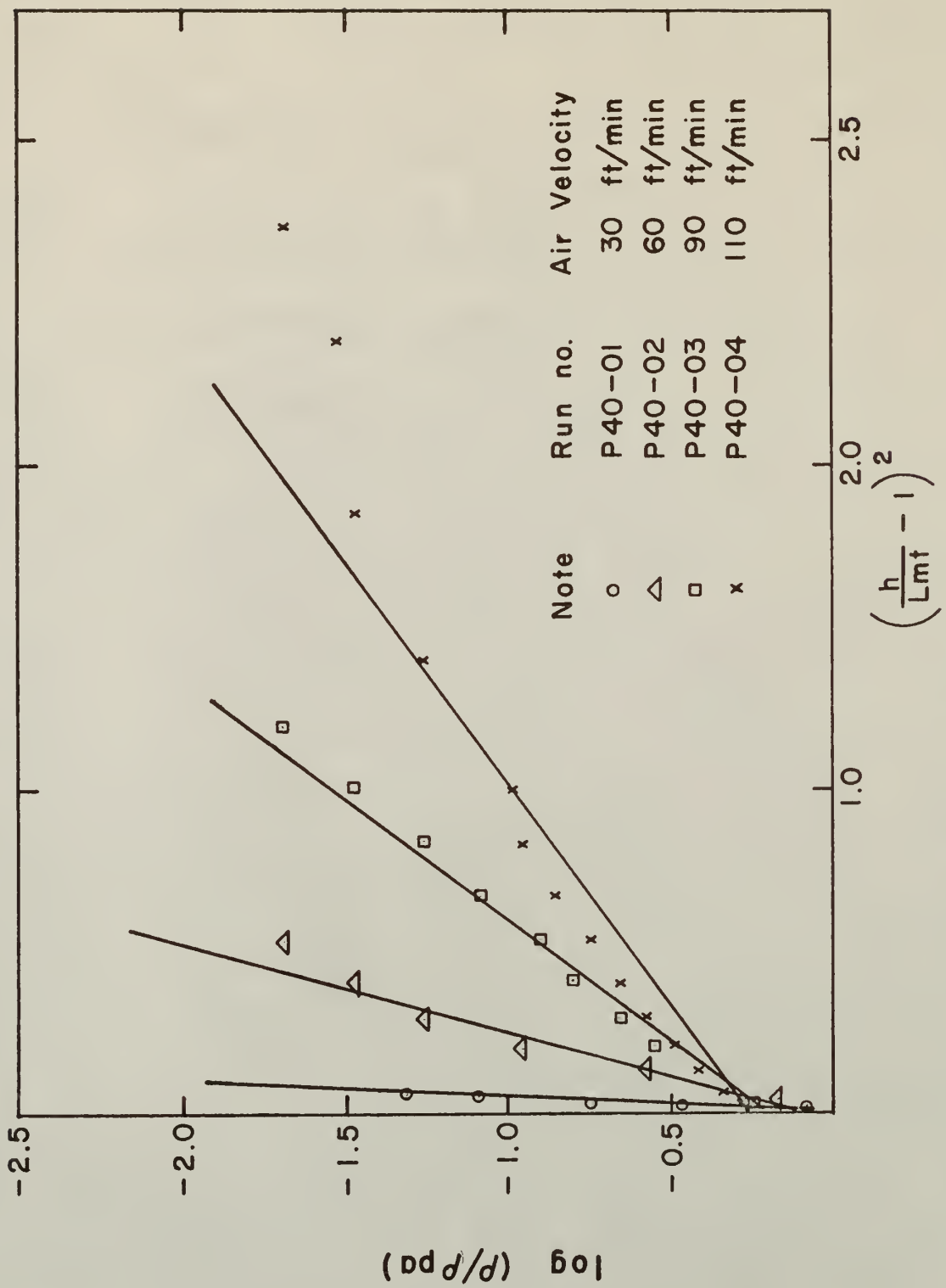
Fig. 16.   Fitting experimental data to the empirical equation
$\log (\rho/\rho_{pa}) = A + B \ (h/L_{mf}-1)^2$

Fig. 18 further verifies that the effect of the static bed height on aggregative fluidization is pronounced only at low air velocity close to the minimum velocity of fluidization.  In Fig. 19, the plot of index B vs. the particle size shows that the particle size affects the state of aggregative fluidization only at lower air velocities.  In other words, the particles are distributed in a similar manner over the falling density zone (at high air velocity), no matter what size of particles the bed is composed of.

The value of A, which is actually the ratio of fluidized bulk density at the position of the static bed height to the bulk density of the same particles in their packed state, was correlated in a similar way as that done for index B.  Fig. 20 shows that the index A is varying with air velocity for all static bed heights.  In all cases (Fig. 20, a-c) the effect of static bed height on the index A is significant when $L_{mf}/D_c < 1$.  When this ratio is greater than one, the fluidized bed expansion was essentially the same for all static bed heights fluidizing at the same air velocity.  For the 80-100 mesh glass beads, the index A correlation with air velocity converges to one curve for all static bed height, even when $L_{mf}/D_c$ is less than one.  This leads to the conclusion that when the particles size is small, the entrance effect does not affect the index A (Fig. 20, c).

The separate effect of particle size on the index A is mostly due to the relative magnitude of the bulk density of different particles in the packed state ( $\rho_{pa}$ ).  The size effect is practically the same at all air-velocity levels as has been shown in Fig. 21.

The effect of bed composition on the values of index A and index B is shown in Fig. 22.  The beds were originally at a static height of 6.5 inch and were composed of various fractions of 40-45 mesh and 80-100 mesh particles.
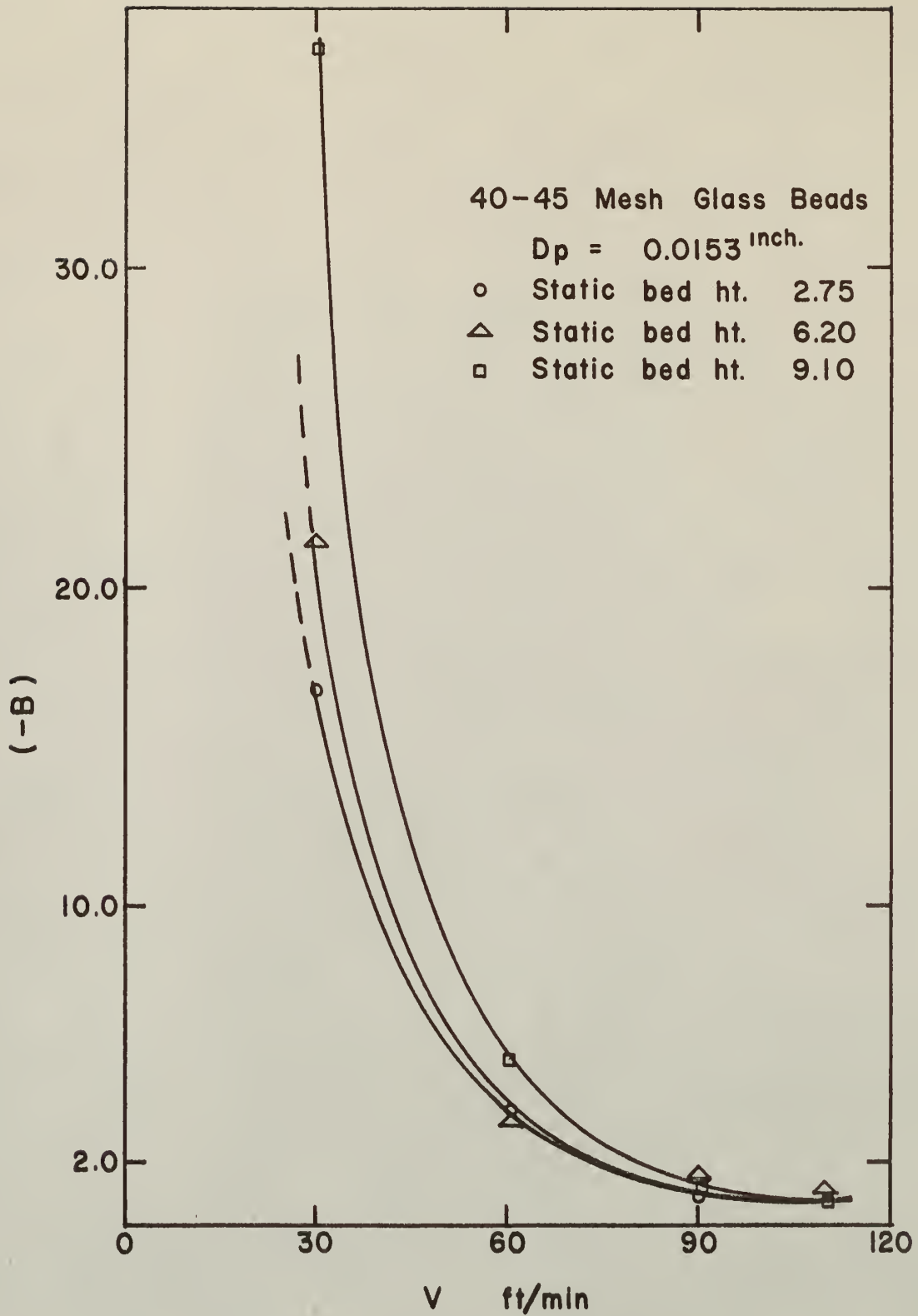
Fig. 17-a    Correlation of index-B v.s. air velocity
with static bed height as parameter.

Fig. 17-(b)  Correlation  of  Index −B  v.s.  superficial
air  velocity  with  static  bed  height  as  parameter.

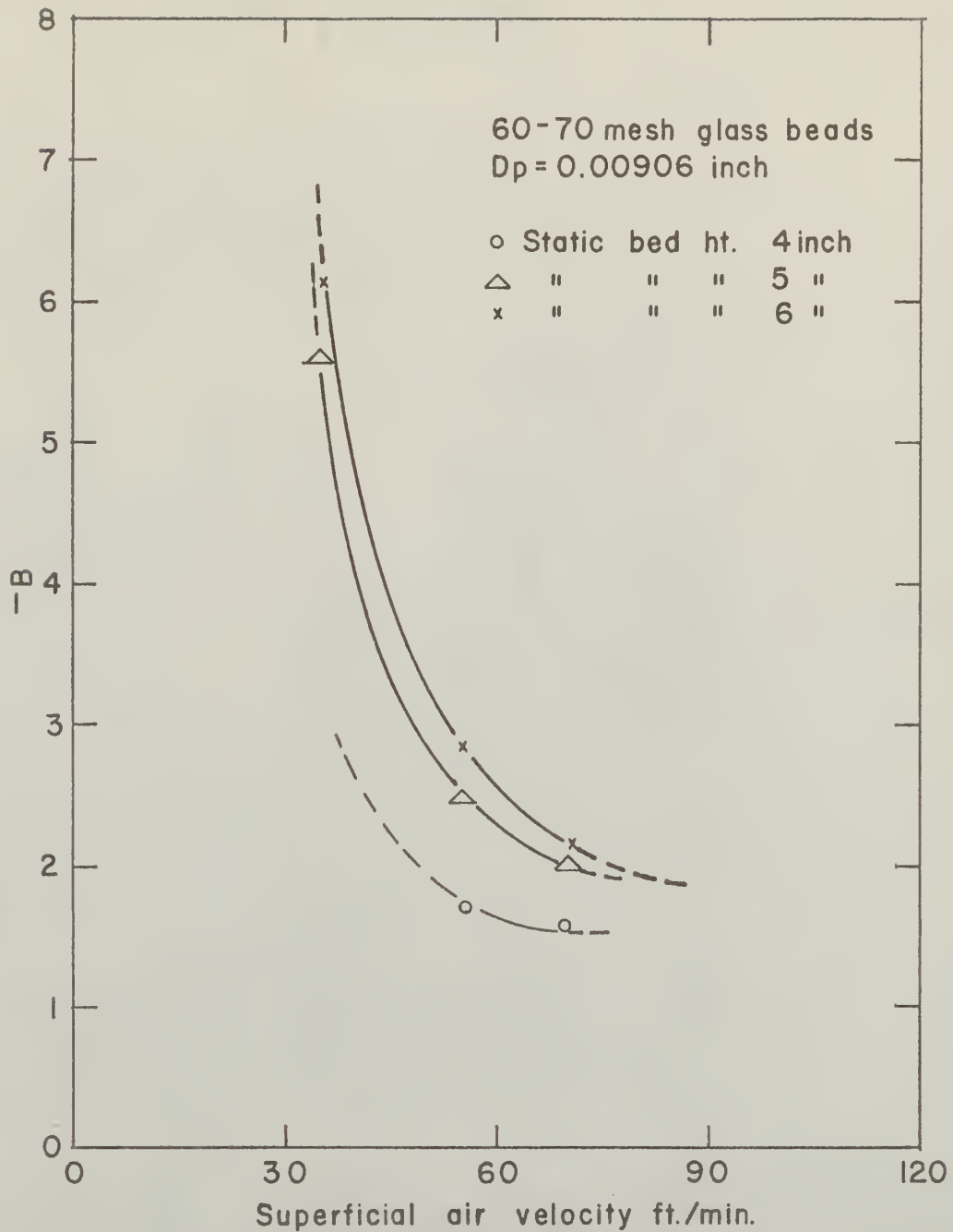Fig. 17-(c) Correlation of Index −B v.s. air velocity with static bed height as parameter.

Fig. 18. Correlation of Index -B v.s. static bed height with air velocity as parameter.

Fig. 19. Correlation of index −B v.s. Dp for same static bed height, 6.20 inch and fluidizing at three different air velocity.

Fig. 20-(a) Correlation of Index A v.s. air velocity with static bed height as parameter.

Fig. 20 - (b). Index- A v.s. air velocity with static bed as parameter.

Fig. 20-(c) Correlation of Index-A v.s. air velocity with static bed height as parameter.

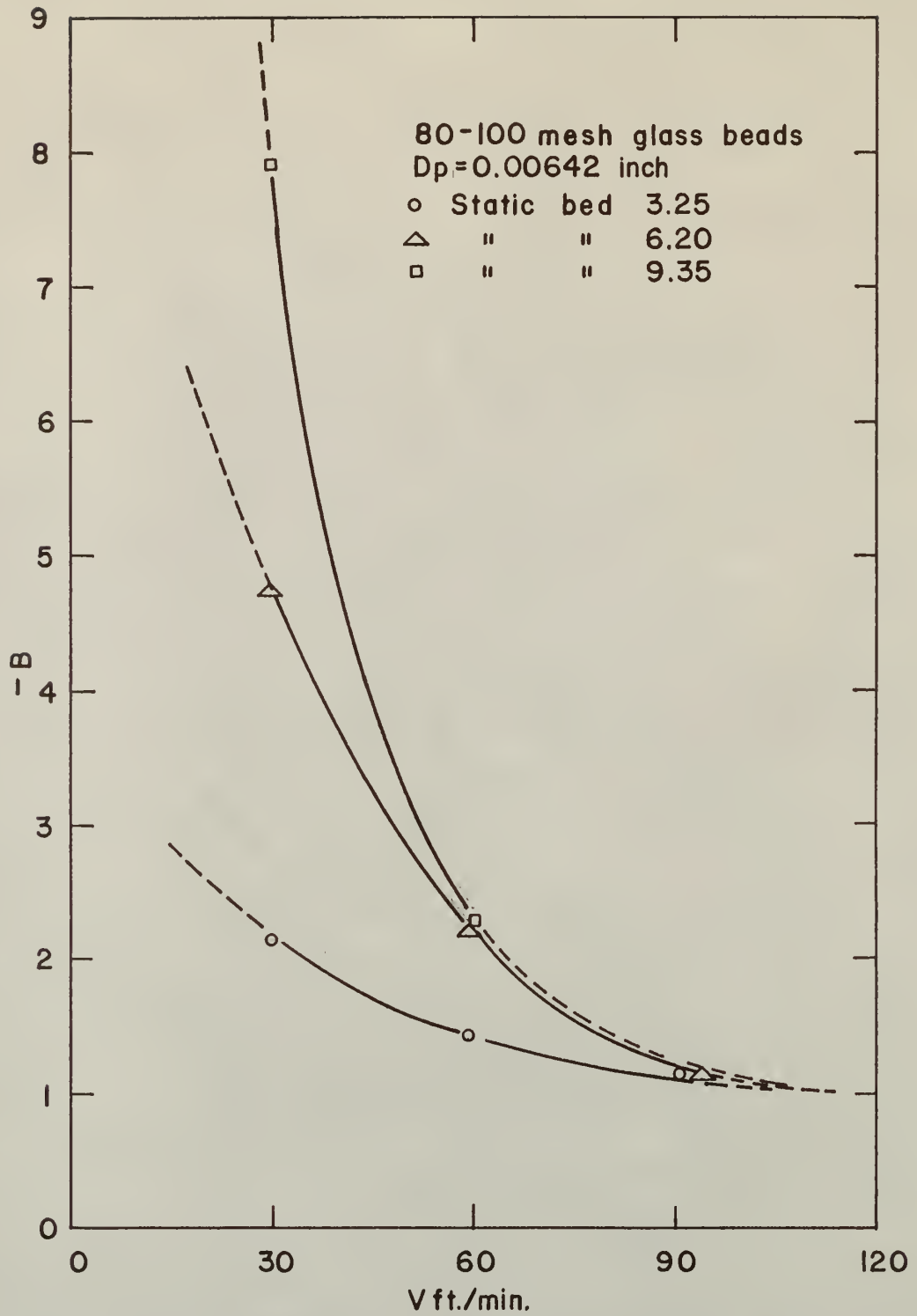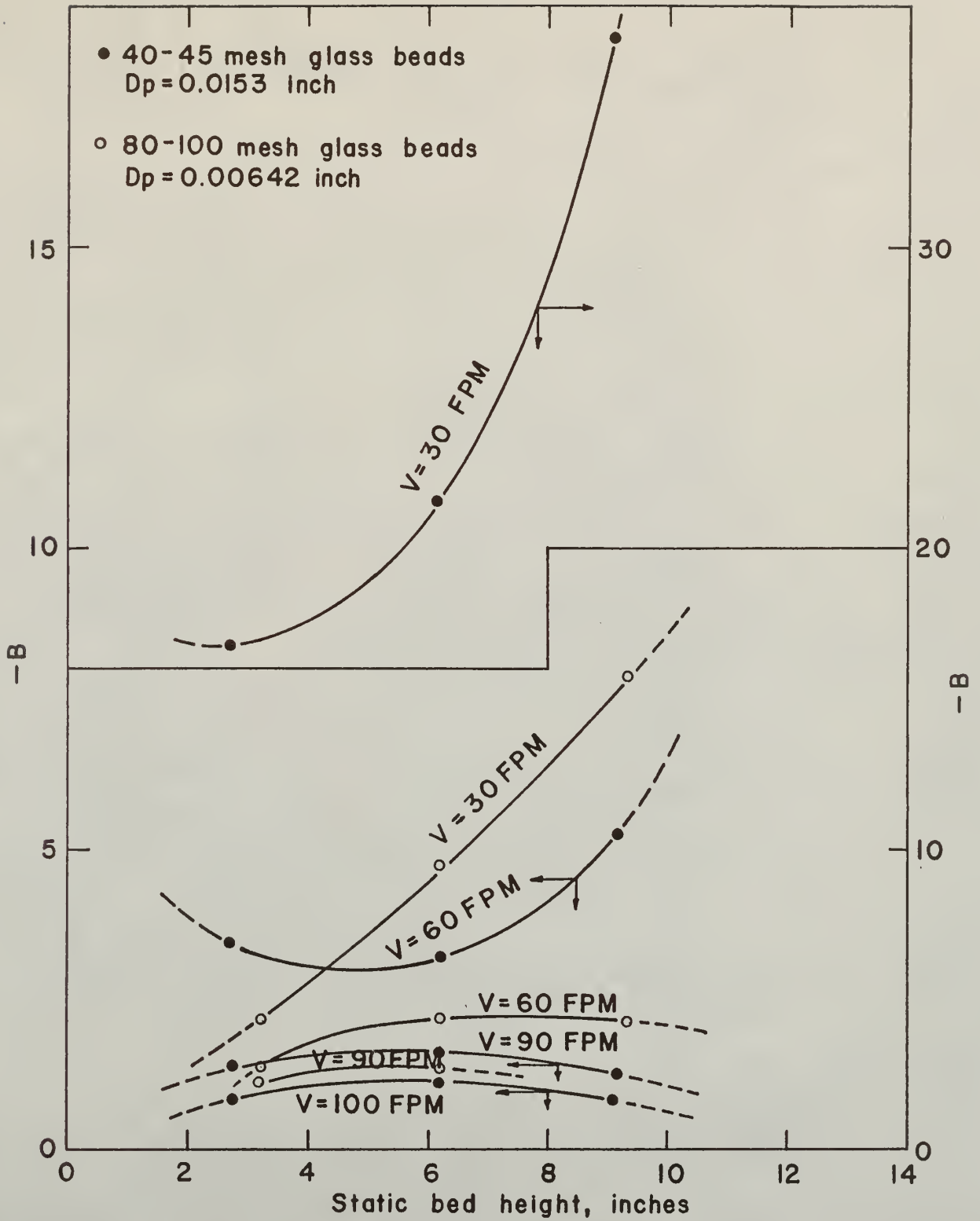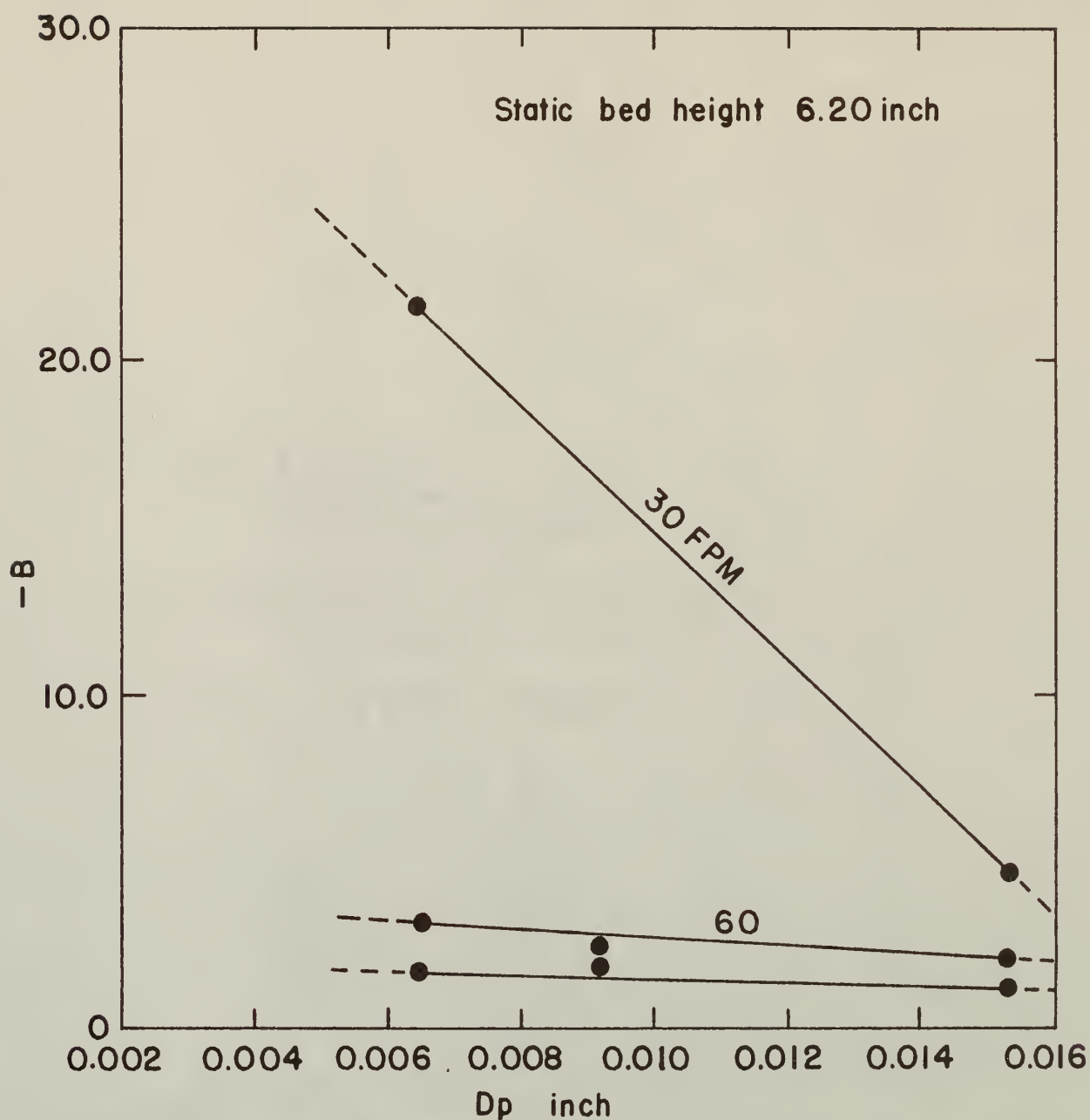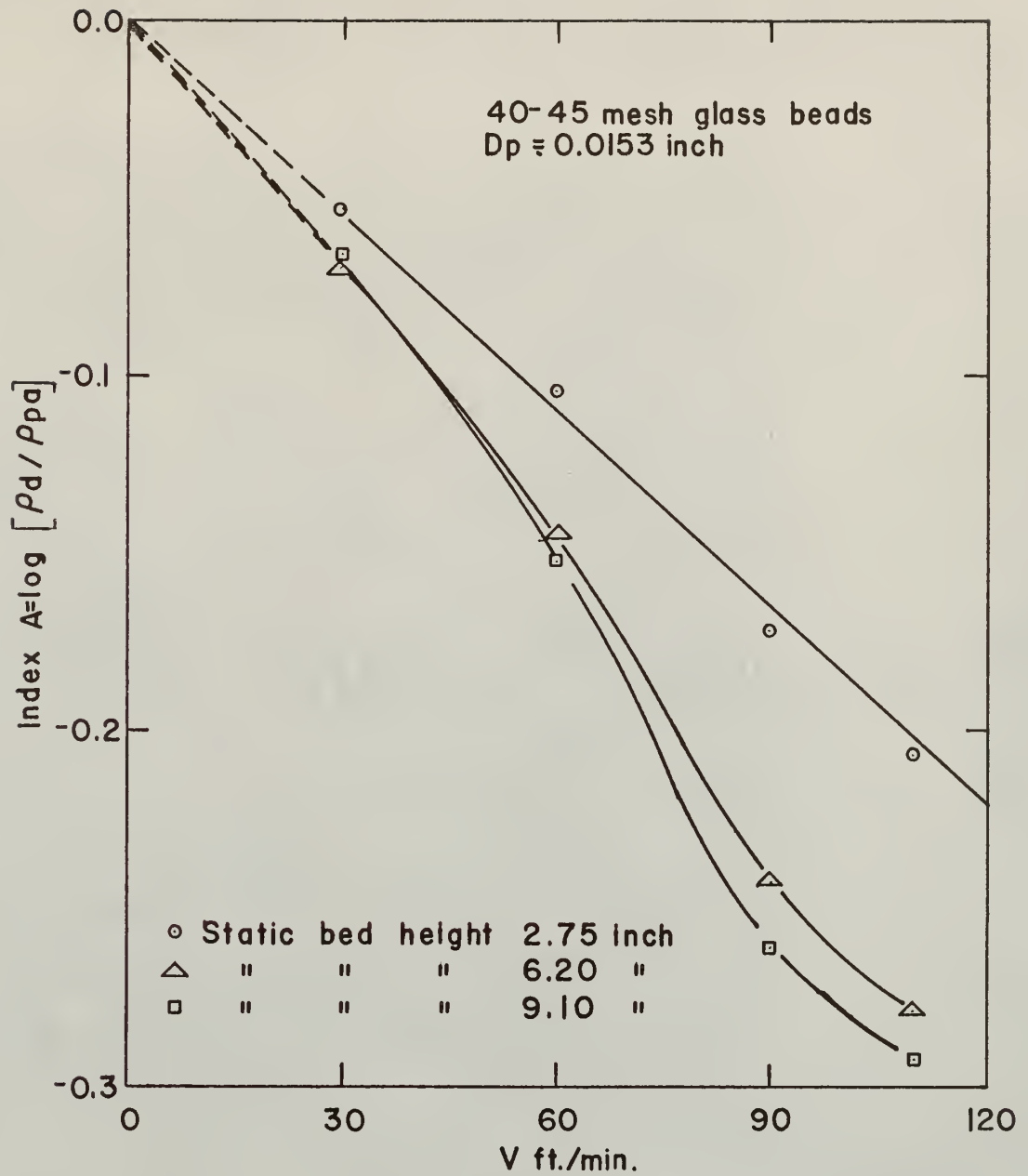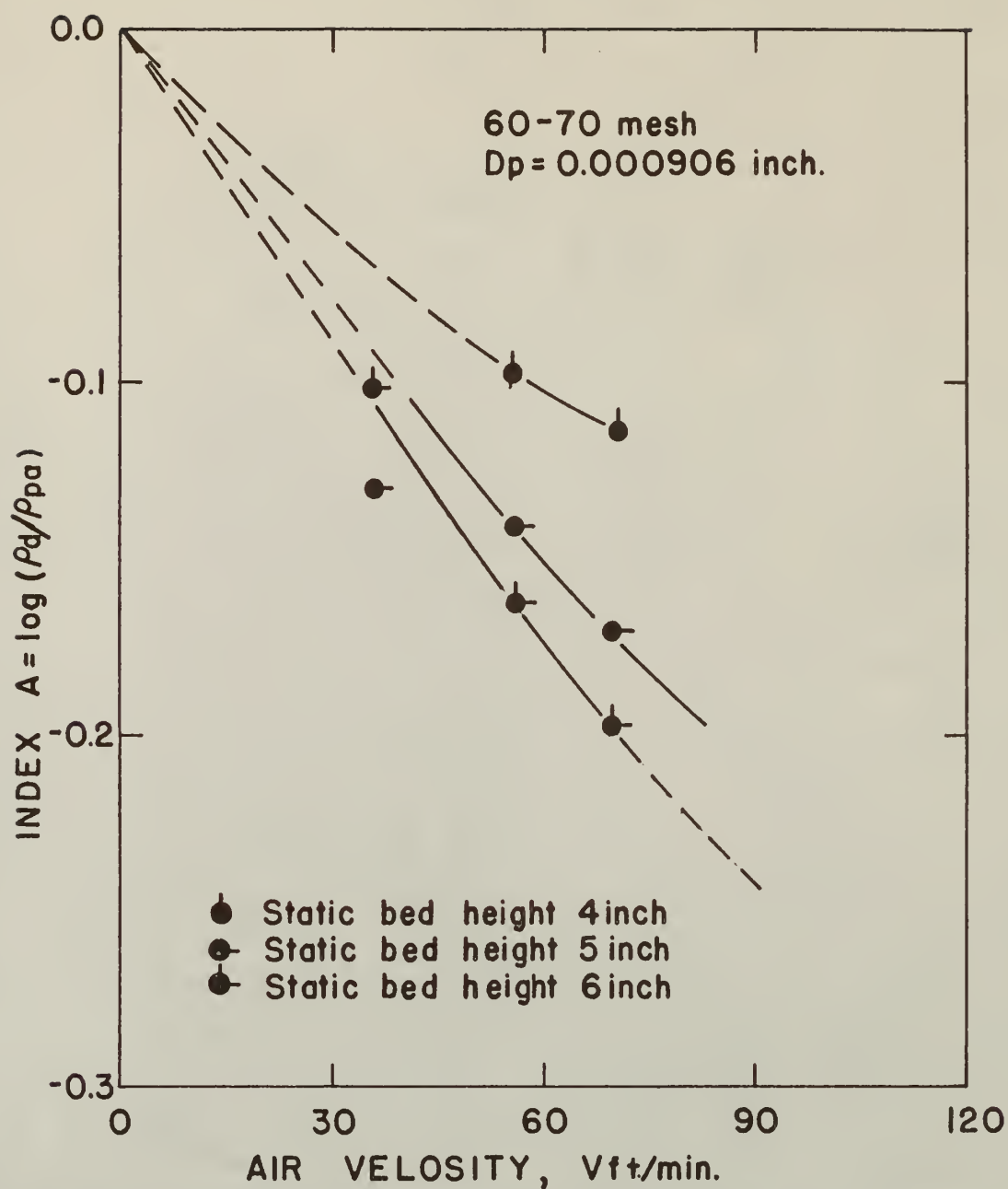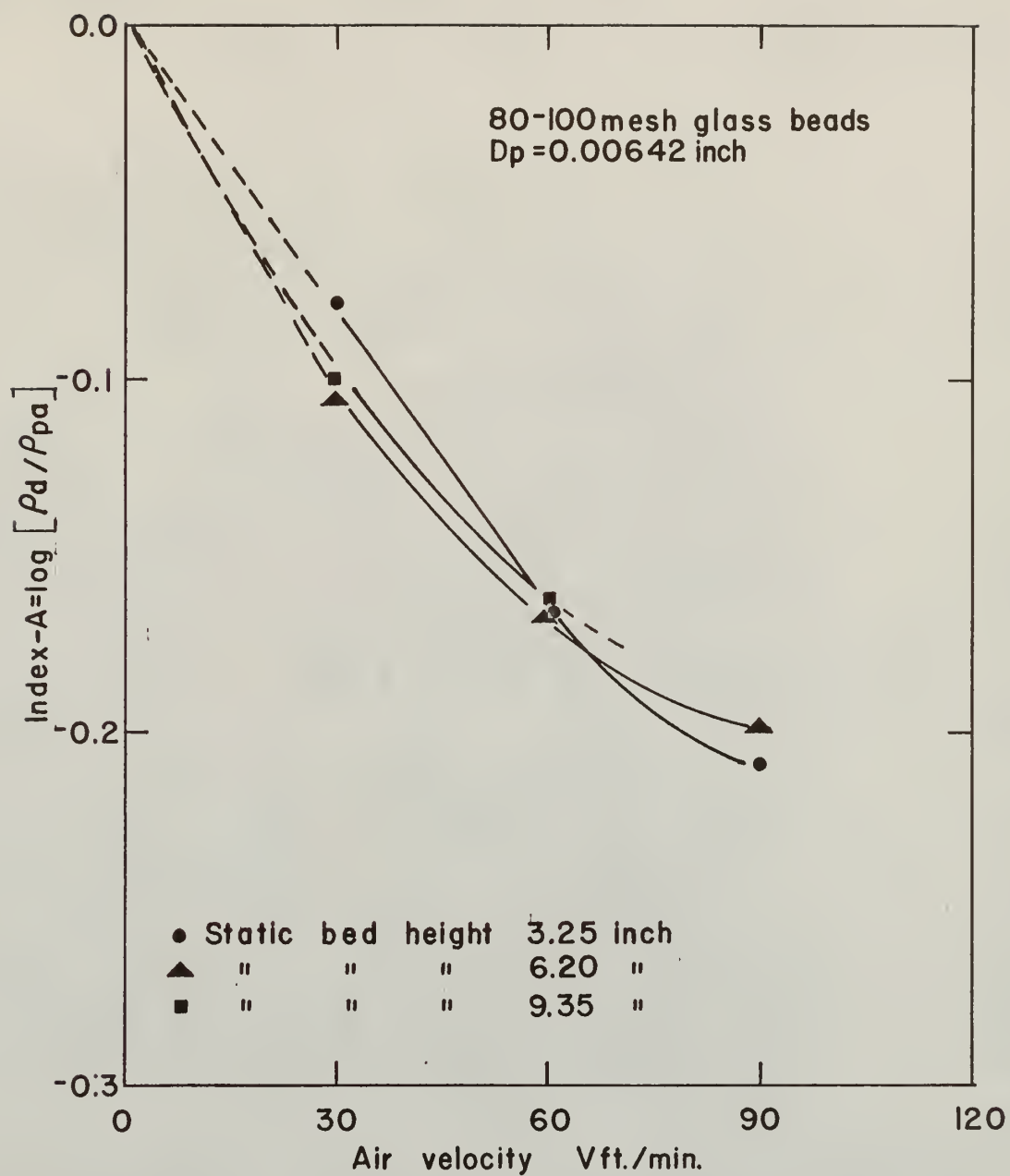They were fluidized at an air velocity of 60 ft/min. The axial density pro-
files were obtained and index A and index B calculated for every bed composi-
tion. Bed compositions of 0, 2, 5, 10, 50, 90, 95, 98 and 100 percent by
weight of 40-45 mesh glass beads were used. The results show that the mixed
particle size affects index A and index B significantly only when the composi-
tion is below 10% or above 90% by weight of 40-45 mesh glass beads.

As the state of aggregative fluidized beds is affected by the three major
variables, i.e., superficial fluid velocity, particle size and the ratio of
static bed height to the diameter of column; index B as well as index A
(which is used to describe the state of aggregative fluidization) should be
correlated in a single empirical equation. By applying the Pi-theorem in
the dimensional analysis, we obtain:

$$|A| = \alpha' \left( \frac{VD_p \rho_F}{\mu} \right)^a (D_p/D_c)^b (L_{mf}/D_c)^c \tag{20}$$

$$|B| = \beta' \left( \frac{VD_p \rho_F}{\mu} \right)^{a'} (D_p/D_c)^{b'} (L_{mf}/D_c)^{c'} \tag{21}$$

where, the values of $\alpha'$, a, b, c; $\beta'$, a', b' and c' can be obtained from
the experimental data.

The equations for the series of data obtained are:

$$|A| = 1.396 \times 10^{-5} \left( \frac{D_p V \rho_F}{\mu} \right)^{0.978} (D_p/D_c)^{-1.265} (L_{mf}/D_c)^{0.3469} \tag{22}$$

$$|B| = 5.492 \times 10^{9} \left( \frac{D_p V \rho_F}{\mu} \right)^{-2.094} (D_p/D_c)^{3.045} (L_{mf}/D_c)^{0.3474} \tag{23}$$

Equations (22) and (23) are plotted in Fig. 23 and Fig. 24 in order to
compare the calculated values for $|B|$ and $|A|$ with those experimentally
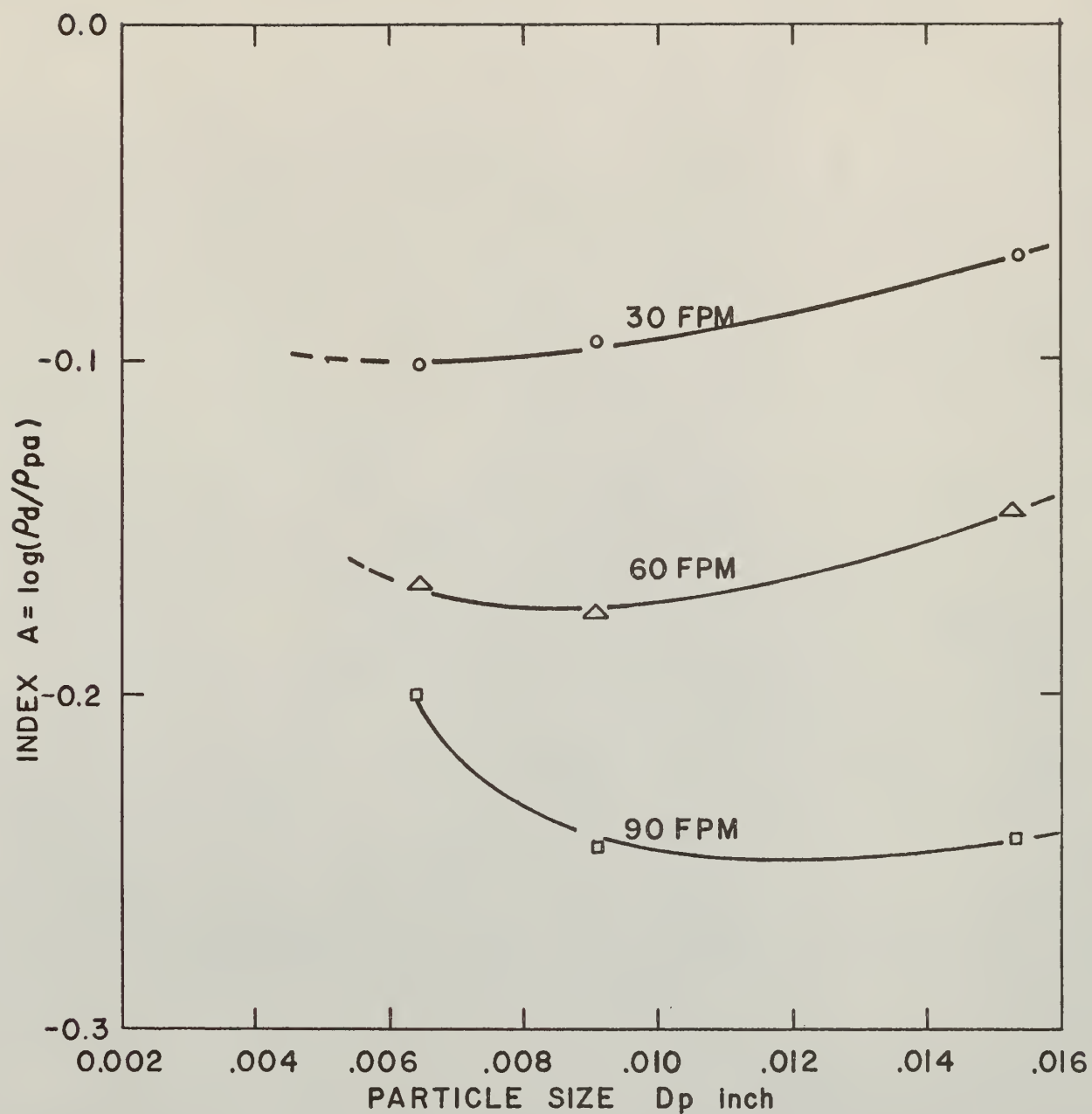determined (Table 4 and Table 5).

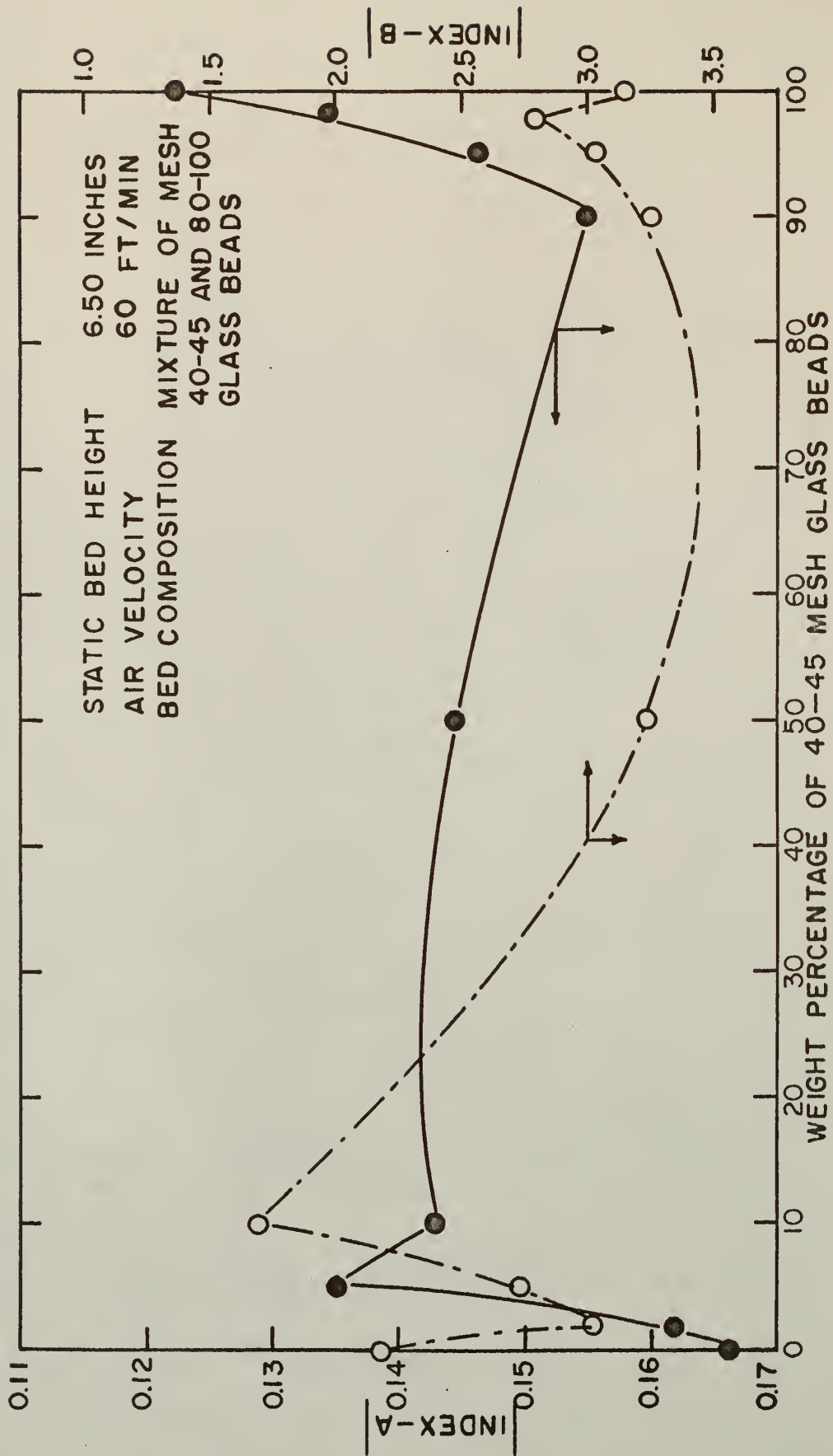Fig. 21. Index-A v.s. Dp for static bed height = 6.20 inch fluidizing at various velocity.

Fig. 22. Effect of bed composition on indices A and B.

Table 4. Comparison of calculated |B| with the experimental data.

| 40-45 mesh glass beads | | 80-100 mesh glass beads | |
|---|---|---|---|
| Experimental | Calculated | Experimental | Calculated |
| 16.789 | 12.524 | 25.695 | 18.910 |
| 3.438 | 2.932 | 2.925 | 4.382 |
| 1.391 | 1.264 | 1.572 | 1.391 |
| 0.813 | 0.830 | 1.710 | 2.231 |
| 21.471 | 16.009 | 5.602 | 6.298 |
| 3.151 | 3.778 | 2.450 | 2.496 |
| 1.645 | 1.635 | 2.035 | 1.560 |
| 1.133 | 1.074 | 6.192 | 6.660 |
| 36.984 | 18.548 | 60-70 mesh glass beads | |
| 5.204 | 4.358 | 2.850 | 2.637 |
| 1.213 | 1.864 | 2.142 | 1.651 |
| 0.815 | 1.253 | 2.141 | 5.929 |
| 10.395 | 13.280 | 1.406 | 1.388 |
| 3.328 | 3.102 | 1.135 | 0.594 |
| 1.033 | 1.264 | 4.766 | 7.642 |
| 24.010 | 17.444 | 2.185 | 1.762 |
| 3.151 | 4.051 | 1.238 | 0.762 |
| 1.150 | 1.710 | | |

Table 5. Comparison of calculated | A | with the experimental data.

| 40-45 mesh glass beads | | 80-100 mesh glass beads | |
|---|---|---|---|
| Experimental | Calculated | Experimental | Calculated |
| 0.0535 | 0.0523 | 0.0793 | 0.0704 |
| 0.1052 | 0.1030 | 0.1667 | 0.1386 |
| 0.1722 | 0.1526 | 0.2074 | 0.2061 |
| 0.2072 | 0.1857 | 0.1055 | 0.0868 |
| 0.0691 | 0.0705 | 0.1663 | 0.1723 |
| 0.1452 | 0.1384 | 0.1993 | 0.2548 |
| 0.2423 | 0.2047 | 0.0983 | 0.1010 |
| 0.2789 | 0.2491 | 0.1624 | 0.1990 |
| 0.0677 | 0.0800 | | |
| 0.1525 | 0.1574 | 60-70 mesh glass beads | |
| 0.2617 | 0.2341 | 0.1142 | 0.1625 |
| 0.2912 | 0.2818 | 0.0991 | 0.1304 |
| 0.0463 | 0.0554 | 0.1318 | 0.0899 |
| 0.0825 | 0.1092 | 0.1420 | 0.1386 |
| 0.1575 | 0.1661 | 0.1716 | 0.1726 |
| 0.0689 | 0.0702 | 0.1029 | 0.0961 |
| 0.1223 | 0.1388 | 0.1629 | 0.1482 |
| 0.2151 | 0.2072 | 0.1987 | 0.1844 |
| 0.0802 | 0.0806 | | |
| 0.1744 | 0.1596 | | |

Fig. 23. Dimensionless correlation for Index A.
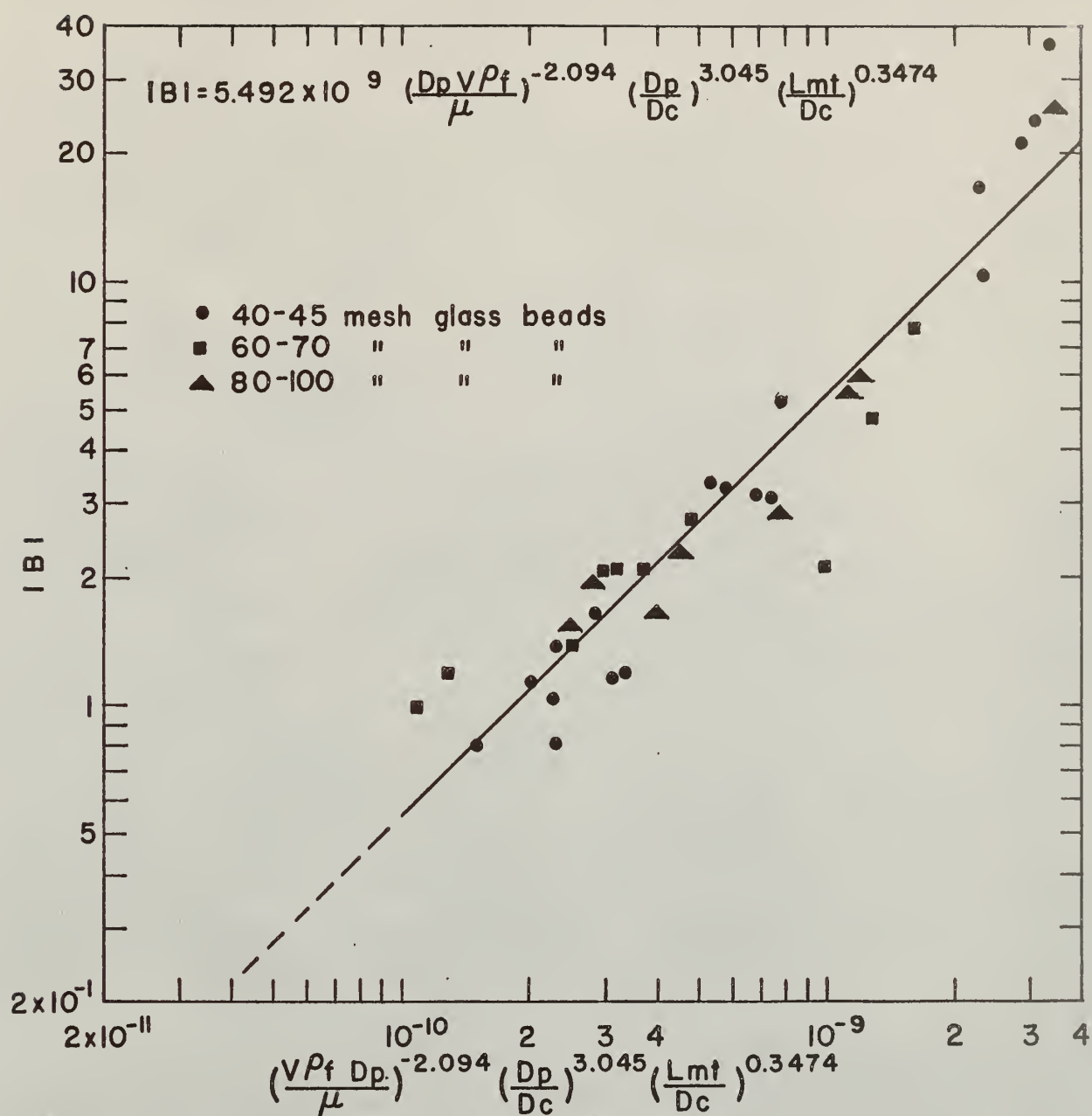
Fig. 24.  Dimensionless  correlation  for  Index B.

We can now calculate a complete axial density profile for the air-particle fluidizing system with Fig. 15 and equations for $|A|$ and $|B|$. It is illustrated in the following illustration:

Illustration:

In a fluidization test, glass beads of 40-45 mesh were used (Run. P40-06), experiment was run at room temperature and with air at 1 atmospheric pressure in a circular column of 4 inch diameter. The bed had a height of 6.20 inch at incipient fluidization. Estimate the fluidized bulk density profile, for the bed fluidizing at 1 ft/sec. of superficial air velocity. Compare it with the experimental data.

Solution:

Properties of air at the fluidizing condition:

$$\rho_F = 0.0757 \text{ lb/cu-ft}$$
$$\mu = 1.23 \times 10^{-5} \text{ lb/ft-sec.} \tag{11}$$

The air velocity at incipient fluidization can be calculated:

$$V_{mf} = 22.35 \text{ ft/min.}$$

Properties of particles:

$$D_p = 0.0153 \text{ inch}$$
$$\rho_{pa} = 1.502 \text{ gm/cu-cm}$$

Constant density zone:

$$V = 1 \text{ ft/sec.} = 60 \text{ ft/min.}$$

$$V - V_{mf} = 37.65 \text{ ft/min.}$$

from Fig. 15 (a), $\overline{\rho}_d = 1.168$ gm/cu-cm.

Falling density zone:

$$N_{Re} = \frac{V \rho_F D_p}{\mu} = \frac{(1)(0.0757)(0.0153)}{(1.23 \times 10^{-5})(12)} = 7.85$$

$$(N_{Re})^{0.978} (\frac{D_p}{D_c})^{-1.265} (\frac{L_{mf}}{D_c})^{0.3469} = (7.85)^{0.978} (\frac{0.0153}{4})^{-1.265} (\frac{6.20}{4})^{0.3469}$$

$$= (7.49)(1.120)(1.164) = 9.763 \times 10^3$$

From Fig. 23,

$$|A| = 0.139$$

$$A = \log (P_d / \rho_{pa}) = -0.139$$

$$(N_{Re})^{-2.094} (\frac{D_p}{D_c})^{3.045} (\frac{L_{mf}}{D_c})^{0.3474} = (7.85)^{-2.094} (\frac{0.0153}{4})^{3.045} (\frac{6.20}{4})^{0.3474}$$

$$= (1.34 \times 10^{-2})(4.335 \times 10^{-8})(1.167)$$

$$= 6.765 \times 10^{-10}$$

From Fig. 24,

$$|B| = 3.65 \qquad\qquad B = -3.65$$

Thus, the density in the falling density zone can be calculated by the following equation:

$$\log (\rho / \rho_{pa}) = A + B (h/L_{mf} - 1)^2$$

i.e.,

$$\log (\rho / 1.502) = -0.139 - 3.65 (h/6.2 - 1)^2$$

The calculated density and the experimental values for the falling density zone are listed as follows:

| Height from distributor h, in | Experimental | | Calculated | |
|---|---|---|---|---|
| | $\rho / \rho_{pa}$ | gm/cu-cm | $\rho / \rho_{pa}$ | gm/cu-cm |
| 7.00 | 0.614 | 0.922 | 0.633 | 0.951 |
| 8.00 | 0.344 | 0.516 | 0.358 | 0.538 |
| 9.00 | 0.153 | 0.229 | 0.132 | 0.200 |
| 10.00 | 0.039 | 0.058 | 0.031 | 0.047 |
| 11.00 | 0.020 | 0.030 | 0.005 | 0.007 |

The experimental data are plotted in Fig. 25 with the density profile calculated by the obtained equation.
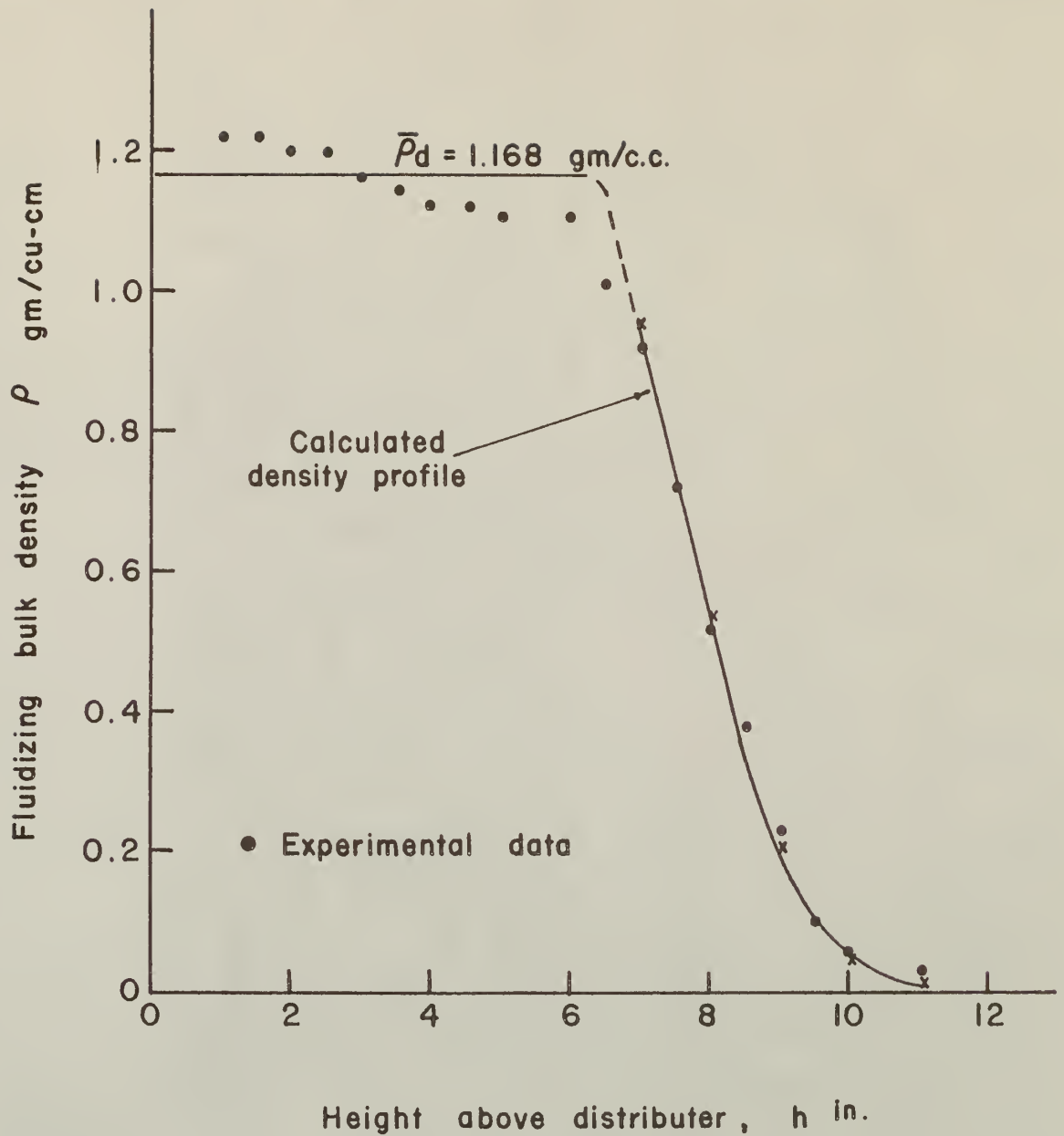
Fig. 25.  Comparison of experimental data with calculated density profile for the illustration

Determination of the Fluidized Bed Height

The behavior of gas-solid fluidized beds observed in this work deviated considerably from the behavior of an ideal expansion of a packed bed. The particles were not as uniformly suspended in the bed as is usually observed in most of the liquid fluidized beds. Even the two phase model for gas-solid fluidization is only a very approximate one. Actually, there is no distinct phase which can be defined as a bubble phase consisting of purely gases, nor is there a dense phase consisting of uniform emulsion of particles. The bubbles, formed by the gas and held in the pore spaces between solids, grow in size as they rise from gas distributor toward the top of the bed, and finally burst near the position corresponding to the static bed height. The small size particles suspended in the air stream were fluctuating and weaving at the top of the bed, and so the disperse phenomenon dominated the top layer of the bed. Thus, there is no clear height of the fluidized bed that can be measured visually.

Three methods can be used to measure the fluidized bed height from the solid density profile under measurement.

(a). End point of the density profile:

Tracing the density profile in the falling density zone and extrapolating to the position at which the density diminishes to zero, we can define the fluidized bed height at this point. This height should correspond to the maximum height of the fluidized bed as observed visually by previous investigators.

(b). Cross point of the normalized density profile:

As indicated in the dimensionless density profiles, Figure 13, the significant height of aggregative fluidized beds can be defined at the point where

the ideally expanded density profile crosses the actually developed density profile of the fluidized bed. The particles are assumed to be uniformly distributed below this height, and the portion above it is less significant to the over-all performance of the total bed and is, therefore, considered to be negligible. This height, as defined, should signify the bed, though aggregative, as a particulate one.

(c). Height determined by IIS methods:

The fluidized bed height - defined as the breaking point of the axial IIS distribution curve - was proposed by Steward (25). However this height corresponds closely to the height determined by method (b).

It is expected that the bed defined by method (b) or method (c) would give better correlation than by method (a), if the analogous correlation of a particulate fluidized bed is applied in an aggregative fluidized bed. In the calculation for reactor conversion, the bed height defined in (b) and (c) should give a more realistic picture, since the insignificant part of the disperse phase is neglected in this consideration.

The fractional fluidized bed expansion $(L - L_{mf})/L_{mf}$, calculated from the height as determined by method (a) was plotted as a function of superficial air velocity with $L_{mf}/D_c$ as parameters in Fig. 26. This correlation shows a linear relationship, which is consistent with the data presented by Minet et.al.for chars (17). The effect of the static bed height on the expansion of fluidized beds is also shown in this figure. Similar correlation was attempted with the bed height defined by method (b) or method (c). The result shows that it deviates considerably from the linear relationship (Fig. 27). Fig. 28 is a comparison between the fluidized bed height determined by method (a) and method (c). It indicates that for a certain value of $L_{mf}/D_c$ and particle

size, these two defined heights are different from each other by a propor-
tionality factor.

## Pressure Gradient Correlations

The pressure-drop-flow diagram in a fluidizing system is well explained in
the following paragraph (6):

> If the behavior of packed bed is followed when a gas stream
> is introduced from the bottom, the pressure drop at first increases
> with flow rate without bed expansion.  When the flow rate is
> sufficient to cause a pressure gradient equal to the buoyant
> weight of the solids per unit volume, further increase in the
> flow rate causes the bed to expand -- i.e. increase the fractional
> void volume -- the pressure drop remains substantially constant....

The two pressure-drop-flow diagrams obtained are shown in Figs. 28-a. and
28-b.  They resemble in shape to the pressure-drop-flow diagram for ideally
fluidizing systems (11), i.e., the pressure drop becomes essentially just the
weight of the bed at the air velocity just beyond the minimum velocity of
fluidization.  This probably indicates that the fluidizing bed developed with
the air distributor (canvas filter cloth) was macroscopically almost equivalent
to the ideal expansion of a packed bed, since the size of air bubbles formed
was small and the bubbles were nicely distributed in the bed at the air
velocity around the minimum velocity of fluidization.  This also implies that
the tube-bundle theory (4) developed for the study of the pressure drop
through a packed bed may be applied analogously to the analysis of the
pressure gradient in the present fluidizing systems, provided the fluidized
bed height can be correctly determined.

As mentioned previously, when the air velocity reaches the minimum velocity
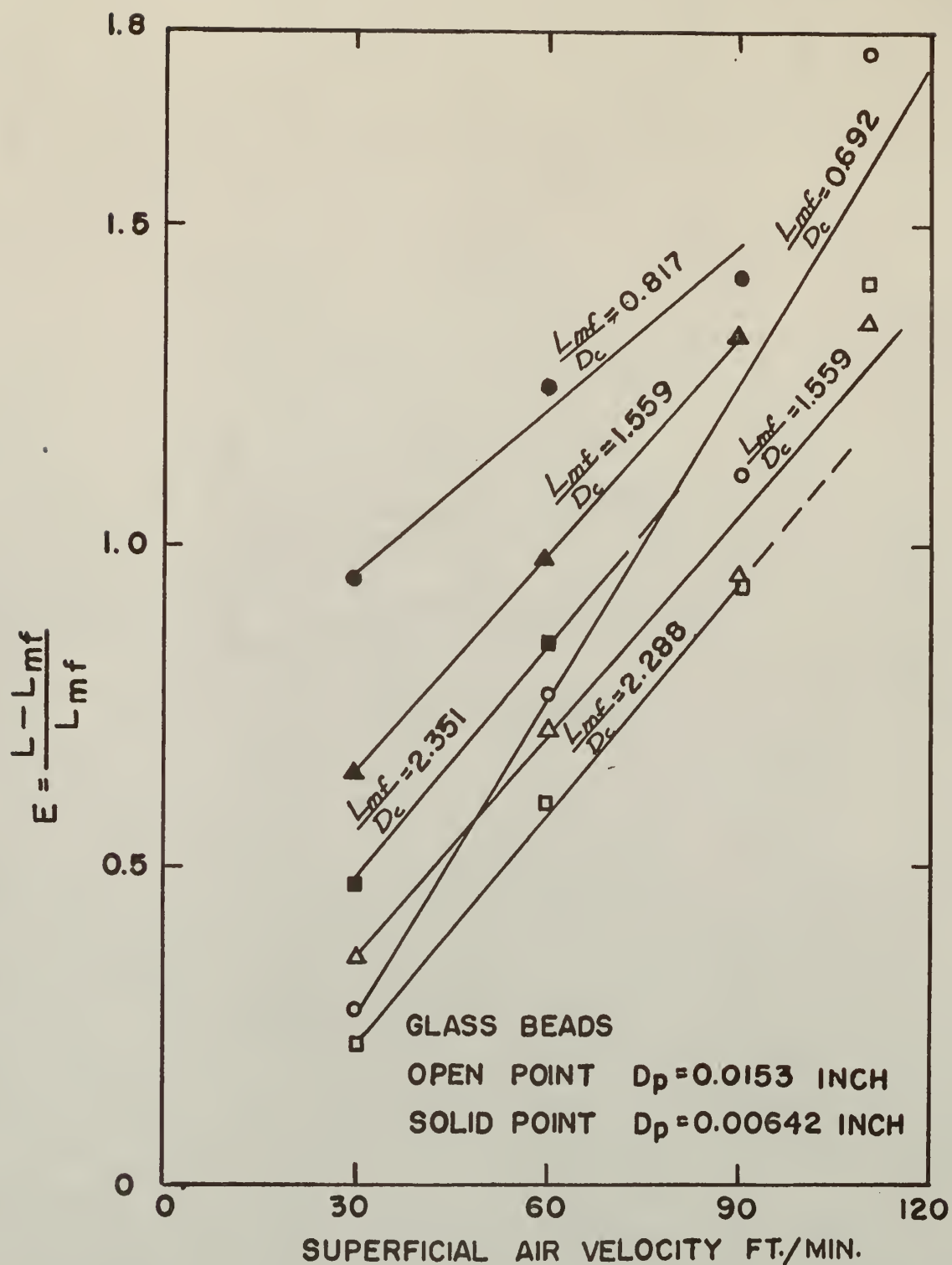of fluidization, the pressure drop, $\Delta P$ is constant and substantially equal

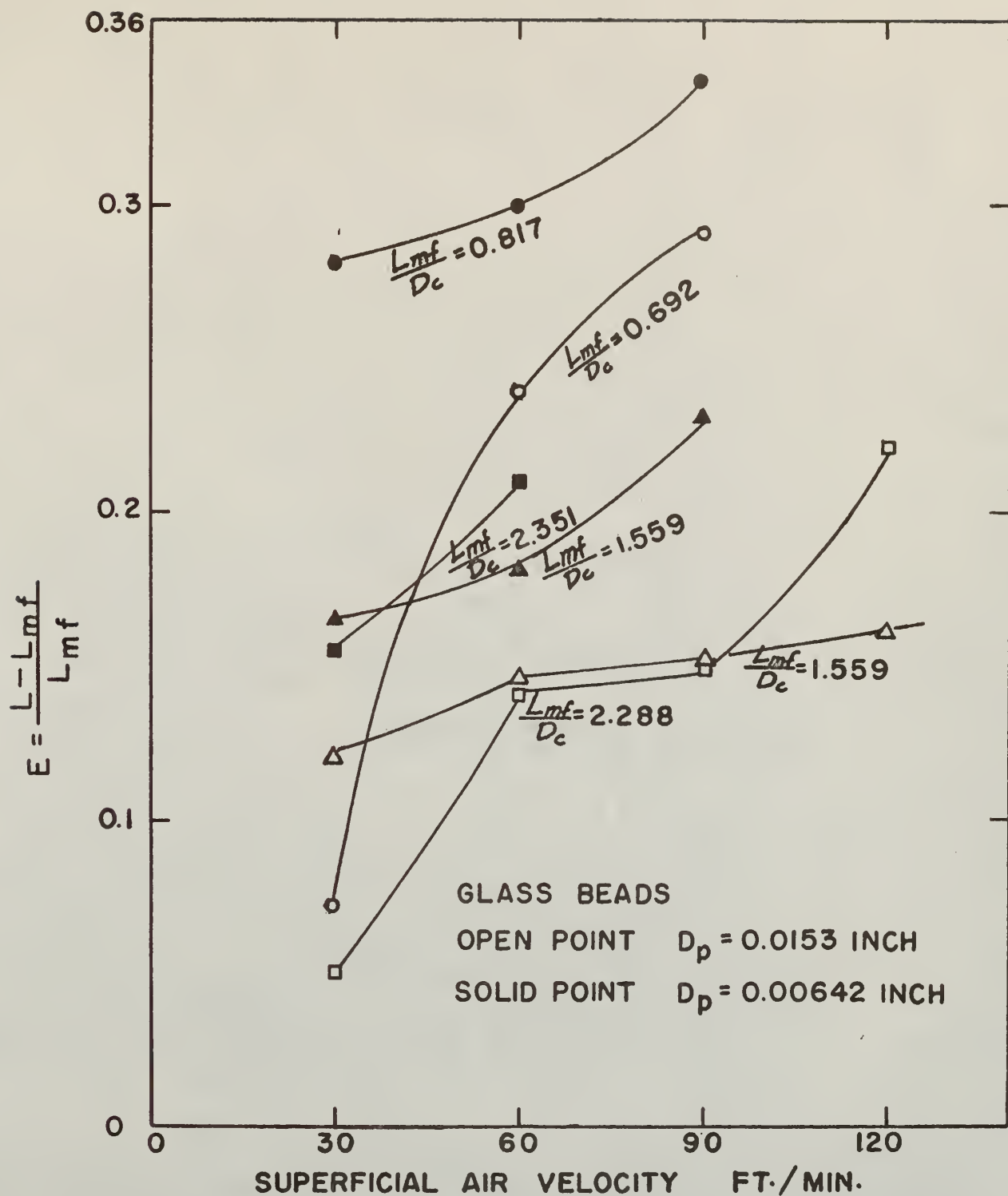Fig. 26. The fractional fluidized bed expansion from height determined by method (a).

Fig. 27. The fractional fluidized bed expansion from height determined by method (b)

Fig. 28. Comparison of fluidized bed height defined by method (a) and method (b).
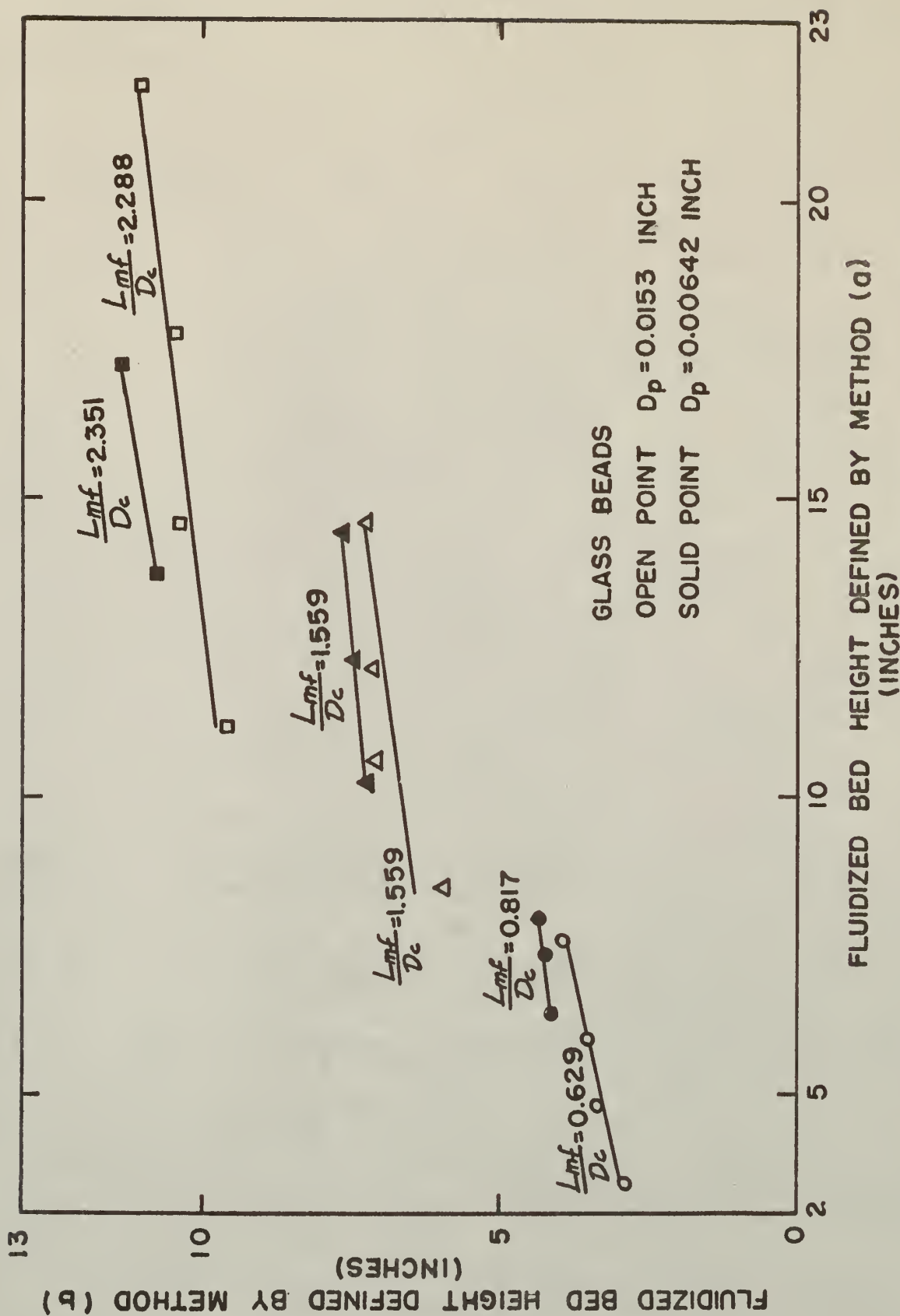
to the weight of the particles constituting the bed. But the pressure gradient
is varied with increased air velocity, since the air flow beyond the minimum
fluidizing velocity causes the bed to expand. Thus, the pressure gradient
$\triangle P/L$ decreases with the increase in the air velocity.

In Fig. 29, the pressure gradients, $\triangle P/L$, are correlated in a form of
friction factor, $f_k$, originally proposed (6) for correlating the pressure drops
through packed beds, against the modified Reynolds number, $N_{Re}' = \frac{D_p V \rho_F}{\mu} \cdot \frac{1}{1 - \epsilon}$.
But, the numerical values of the pressure gradient, $\triangle P/L$, for fluidized beds
should depend on the definition of fluidizing bed heights used. (See previous
section.) The correlation obtained with the height determined by method (a)
yields the curves resembling the Ergun equation for packed bed in shape (4),
and have varying slopes. Whereas, the correlation with that determined by
method (b), like Blake-Kozeney equation, has a constant slope. In both
cases the observation of Fig. 29 and the data shows that the effect of particle
size, $D_p$, appears to be more significant than that suggested by the correlations
proposed for packed beds. The experimental data indicate that the static bed
height also has some effect on the correlation of pressure gradients. But,
this factor does not come into the consideration for packed beds.

The results of the dimensionless analysis lead to the following form
(Appendix II):

$$f_K = \frac{g_c \triangle P}{L} \cdot \frac{\epsilon^3}{1 - \epsilon} \cdot \frac{D_p}{P_F V^2} = \phi \left( \frac{D_p \rho_F V}{\mu} \cdot \frac{1}{1 - \epsilon} \right)^a \left( \frac{D_p}{D_c} \right)^b \left( \frac{L_{mf}}{D_c} \right)^c \quad (24)$$

Where, the constant $\phi$, a, b, c, can be evaluated from the experimental data
with the height of fluidized bed defined by methods (a) and (b).

With the height defined by method (a), the dimensional analysis gives:
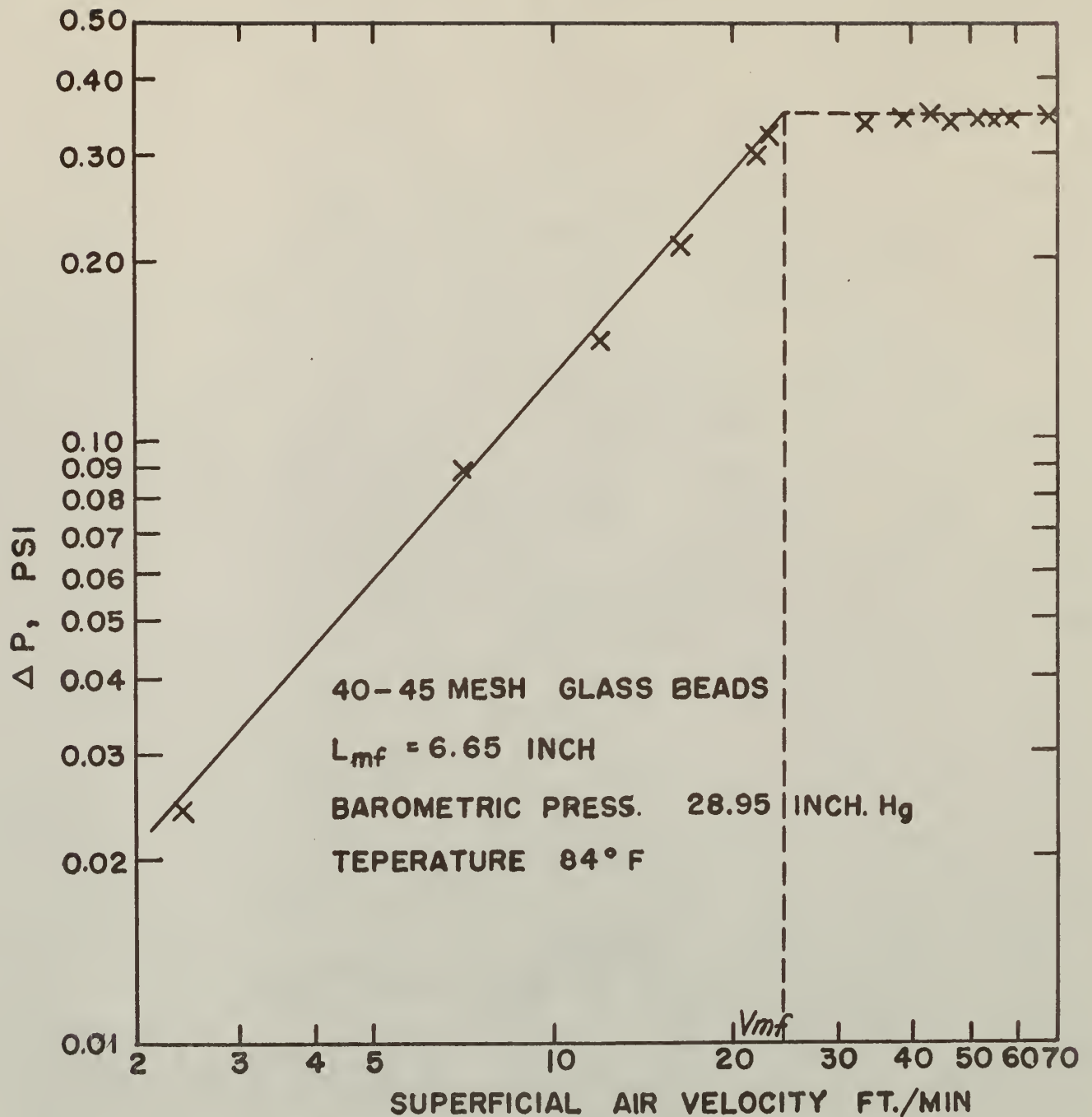
Fig. 28-(a). Pressure-drop-flow diagram for run S40-05.
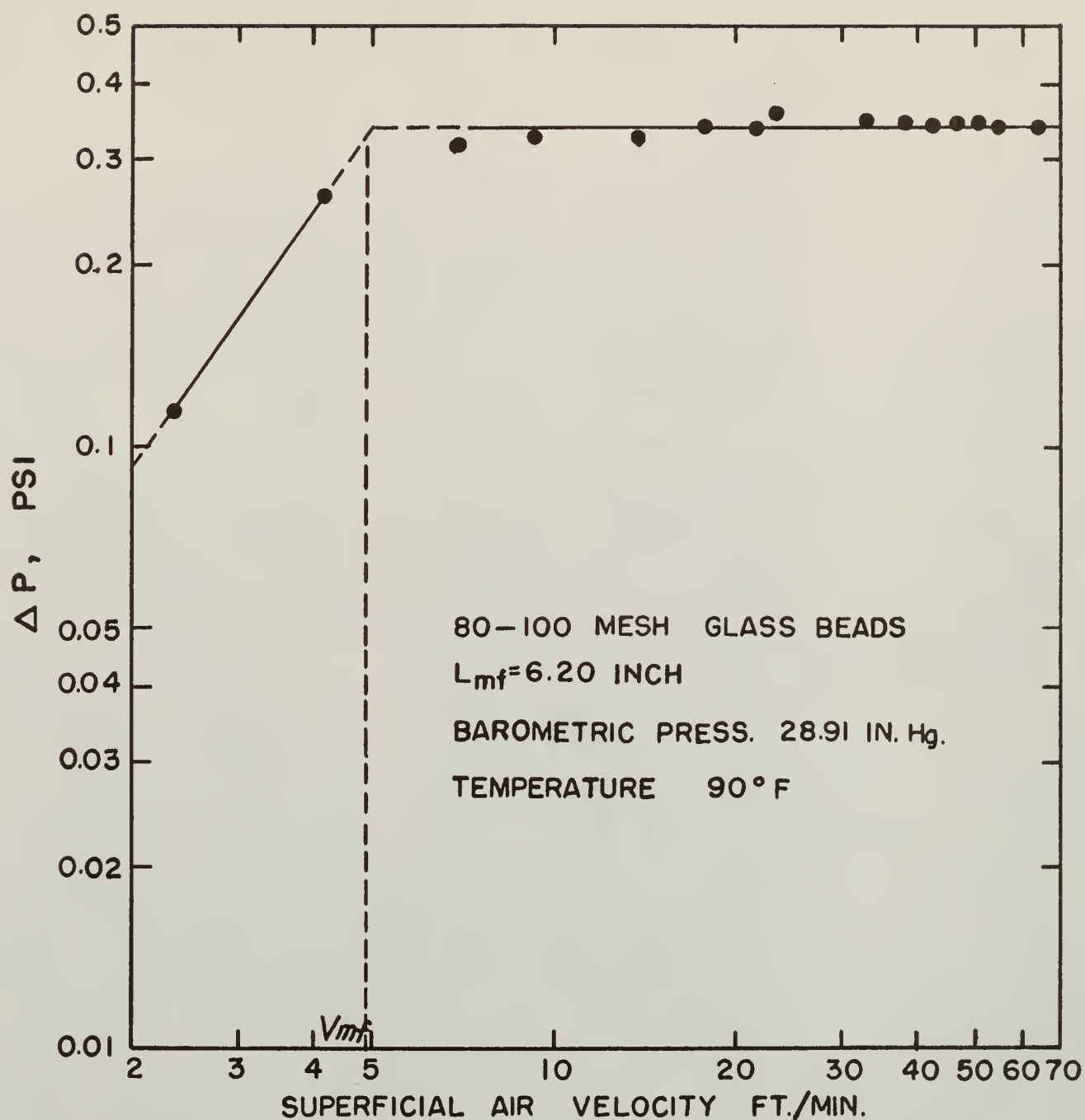
Fig. 28-(b). Pressure-drop-flow diagram for run S80-04.

$$f_K = \frac{g_c \Delta P}{L} \cdot \frac{\epsilon^3}{1-\epsilon} \cdot \frac{D_p}{\rho_F V^2} =$$

$$(9.028 \times 10^5)(\frac{D_p \rho_F V}{\mu} \cdot \frac{1}{1-\epsilon})^{-0.945}(\frac{D_p}{D_c})^{1.389}(\frac{L_{mf}}{D_c})^{-0.224} \qquad (25)$$

and, with the height defined by method (b):

$$f_K = \frac{g_c \Delta P}{L} \cdot \frac{\epsilon^3}{1-\epsilon} \cdot \frac{D_p}{\rho_F V^2} =$$

$$(8.80 \times 10^7)(\frac{D_p \rho_F V}{\mu} \cdot \frac{1}{1-\epsilon})^{-1.591}(\frac{D_p}{D_c})^{2.126}(\frac{L_{mf}}{D_c})^{-0.298} \qquad (26)$$

Equations (25) and (26) are plotted in Figs. (30) and (31) respectively.

The comparison plot for Equations (25) and 26) is shown in Fig. 32 in order to see which definition of height for fluidized bed gives better results in the proposed correlation for the pressure gradient. It can be seen from this plot that the height determined by method (a) gives more scattered correlation than that determined by method (b). It may be concluded, in the proposed dimensionless correlation of pressure gradient through fluidized bed, that the height determined by method (b) gives more consistent result than that by method (a).
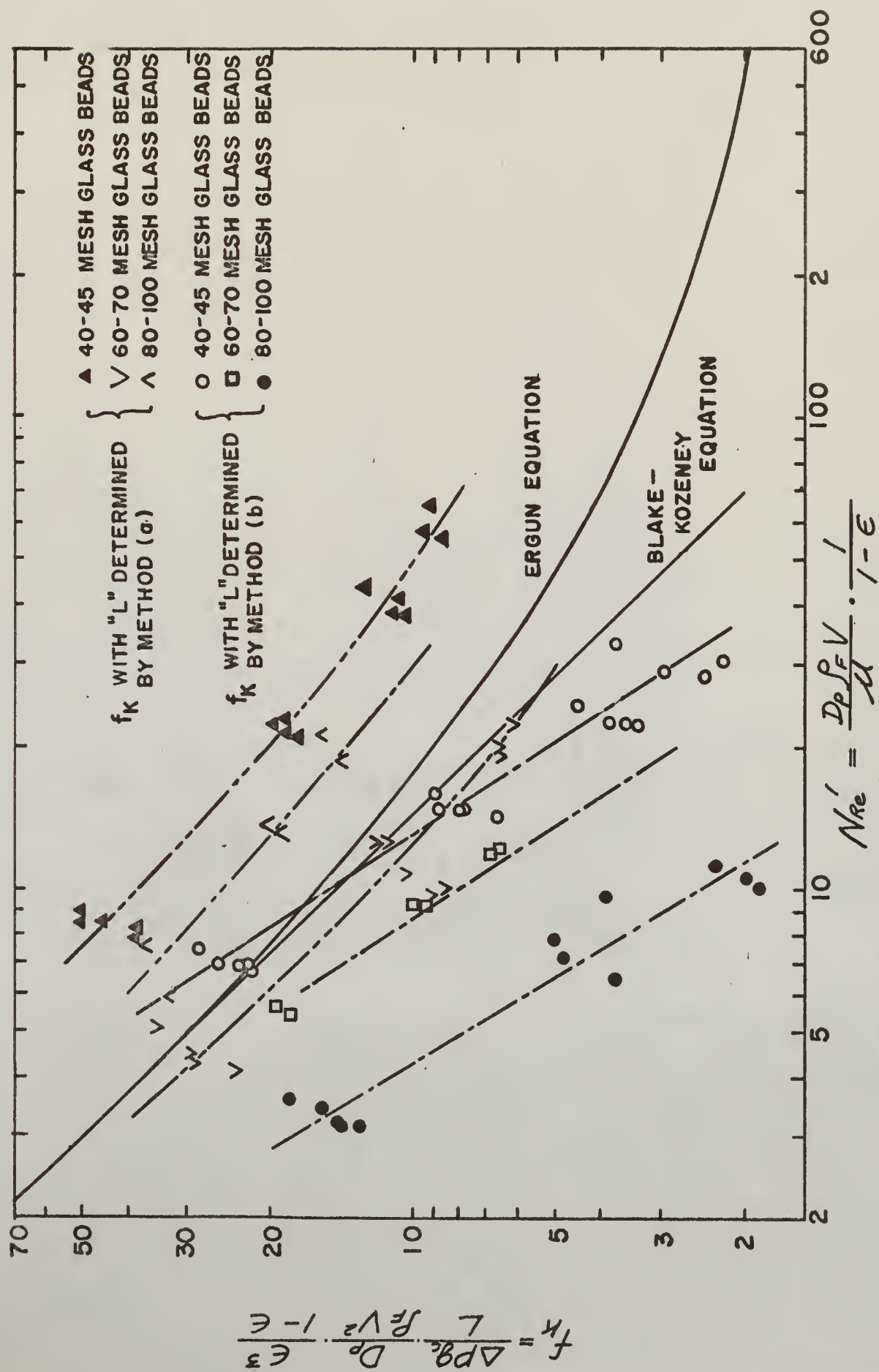
Fig. 29. Friction factor correlation.

$$f_K = \frac{\Delta P g_c}{L} \cdot \frac{D_p}{\rho_f V^2} \cdot \frac{\epsilon^3}{1-\epsilon}$$

$$N_{Re}' = \frac{D_p \rho_f V}{\mu} \cdot \frac{1}{1-\epsilon}$$

▲ 40-45 MESH GLASS BEADS
∨ 60-70 MESH GLASS BEADS    $f_K$ WITH "L" DETERMINED
∧ 80-100 MESH GLASS BEADS    BY METHOD (a)

○ 40-45 MESH GLASS BEADS
⊟ 60-70 MESH GLASS BEADS    $f_K$ WITH "L" DETERMINED
● 80-100 MESH GLASS BEADS    BY METHOD (b)

ERGUN EQUATION

BLAKE-KOZENEY EQUATION
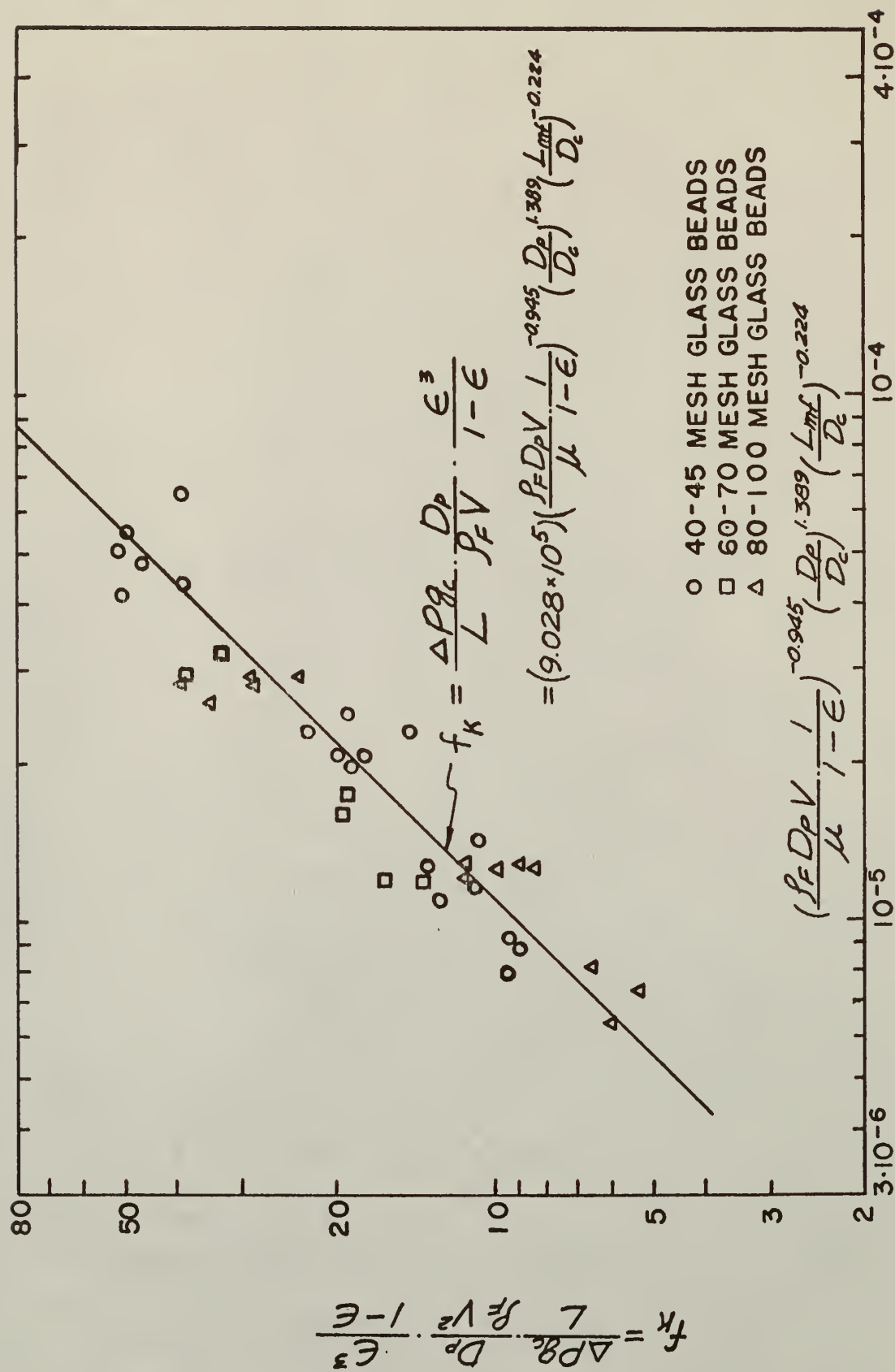
Fig. 30. Dimensionless correlation of friction factor with bed height determined by method (a)
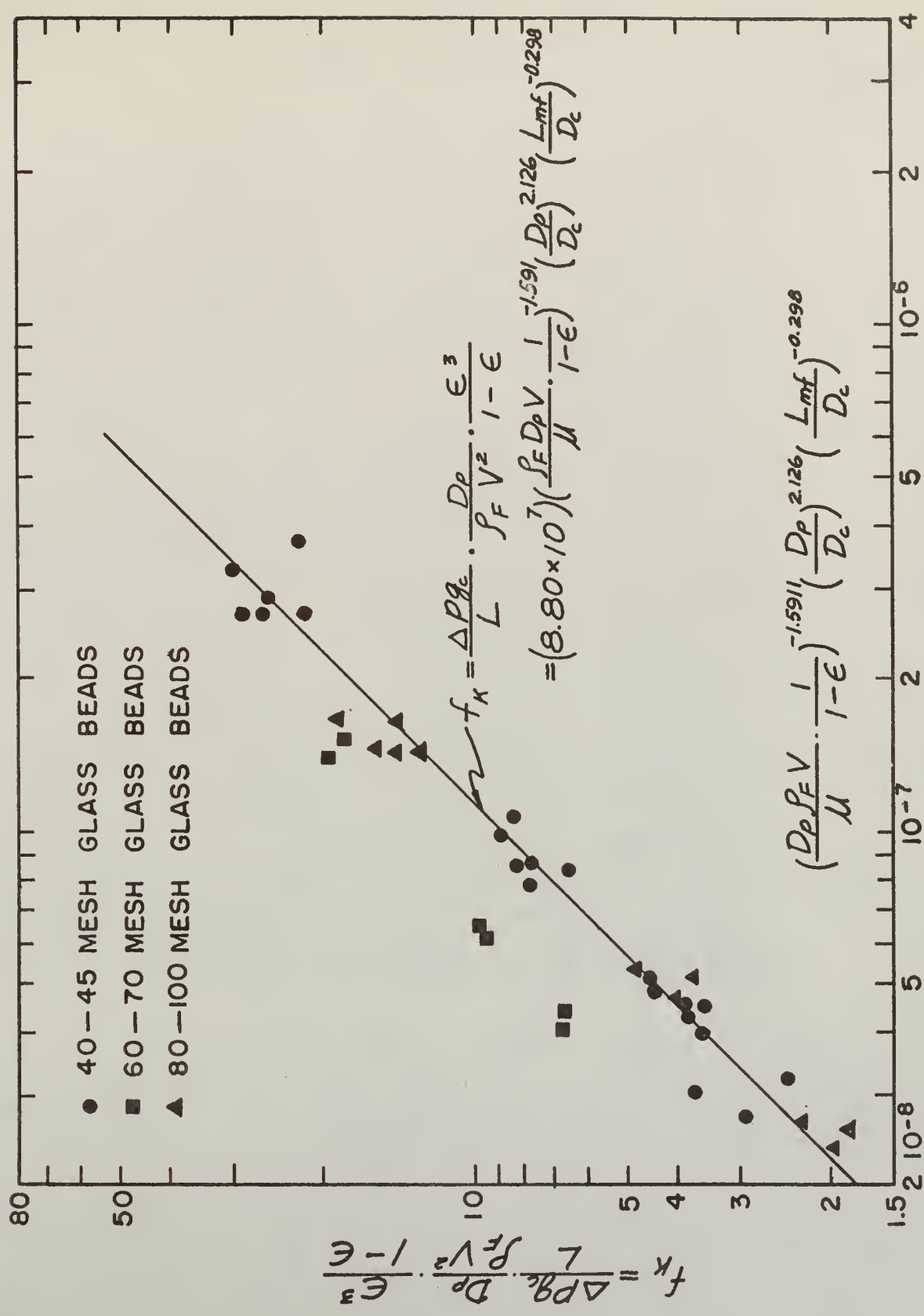
Fig. 31. Dimesionless correlation of friction factor with bed height determined by method (b).

● 40—45 MESH GLASS BEADS
■ 60—70 MESH GLASS BEADS
▲ 80—100 MESH GLASS BEADS

$$f_K = \frac{\Delta P g_c}{L} \cdot \frac{D_p}{\rho_F V^2} \cdot \frac{\epsilon^3}{1-\epsilon}$$

$$= (8.80 \times 10^7)\left(\frac{\rho_F D_p V}{\mu} \cdot \frac{1}{1-\epsilon}\right)^{-1.591}\left(\frac{D_p}{D_c}\right)^{2.126}\left(\frac{L_{mf}}{D_c}\right)^{-0.298}$$

X-axis: $\left(\frac{D_p \rho_F V}{\mu} \cdot \frac{1}{1-\epsilon}\right)^{-1.591}\left(\frac{D_p}{D_c}\right)^{2.126}\left(\frac{L_{mf}}{D_c}\right)^{-0.298}$

Y-axis: $f_K = \frac{\Delta P g_c}{L} \cdot \frac{D_p}{\rho_F V^2} \cdot \frac{\epsilon^3}{1-\epsilon}$
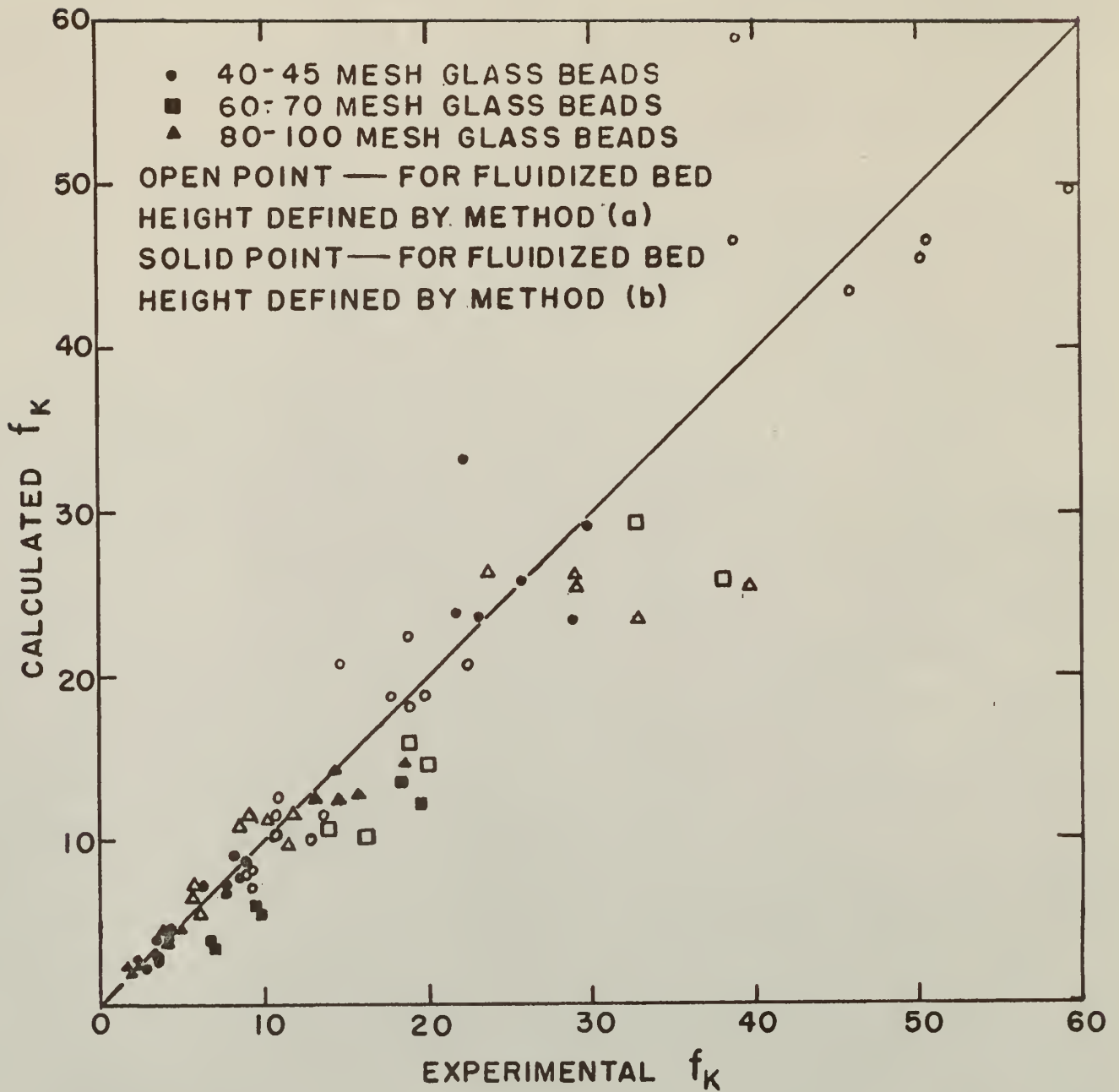
Fig. 32. Comparison of experimental $f_K$ to calculated $f_K$.

RESULTS AND DISCUSSION

$\gamma$-ray Technique as Applied to the Measurement
of Fluidized Bulk Density in Fluidized Beds

Among the several technical methods developed for the study of local
properties of a non-ideal two phase fluid, the $\gamma$-ray technique is a rela-
tively new one. It could be applied to the study of the formation and
behavior of bubbles in aggregative fluidized beds. By using a short-time
constant of the rate-count-meter to obtain the strip chart oscillograms,
the size, velocity and frequency of bubbles could be calculated (3). This
method also simplified the technical problems in the measurement of local
time-average density by using a long-time constant. The capacitance probe
method which was used by Dotson (5) and other investigators (18, 1)
appeared to disturb the flow pattern of the fluidizing vessel. The capaci-
tance probe inserted in the vessel, though it was small, should change the
local flow pattern. The properties investigated were influenced by the
probe and should be different from the flow pattern without such disturbance.
The $\gamma$-ray radiation technique can get rid of this disturbance completely.
The radiation passing through the fluidizing vessel has no effect on the
motion of fludizing mixtures.

Comparison of the Short-time Constant
to Long-time Constant Data

Although a 30 second long time constant was used for all the experimental
runs, the data obtained were compared with the data taken by short-time
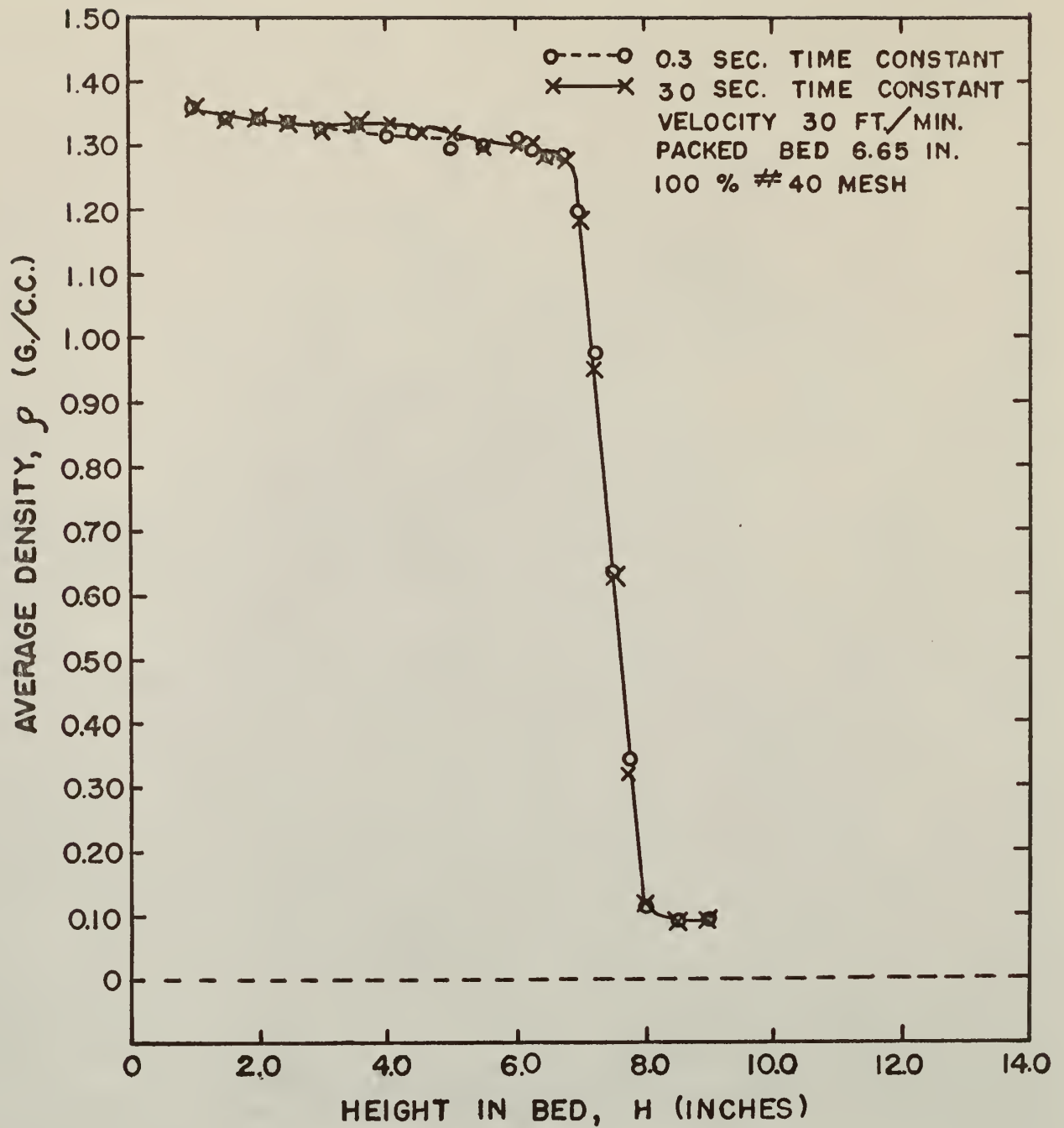
Fig. 34. Comparison of long and short time constants.

constant (0.3 second) in one particular run. The method used to calculate the line average density from the fluctuating CRM reading with a short-time constant was essentially the same as that used by Stewart (25). The axial density profiles obtained with both long-time constants and short-time constants are plotted in Fig. 34 for comparison. It can be seen that the results were almost identical, indicating that the sensitivity of the rate-count-meter was satisfactory. Considering the effort required to determine the axial density profile from the short-time constant data, we should be satisfied with the results obtained with a long-time constant for the purpose of the present studies. The density profiles were most directly obtained from the recording chart in long-time constant runs.

## Reproducibility

The accuracy of the experimental result was determined by the consistency test. The consistency test was satisfactory if the instrument operated was stable and the power to detect the $\gamma$-ray was consistent throughout. Occasionally, the instrument became damped during the process of experiment, and the density profile obtained would be quite skewed even in the constant density zone. This is shown in Fig. 35. This deficiency could be improved by checking the calibration before and after taking the data, and by avoiding any mechanical shock to the $\gamma$-ray source. In fact, the reproducibility obtained was good, considering that the fluidizing state of beds changed constantly owing to the nature of bed itself. Installing more than one $\gamma$-ray source and scintillation probe to measure the solid density from several directions of the fluidizing column would have been necessary to improve the reproducibility to any larger extent.
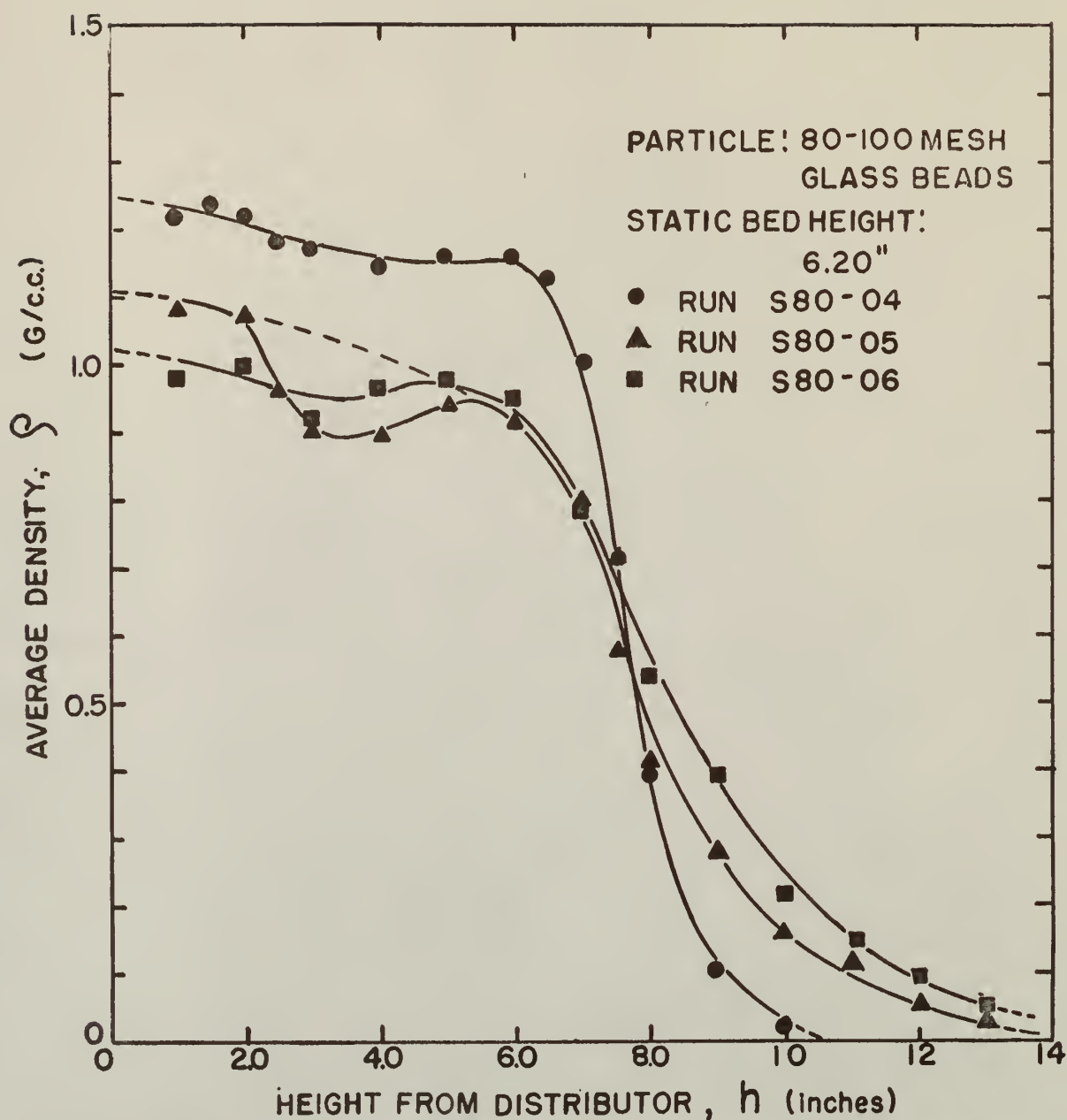
Fig. 35. The skewed density profile taken
when the instrument was damped.

The Importance of the "Bed Density Distribution"
to the Understanding of Heat and Mass Transfer Mechanism
in Catalyst Fluidized Bed Reactor

In spite of the wide application and rapid development of fluidization techniques, a complete understanding of the fundamental factors governing the performance of fluidizing units has been lacking (especially for gas-solid systems.). One way for expressing the bed performance is in terms of various degrees of so-called "good" or "bad" fluidization based on some definite index. This index is a direct measure of the effectiveness of heat and mass transfer as well as the conversion of reactants in chemical reactors (15, 16, 18).

Heat and mass transfer correlations for packed beds are rather complete in the literatures (11, 28). There has been a trend during the past 15 years for investigators in the field of fluidization to use the analogy to the packed bed reactor in the study of fluidized bed reactors. But the difficulties encountered were due to the non-uniform particle distribution throughout the fluidized bed. The reacting gas flowing through the fluidized bed is not only a tortuous flow through the constant void space as in packed beds, but in addition it is affected by the impacts between particles and the interaction between particles and the flowing medium. A quantitative measurement of the complexity of the flowing pattern in the fluidized bed is therefore important. The mass and heat transfer in the fluidized bed is governed by the surface and the movement of particles in the bed. It is certain that the transfer is better in the locations where the solid particles are dense and are constantly circulating.

Mickley et. al. (16) in their study of heat transfer for gas fluidized beds concludes:

The local time-mean wall-to-bed heat transfer coefficient varies with the axial position of heat transfer surface, decreasing with increasing distance above the bottom of the bed. On the other hand, the local coefficient is not significantly influenced by total height of the bed.

Shirai et.al.(23) also drew the same conclusion in studying the axial distribution of heat transfer coefficients. The axial distribution of particles-to-fluid heat transfer coefficients obtained by them is almost identical in shape to the axial density profile obtained in this work.

The close relationship between the axial distribution of the heat transfer coefficient and the axial density profile suggests that the study of the density profile of fluidized beds will help in understanding heat and mass transfer mechanism in the fluidized bed, since the particle behavior is the major factor affecting the performance of fluidized beds.

## CONCLUSION

The following significant conclusions have been drawn from the results of the present investigation:

1. With a long-time constant on the CRM, the $\gamma$-ray technique can be applied satisfactorily to the study of the axial density profile of the aggregative fluidized bed. The reproducibility is within the allowable error, except those at very high air velocities.

2. The data taken with a short-time constant is almost identical with the data using long-time constant.

3. Two distinct zones can be seen in the axial density profile, the constant density zone and the falling density zone. The line average density in the constant density zone decreases with increasing air velocity.

4.  The ratio of the static bed height to the column diameter instead of the static bed height itself is the important variable influencing the fluidizing state.

5.  Indices A and B can be used to describe aggregative fluidization. The greater the Index B, the more stable is the fluidizing bed.

6.  Indices A and B are correlated by the following empirical equations:

$$|A| = 1.349 \times 10^{-5} (N_{Re})^{0.978} (\frac{D_p}{D_c})^{-1.265} (\frac{L_{mf}}{D_c})^{0.3469} \tag{22}$$

$$|B| = 5.492 \times 10^{9} (N_{Re})^{-2.094} (\frac{D_p}{D_c})^{3.045} (\frac{L_{mf}}{D_c})^{0.3474} \tag{23}$$

7.  Among the three significant operational variables, air velocity, static bed height, and particle size, air velocity has the most pronounced effect on the fluidizing state.

8.  The bed height defined as the end point of the axial density profile corresponds to the visual maximum bed height. The more significant mean height of aggregative fluidized bed is defined as the cross point of the normalized density profile.

9.  Pressure gradient ($\Delta P/L$) correlation yields the following equations:

$$f_K = \frac{D_p}{\rho_F V^2} \cdot \frac{g_c \Delta P}{L} \cdot \frac{\epsilon^3}{1-\epsilon} =$$

$$(9.028 \times 10^5)(\frac{D_p V \rho_F}{\mu} \cdot \frac{1}{1-\epsilon})^{-0.945} (\frac{D_p}{D_c})^{1.389} (\frac{L_{mf}}{D_c})^{-0.224} \tag{25}$$

$$f_K = \frac{D_p}{\rho_F V^2} \cdot \frac{g_c \Delta P}{L} \cdot \frac{\epsilon^3}{1-\epsilon} =$$

$$(8.80 \times 10^8)(\frac{D_p V \rho_F}{\mu} \cdot \frac{1}{1-\epsilon})^{-1.591} (\frac{D_p}{D_c})^{2.126} (\frac{L_{mf}}{D_c})^{-0.298} \tag{26}$$

In equation (25), L was determined by method (a), and in equation (26), by method (b) or (c). The second equation correlates the data better than the first one.

10. The heterogeneous distribution of fluidized bulk density in the aggregative fluidized beds has a direct influence on the heat transfer, mass transfer and local conversion of fluidized bed reactors.

## ACKNOWLEDGEMENT

# BIBLIOGRAPHY

1. Bakker, P. J., and Heertjes, P. M.
   British Chem. Engr., 3, 240, 1958.

2. Bakker, P. J., and Heertjes, P. M.
   Chem. Engr. Sci., 4, 12, 260-71, 1960.

3. Baumgarten, P. K., and Pigford, R. L.
   A. I. Ch. E. Journal, 6, 115, 1960.

4. Bird, R. B., Stewart, W. E., and Lightfoot, E. N.
   Notes on Transport Theory. John Wiley and Sons Inc., N. Y., 1959.

5. Dotson, J. M.
   A. I. Ch. E. Journal, 5, 169, 1959.

6. Ergun, S., and Orning, A. A.
   Ind. Engr. Chem., 41, 1179-84, 1949.

7. Furukawa, J. and Ohmae, T. J.
   Ind. Chem., Chem. Sco. Japan, 54, 798-800, 1951.

8. Gomezplata, A., and Shuster, W. W.
   A. I. Ch. E. Journal, 3, 454, 1960.

9. Grohse, E. W.
   A. I. Ch. E. Journal, 1, 358, 1955.

10. Kern, D. Q.
    Process Heat Transfer. McGraw-Hill, New York, 1959 (pp. 38-40).

11. Leva, M.
    Fluidization. McGraw-Hill, New York, 1959.

12. Lewis, W. K., and Gilliland, E. R.
    Ind. Eng. Chem., 6, 40, 1949.

13. Massimilla, L., and Westwater, J. M.
    A. I. Ch. E. Journal, 6, 134, 1960

14. Matheson, G. L., Herbst, W. A., and Hole, P. H.
    Ind. Eng. Chem., 41, 1099, 1949.

15. May, W. G.
    Chem. Engr. Prog., 55, 49, 1959.

16. Mickley, H. S., Fairbank, D. F., and Hawthorn, R. D.
    Chem. Engr. Prog. Symp. Series, Heat Transfer, 57, 32, 1961.

17. Minet, R. G., Happel, J., and Kapfer, W.
    Presentation to American Inst. of Chem. Engr. Annual Meeting, Dec.,
    1959, San Francisco, Cal.

18. Morse, R. D., and Ballou, C. O.
    Chem. Engr. Prog., 47, 4, 199, 1951.

19. Petrick, M., and Swanson, B. S.
    Review Sci. Instruments, 29 (12), 1079-1085, Dec. 1958.

20. Richardson, J. F., and Zaki, W. N.
    Trans. Inst. Chem. Engr., 32, 1954.

21. Romero, J. B.
    Ph. D. Thesis, Univ. of Washington, 1959.

22. Shannon, P. T.
    Ph. D. Thesis, Ill. Inst. of Tech., 1958.

23. Shirai, T. et. al.
    Printed Note on "Heat Transfer in Gas Fluidized Bed."
    Tokyo Tech. Univ., Tokyo, Japan, 1960.

24. Shuster, W. W., and Kisliak, P.
    Chem. Engr. Prog., 48, 455, 1952.

25. Stewart, J. J.
    M. S. Thesis, Kansas State Univ., 1961.

26. Wilhelm, R. H., and Kwauk, M.
    Chem. Engr. Prog., 44, 201, 1948.

27. Yasui, G., and Johanson, L. N.
    A. I. Ch. E. Journal, 4, 445, 1958.

28. Zenz, F. A., and Othmer, D. F.
    Fluidization and Fluid-Particle Systems. Reinhold, New York, 1960.

## NOMENCLATURE

| | | |
|---|---|---|
| A | = | cross-sectional area of the fluidized bed, $1^2$. |
| A' | = | part of cross-sectional area of the fluidized bed, $1^2$. |
| $A_r$ | = | projected area of $\gamma$-beam path, $1^2$. |
| $A_o$ | = | constant, dimensionless. |
| $B_o$ | = | constant, dimensionless. |
| A | = | index of fluidized bed, dimensionless. |
| B | = | index of fluidized bed, dimensionless. |
| $d_{Al}$ | = | thickness of spacer aluminum, 1. |
| $D_c$ | = | inner diameter of fluidized column, 1. |
| $d_c$ | = | wall thickness of fluidized column, 1. |
| $D_p$ | = | diameter of particle, 1. |
| $D_p'$ | = | width of packed particle bed in the direction of radiation beam, 1. |
| $D_s$ | = | width of spacer, 1. |
| $f_K$ | = | friction factor, dimensionless. |
| G | = | volumetric air velocity, $1^3/\theta$ . |
| $G_b$ | = | volumetric bubble velocity, $1^3/\theta$ . |
| $g_c$ | = | conversion from force to mass, $ml/F\theta^2$. |
| $G_{mf}$ | = | volumetric velocity of minimum fluidization, $1^3/\theta$ . |
| h | = | height above the distribution in bed, 1. |
| $I/I_o$ | = | fraction of photons remaining in the beam after passage through absorber of thickness d, dimensionless. |
| L | = | height of fluidized bed, 1. |
| $L_{mf}$ | = | static (on-set) height of bed, 1. |
| M | = | total particle weight in bed, m. |
| M' | = | bed weight obtained from integrated area (consistency test), m. |

$M_{s_1}$ = weight of particles fluidizing above $L_{mf}$, m.

$M_{s_2}$ = weight of particles fluidizing below $L_{mf}$, m.

$N_a$ = Avagodro's number ($6.025 \times 10^{23}$ nuclei/g-mol).

$N_{Re}$ = Reynolds number, $V\rho_F D_p/\mu$ , dimensionless.

$N_{Re}'$ = modified Reynolds number, $V\rho_F D_p/\mu \cdot 1/1-\epsilon$ , dimensionless.

$\triangle P$ = pressure drop through fluidized bed, $F/1^2$

$t_b$ = the residence time of bubbles in the bed below $L_{mf}$, $\Theta$ .

$V$ = superficial air velocity, $1/\Theta$.

$\bar{V}_b$ = average linear velocity of bubbles, $1/\Theta$ .

$V_{mf}$ = minimum velocity of fluidization, $1/\Theta$.

$Vol_b$ = the volume occupied by bubbles below $L_{mf}$, $1^3$.

$Vol_{s_1}$ = volume of particles fluidizing above $L_{mf}$, $1^3$.

$Vol_{s_2}$ = volume of particles fluidizing below $L_{mf}$, $1^3$.


Greek Letters

$\alpha'$ = constant.

$\beta'$ = constant.

$\epsilon_{mf}$ = porosity of the fluidized bed at on-set fluidization.

$\rho$ = fluidized bulk density.

$\rho_{Al}$ = density of aluminum.

$\rho_C$ = density of the fluidizing column material.

$\rho_d$ = fluidized bulk density at the position corresponding to the static bed height.

$\bar{\rho}_d$ = average line density in the constant density zone.

$\rho_F$ = density of fluid.

$\rho_{mf}$ = fluidized bulk density at on-set fluidization.

$\rho_{pa}$ = bulk density of bed at packed state.

$\rho_s$ = density of solid particle.

$\phi$ = constant.

$\sigma$ = microscopic absorption cross-section.

$\mu$ = viscosity of fluid.

$\mu_m$ = absorption coefficient.

APPENDIX

APPENDIX I

Table 3. Summary of the experimental and calculated data.

| Run No. | | P40-01 | P40-02 | P40-03 | P40-04 | P40-05 | P40-06 |
|---|---|---|---|---|---|---|---|
| Part. Size, $D_p$ (inch) | | 0.0153 | 0.0153 | 0.0153 | 0.0153 | 0.0153 | 0.0153 |
| Static Bd. Ht. (inch) | | 2.75 | 2.75 | 2.75 | 2.75 | 6.20 | 6.20 |
| Air Flow Rate (ft/min.) | | 30 | 60 | 90 | 110 | 30 | 60 |
| Exp'd. Bd. Ht.; L, (inch) | | | | | | | |
| (by method a) | | 3.516 | 4.872 | 5.904 | 7.608 | 8.436 | 10.608 |
| (by method b) | | 2.952 | 3.408 | 3.552 | 3.900 | 6.948 | 7.104 |
| Pres. Drop per Unit Bd. Ht. $\Delta P/L$ | | | | | | | |
| (by method a) | | 56.075 | 40.468 | 33.394 | 25.915 | 59.255 | 47.123 |
| Modified Reynold's No. (by method b) | | 66.788 | 57.852 | 55.506 | 50.554 | 71.945 | 70.366 |
| $N'_{Re} = \dfrac{D_p\, \rho_F V}{\mu(1-\epsilon)}$ | (a) | 8.238 | 22.844 | 41.334 | 65.186 | 8.916 | 22.369 |
| | (b) | 6.914 | 15.967 | 24.889 | 33.362 | 7.352 | 14.955 |
| Reynold's Number $N_{Re} = \dfrac{D_p\, \rho_F V}{\mu}$ | | 3.872 | 7.744 | 11.574 | 14.145 | 3.941 | 7.852 |
| $\left[ D_p / \eta_c \text{ ratio} \right] \times 10^3$ | | 3.848 | 3.848 | 3.848 | 3.848 | 3.848 | 3.848 |
| Friction factor $f_K = \dfrac{g_c \Delta P}{L} \cdot \dfrac{D_p}{\rho_F V^2} \cdot \dfrac{\epsilon^3}{1-\epsilon}$ | (a) | 39.013 | 18.931 | 10.904 | 9.400 | 50.267 | 19.876 |
| | (b) | 22.314 | 8.946 | 4.477 | 3.736 | 28.938 | 7.779 |
| Index A | | -0.054 | -0.105 | -0.172 | -0.207 | -0.069 | -0.145 |
| Index B | | -16.780 | -3.437 | -1.391 | -0.813 | -21.459 | -3.150 |

Note: Index A is the correlated intercept for density falling-zone profile.
Index B is the correlated slope for density falling-zone profile.

Table 3. Summary of the experimental and calculated data. (Cont.)

| Run No. | | P40-07 | P40-08 | P40-09 | P40-10 | P40-11 | P40-12 |
|---|---|---|---|---|---|---|---|
| Part. Size, $D_p$ (inch) | | 0.0153 | 0.0153 | 0.0153 | 0.0153 | 0.0153 | 0.0153 |
| Static Bd. Ht. (inch) | | 5.20 | 6.20 | 9.10 | 9.10 | 9.10 | 9.10 |
| Air Flow Rate (ft/min.) | | 90 | 110 | 30 | 60 | 90 | 110 |
| Exp'd Bd. Ht., L, (inch) | | | | | | | |
| (by method a) | | 12.120 | 14.568 | 11.148 | 14.556 | 17.748 | 21.936 |
| (by method b) | | 7.140 | 7.200 | 9.552 | 10.380 | 10.464 | 11.124 |
| Pres. Drop per Unit Bd. Ht. $\Delta P/L$ | | | | | | | |
| (by method a) | | 41.244 | 34.313 | 67.004 | 51.317 | 42.087 | 34.052 |
| (by method b) | | 70.011 | 69.427 | 78.199 | 71.962 | 71.384 | 67.149 |
| Modified Reynold's No. $N'_{Re} = \dfrac{D_p}{\mu} \dfrac{\rho_F V}{(1-\epsilon)}$ | (a) | 38.023 | 55.912 | 7.958 | 20.786 | 38.063 | 56.907 |
| | (b) | 22.435 | 27.632 | 6.845 | 14.830 | 22.459 | 28.859 |
| Reynold's Number $N_{Re} = \dfrac{D_p \, \rho_F V}{\mu}$ | | 11.711 | 14.314 | 3.915 | 7.816 | 11.723 | 14.170 |
| $\left[ D_p/D_c \text{ ratio} \right] \times 10^3$ | | 3.848 | 3.848 | 3.848 | 3.848 | 3.848 | 3.848 |
| Friction factor $f_K = \dfrac{g_c \Delta P}{L} \cdot \dfrac{D_p}{\rho_F V^2} \cdot \dfrac{\epsilon^3}{1-\epsilon}$ | (a) | 10.741 | 8.945 | 38.782 | 18.042 | 10.949 | 9.482 |
| | (b) | 3.546 | 2.432 | 23.283 | 7.862 | 3.612 | 2.952 |
| Index A | | -0.242 | -0.279 | -0.0678 | -0.153 | -0.262 | -0.291 |
| Index B | | -1.645 | -1.133 | -36.960 | -5.203 | -1.213 | -0.815 |

Note: Index A is the correlated intercept for density falling-zone profile.
Index B is the correlated slope for density falling-zone profile.

Table 3. Summary of the experimental and calculated data. (Cont.)

| Run No. | | S40-01 | S40-02 | S40-03 | S40-05 | S40-06 | S40-07 |
|---|---|---|---|---|---|---|---|
| Part. Size, $D_p$ (inch) | | 0.0153 | 0.0153 | 0.0153 | 0.0153 | 0.0153 | 0.0153 |
| Static Bd. Ht. (inch) | | 3.25 | 3.25 | 3.25 | 6.65 | 6.65 | 6.65 |
| Air Flow Rate (ft/min.) | | 30 | 60 | 90 | 30 | 60 | 90 |
| Exp'd. Bd. Ht., L, (inch) | | | | | | | |
| (by method a) | | 4.875 | 5.982 | 7.580 | 8.976 | 12.372 | 14.964 |
| (by method b) | | 3.652 | 3.780 | 4.000 | 7.176 | 7.764 | 7.932 |
| Pres. Drop per Unit Bd. Ht. $\Delta P/L$ | | | | | | | |
| (by method a) | | 53.327 | 43.458 | 34.296 | 59.360 | 43.066 | 35.606 |
| (by method b) | | 71.185 | 68.774 | 64.992 | 74.249 | 68.626 | 67.172 |
| Modified Reynold's No. $N'_{Re} = \dfrac{D_p \, \rho_F \, V}{\mu(1-\epsilon)}$ | (a) | 9.478 | 23.766 | 44.404 | 8.601 | 20.059 | 43.321 |
| | (b) | 7.246 | 15.020 | 23.438 | 6.871 | 14.918 | 22.735 |
| Reynold's Number $N_{Re} = \dfrac{D_p \, \rho_F \, V}{\mu}$ | | 3.871 | 7.750 | 11.898 | 3.827 | 7.683 | 11.567 |
| $[D_p/D_c$ ratio $] \times 10^3$ | | 3.848 | 3.848 | 3.848 | 3.848 | 3.848 | 3.848 |
| Friction factor $f_K = \dfrac{g_c \Delta P}{L} \cdot \dfrac{D_p}{\rho_F V^2} \cdot \dfrac{\epsilon^3}{1-\epsilon}$ | (a) | 59.471 | 22.513 | 13.564 | 50.673 | 14.618 | 12.872 |
| | (b) | 29.761 | 8.391 | 4.541 | 25.752 | 8.414 | 3.829 |
| Index A | | -0.046 | -0.083 | -0.158 | -0.069 | -0.122 | -0.215 |
| Index B | | -10.391 | -3.327 | -1.033 | -23.996 | -3.150 | -1.150 |

Note: Index A is the correlated intercept for density falling-zone profile.
Index B is the correlated slope for density falling-zone profile.

Table 3. Summary of the experimental and calculated data. (Cont.)

| Run No. | S40-09 | S40-10 | P80-04 | P80-05 | P80-06 |
|---|---|---|---|---|---|
| Part. Size, $D_p$ (inch) | 0.0153 | 0.0153 | 0.00642 | 0.00642 | 0.00642 |
| Static Bd. Ht. (inch) | 9.40 | 9.40 | 6.10 | 6.10 | 6.10 |
| Air Flow Rate (ft/min.) | 30 | 60 | 30 | 60 | 90 |
| Exp'd. Bd. Ht., L, (inch) | | | | | |
| (by method a) | 12.290 | 15.490 | 11.004 | 13.632 | 16.356 |
| (by method b) | 9.750 | 10.232 | 7.380 | 7.500 | 7.752 |
| Pres. Drop per Unit Bd. Ht. $\Delta P/L$ | | | | | |
| (by method a) | 61.235 | 48.578 | 39.9346 | 32.2360 | 26.8672 |
| (by method b) | 77.178 | 73.543 | 59.5389 | 58.5734 | 56.7259 |
| Modified Reynold's No. $N'_{Re} = \dfrac{D_p \rho_F V}{\mu (1 - \epsilon)}$ (a) | 8.487 | 21.410 | 5.058 | 12.532 | 22.254 |
| (b) | 6.741 | 14.145 | 3.394 | 6.899 | 10.542 |
| Reynold's Number $N_{Re} = \dfrac{D_p \rho_F V}{\mu}$ $\left[D_p/D_c \text{ ratio}\right] \times 10^3$ | 3.900 | 7.838 | 1.639 | 3.278 | 4.854 |
| ($D_p/D_c$ ratio) | 3.848 | 3.848 | 1.6140 | 1.6140 | 1.6140 |
| Friction factor $f_K = \dfrac{g_c \Delta P}{L} \cdot \dfrac{D_p}{\rho_F V^2} \cdot \dfrac{\epsilon^3}{1 - \epsilon}$ (a) | 46.036 | 18.753 | 34.756 | 11.330 | 6.056 |
| (b) | 21.806 | 6.577 | 15.573 | 4.069 | 1.991 |
| Index A | -0.080 | -0.175 | - | - | - |
| Index B | -25.685 | -2.925 | - | - | - |

Note: Index A is the correlated intercept for density falling-zone profile.
Index B is the correlated slope for density falling-zone profile.

Table 3. Summary of the experimental and calculated data. (Cont.)

| Run No. | | P80-07 | P80-08 | S80-01 | S80-02 | S80-03 | S80-04 |
|---|---|---|---|---|---|---|---|
| Part. Size, $D_p$ (inch) | | 0.00642 | 0.00642 | 0.00642 | 0.00642 | 0.00642 | 0.00642 |
| Static Bd. Ht. (inch) | | 8.75 | 8.75 | 3.25 | 3.25 | 3.25 | 6.20 |
| Air Flow Rate (ft/min.) | | 30 | 60 | 30 | 60 | 90 | 30 |
| Exp'd. Bd. Ht., L, (inch) | | | | | | | |
| (by method a) | | 13.356 | 15.300 | 6.348 | 7.308 | 7.860 | 10.236 |
| (by method b) | | 10.020 | 10.284 | 4.164 | 4.224 | 4.356 | 7.224 |
| Pres. Drop per Unit Bd. Ht. $\Delta P/L$ | | | | | | | |
| (by method a) | | 51.258 | 44.745 | 37.075 | 32.220 | 29.943 | 40.317 |
| (by method b) | | 68.339 | 66.592 | 56.577 | 55.734 | 54.044 | 62.110 |
| Modified Reynold's No. $N'_{Re} = \dfrac{D_p \, \rho_F \, V}{\mu(1-\epsilon)}$ | (a) | 4.251 | 9.741 | 5.374 | 12.373 | 19.964 | 4.480 |
| | (b) | 3.191 | 6.550 | 3.523 | 7.157 | 11.065 | 3.159 |
| Reynold's Number $N_{Re} = \dfrac{D_p \, \rho_F \, V}{\mu}$ $\left[ D_p/D_c \text{ ratio} \right] \times 10^3$ | | 1.628 | 3.757 | 1.608 | 3.217 | 4.825 | 1.586 |
| | | 1.614 | 1.614 | 1.614 | 1.614 | 1.614 | 1.614 |
| Friction factor $f_K = \dfrac{g_c \Delta P}{L} \cdot \dfrac{D}{\rho_F V^2} \cdot \dfrac{\epsilon^3}{1-\epsilon}$ | (a) | 28.881 | 9.069 | 39.673 | 11.682 | 5.588 | 28.991 |
| | (b) | 14.448 | 3.910 | 18.510 | 4.814 | 2.299 | 14.429 |
| Index A | | - | - | -0.079 | -0.167 | -0.208 | -0.106 |
| Index B | | - | - | -2.142 | -1.406 | -1.135 | -4.765 |

Note: Index A is the correlated intercept for density falling-zone profile.
Index B is the correlated slope for density falling-zone profile.

Table 3. Summary of the experimental and calculated data. (Cont.)

| Run No. | S80-05 | S80-06 | S80-07 | S80-08 |
|---|---|---|---|---|
| Part.Size, $D_p$ (inch) | 0.00642 | 0.00642 | 0.00642 | 0.00642 |
| Static Bd. Ht. (inch) | 6.20 | 6.20 | 9.35 | 9.35 |
| Air Flow Rate (ft./min.) | 60 | 90 | 30 | 60 |
| Exp'd. Bd. Ht., L, (inch) | | | | |
| (by method a) | 12.276 | 14.472 | 13.764 | 17.184 |
| (by method b) | 7.320 | 7.632 | 10.800 | 11.316 |
| Pres. Drop per Unit Bd. Ht. $\triangle P/L$ | | | | |
| (by method a) | 36.550 | 31.004 | 45.6415 | 36.5579 |
| (by method b) | 61.296 | 58.790 | 58.1676 | 55.5270 |
| Modified Reynold's No. $N'_{Re} = \dfrac{D_p\,\rho_F V}{\mu(1-\epsilon)}$ (a) | 10.830 | 19.064 | 4.028 | 10.0506 |
| (b) | 6.452 | 10.034 | 3.163 | 6.6268 |
| Reynold's Number $N_{Re} = \dfrac{D_p\,\rho_F V}{\mu}\left[D_p/D_c\ \text{ratio}\right] \times 10^3$ | 3.195 | 4.766 | 1.600 | 3.200 |
| | 1.614 | 1.614 | 1.614 | 1.614 |
| Friction factor $f_K = \dfrac{\rho_c \triangle P}{L}\cdot\dfrac{D_p}{\rho_F V^2}\cdot\dfrac{\epsilon^3}{1-\epsilon}$ (a) | 10.174 | 5.479 | 23.555 | 8.506 |
| (b) | 3.737 | 1.865 | 12.980 | 3.720 |
| Index A | -0.166 | -0.199 | -0.098 | -0.163 |
| Index B | -2.185 | -1.238 | -7.924 | -2.161 |

Note:  Index A is the correlated intercept for density falling-zone profile.
       Index B is the correlated slope for density falling-zone profile.

Table 3. Summary of the experimental and calculated data. (Cont.)

| Run No. | EX-01 | EX-02 | EX-03 | EX-04 | EX-05 | EX-06 |
|---|---|---|---|---|---|---|
| Part. Size, $D_p$ (inch) | 0.00906 | 0.00906 | 0.00906 | 0.00906 | 0.00906 | 0.00906 |
| Static Bd. Ht. (inch) | 5.0 | 5.0 | 5.0 | 6.0 | 6.0 | 6.0 |
| Air Flow Rate (ft/min.) | 35.6 | 55.4 | 69.3 | 35.6 | 55.4 | 69.3 |
| Exp'd Bd. Ht., L, (inch) | | | | | | |
| (by method a) | 7.50 | 9.20 | 11.80 | 9.80 | 11.40 | 12.30 |
| (by method b) | 5.87 | 6.39 | 6.6 | 7.22 | 7.71 | 8.00 |
| Pres. Drop per Unit Bd. Ht. $\Delta P/L$ | | | | | | |
| (by method a) | 60.890 | 49.636 | 38.703 | 55.917 | 47.955 | 44.554 |
| (by method b) | 77.798 | 71.467 | 69.195 | 75.901 | 71.078 | 68.498 |
| Modified Reynold's No. $N'_{Re} = \dfrac{D_p \rho_F V}{\mu (1 - \epsilon)}$ (a) (b) | 6.927 / 5.421 | 13.223 / 9.184 | 21.271 / 11.989 | 7.563 / 5.572 | 13.654 / 9.234 | 18.478 / 12.018 |
| Reynold's Number $N_{Re} = \dfrac{D_p \rho_F V}{\mu}$ | 2.770 | 4.309 | – | – | – | – |
| $\left[ D_p/D_c \text{ ratio} \right] \times 10^3$ | 2.278 | 2.278 | 2.278 | 2.278 | 2.278 | 2.278 |
| Friction factor $f_K = \dfrac{g_c \Delta P}{L} \cdot \dfrac{D_p}{\rho_F V^2} \cdot \dfrac{\epsilon^3}{1 - \epsilon}$ (a) (b) | 32.923 / 18.310 | 19.008 / 9.548 | 16.247 / 6.590 | 38.248 / 19.619 | 19.866 / 9.706 | 13.936 / 6.748 |
| Index A | -0.1319 | -0.1420 | -0.1717 | -0.1029 | -0.1630 | -0.1988 |
| Index B | -5.600 | -2.4500 | -2.035 | -6.1900 | -2.850 | -2.1420 |

Note:  Index A is the correlated intercept for density falling-zone profile.
       Index B is the correlated slope for density falling-zone profile.

APPENDIX II

(A)  Derivation of the Dimensionless Equation for Correlating Pressure
     Gradient in the Aggregative Fluidized Bed----Friction Factor, $f_K$

The pressure gradient, $\triangle P/L$, has been found experimentally to be in-
fluenced by the following properties of column, fluid, and particles:  column
diameter, $D_c$, fluid density, $\rho_F$, viscosity, $\mu$, velocity, $V$, particle diameter,
$D_p$, and static bed height, $L_{mf}$.  The primary relationship existing between the
pressure gradient and the variables is (6, 11, 28):

$$\frac{\triangle P}{L} = \phi \, (D_c)^h \, (\rho_F)^i \, (\mu)^j \, (V)^k \, (D_p)^m \, (L_{mf})^n \, (g_c)^p \tag{27}$$

where $\phi$, h, i, j, k, m, n, q, are unknown constants, and $g_c$ is the con-
version constant between force and mass.

Equation (27) is rewritten using the dimensions of each variable as:

$$\frac{F}{l^3} = \phi \, (1)^h \, (\frac{m}{l})^i \, (\frac{m}{1 - \Theta})^j \, (\frac{1}{\Theta})^k \, (1)^m \, (1)^n \, (\frac{ml}{F\Theta^2})^q \tag{28}$$

Summing the exponents of equation (28),

$\sum F, \qquad 1 = - q$

$\sum 1, \qquad - 3 = h - 3i - j + k + m + n + q$

$\sum m, \qquad 0 = i + j + q$

$\sum \Theta, \qquad 0 = - j - k - 2q$

To solve the above four equations for seven unknowns, the Bridgman
Pi-Theorem[*] is used.  Choosing h, j, n, as three unknowns, then,

---

[*]Bridgman's Pi-theorem:  If there are N number of equations to solve for K
unknowns, the number of dimensionless groups to be obtained is N - K + 1,
and N - K of unknowns retain  numerically unsolved.

$$q = -1$$

$$i = -j - q = 1 - j$$

$$k = -j - 2q = 2 - j$$

$$m = -3 - h + 3i + j - k - n - q$$

$$= -h - j - n - 1$$

Substituting the above values into equation (27):

$$(\frac{\triangle P}{L}) = \phi (D_c)^h (\rho_F)^{1-j} (\mu)^j (V)^{2-j} (D_p)^{-1-h-j-n} (L_{mf})^n (g_c)^{-1} \tag{29}$$

and rearranging:

$$\frac{g_c \triangle P}{L} = \phi (\frac{\mu}{\rho_F V D_p})^j (\frac{D_c}{D_p})^h (\frac{L_{mf}}{D_p})^n (\frac{\rho_F V^2}{D_p})$$

or,

$$(\frac{g_c \triangle P}{L} \cdot \frac{D_p}{\rho_F V^2}) = \phi (\frac{\rho_F V D_p}{\mu})^{-j} (\frac{D_p}{D_c})^{-h-n} (\frac{L_{mf}}{D_c})^n$$

Let $-j = a$, $-h - n = b$, $n = c$, then:

$$(\frac{g_c \triangle P}{L} \cdot \frac{D_p}{\rho_F V^2}) = \phi (\frac{\rho_F V D_p}{\mu})^a (\frac{D_p}{D_c})^b (\frac{L_{mf}}{D_c})^c \tag{30}$$

Based on the theoretical consideration (for the hydraulic radius of column and the wetted surface of particles, etc.), the friction factor, $f_K$, derived for the packed bed has been modified by multiplying the dimensionless factor, $\epsilon^3/1 - \epsilon$ (6), and the Reynolds number, $\rho_F V D_p/\mu$, has been modified by multiplying by $1/1 - \epsilon$ (where $\epsilon$ is the void fraction of the fluid-particles bed.) The dimensionless equation then becomes:

$$f_K = (\frac{g_c \triangle P}{L} \cdot \frac{D_p}{\rho_F V^2} \cdot \frac{\epsilon^3}{1-\epsilon})$$

$$= \phi (\frac{\rho_F V D_p}{\mu} \cdot \frac{1}{1-\epsilon})^a (\frac{D_p}{D_c})^b (\frac{L_{mf}}{D_c})^c \tag{24}$$

(B)   Derivation of the Dimensionless equation for Correlating Indices A and
      B.

The results of the previous and the present investigation indicate that
(5, 25):

$$|A| = \alpha'(D_c)^h (\rho_F)^i (\mu)^j (V)^k (D_p)^m (L_{mf})^n \tag{31}$$

$$1 = \alpha'(1)^h (m/l^3)^i (m/l - \theta)^j (1/\theta)^k (1)^m (1)^n$$

$$\Sigma m, \quad 0 = i + j$$

$$\Sigma l, \quad 0 = h - 3i - j + k + m + n$$

$$\Sigma \theta, \quad 0 = -j - k$$

Holding h, j, n, as unknown constants

$$i = -j$$

$$k = -j$$

$$m = -h + 3i + j - k - n = -h - j - n$$

substituting these into equation (31),

$$|A| = \alpha'(D_c)^h (\rho_F)^{-j} (\mu)^j (V)^{-j} (D_p)^{-h - j - n} (L_{mf})^n \tag{32}$$

Rearranging:

$$|A| = \alpha'(\mu / \rho_F V D_p)^j (D_c/D_p)^h (L_{mf}/D_p)^n$$

$$= \alpha'(\rho_F V D_p/\mu)^{-j} (D_p/D_c)^{-h - n} (L_{mf}/D_c)^n$$

Let $- j = a$, $- h - n = b$, $n = c$, then:

$$|A| = \alpha'(\rho_F V D_p/\mu)^a (D_p/D_c)^b (L_{mf}/D_c)^c \tag{20}$$

By the similar method, the dimensionless equation for correlating index B can
be obtained as:

$$|B| = \beta'(\rho_F V D_p/\mu)^{a'} (D_p/D_c)^{b'} (L_{mf}/D_c)^{c'} \tag{21}$$

AXIAL SOLID-DENSITY DISTRIBUTION IN
GAS SOLID FLUIDIZED BEDS

by

CHAU JEN LEE

B. S., National Taiwan University, 1957

———————————

AN ABSTRACT OF A THESIS

submitted in partial fulfillment of the

requirements for the degree

MASTER OF SCIENCE

Department of Chemical Engineering

KANSAS STATE UNIVERSITY
Manhattan, Kansas

1961

$\gamma$-ray attenuation method was applied to determine the axial fluidizing bulk density profile for an air-solid aggregative fluidized bed. Two distinct density zones, constant and falling, were observed except for the bed fluidizing at very high air velocity.

The average density of the constant zone $\bar{\rho}_d$, was correlated as a function of the operating variables as:

$$\bar{\rho}_d = \alpha - \beta \ (V - V_{mf})$$

where $\alpha$ and $\beta$ are the constants depending on the particle diameter only, $V$ and $V_{mf}$ are fluidizing gas velocity and minimum fluidizing velocity of the particles.

The density, $\rho$, in the falling zone was found to be approximated by the following equation, which is characterized by the two indices A and B:

$$\text{Log} \ (\rho \ / \ \rho_{pa}) = A + B \ (h/L_{mf} - 1)^2$$

The effects of operational variables, such as air velocity, $V$, static bed height, $L_{mf}$, particle size, $D_p$, on these indices were investigated. They were expressed as functions of dimensionless groups as:

$$|A| = 1.349 \times 10^{-5} (\frac{D_p V \rho_F}{\mu})^{0.978} (D_p/D_c)^{-1.265} (L_{mf}/D_c)^{0.3469}$$

$$|B| = 5.492 \times 10^{9} (\frac{D_p V \rho_F}{\mu})^{-2.094} (D_p/D_c)^{3.045} (L_{mf}/D_c)^{0.3474}$$

The effects of particle composition in beds containing a mixture of two sizes of particles (40-45 mesh and 80-100 mesh glass beads) on fluidization characteristics were also studied. The results showed that the values of

indices A and B were significantly changed only when the mixture contained less than 10 weight percent of one component.

Three different ways to define the height of a fluidized bed were considered:

(a) End point of the density profile.

(b) Cross point of the normalized density profile with that of an ideal fluidized bed.

(c) Maximum point of axial instability index distribution curve.

The height defined in (a) corresponded to the maximum bed height as visually observed, while the other two are the average of the fluctuating bed height.

Pressure gradient was correlated in the form of a friction factor. The heights defined in (b) and (c) gave better correlation than that defined in (a). The friction factor obtained is given as follows:

$$f_K = (\frac{D_p}{\rho_F V^2} \cdot \frac{g_c \Delta P}{L} \cdot \frac{\epsilon^3}{1-\epsilon} =$$

$$(8.80 \times 10^7)(\frac{D_p V \rho_F}{\mu} \cdot \frac{1}{1-\epsilon})^{-1.591} (\frac{D_p}{D_c})^{2.126} (\frac{L_{mf}}{D_c})^{-0.298}$$

The heterogeneous distribution of fluidized bulk density in the aggregative fluidized beds has direct influences on the transport and rate processes. Therefore, the knowledge of the density distribution in the aggregative fluidized beds cannot be over-emphasized. The works of previous investigators on the transport and rate processes in fluidized beds were re-examined in the light of the results obtained in this investigation.